Computer-Aided Pre-operative Planning System for Skull Base Surgery

Nava Aghdasi

A dissertation
submitted in partial fulfillment of the
requirements for the degree of

Doctor of Philosophy

University of Washington

2017

Reading Committee:

Dr. Blake Hannaford, Chair

Dr. Linda Shapiro

Dr. Howard Chizeck

Program Authorized to Offer Degree:
Electrical Engineering

University of Washington

Abstract

Computer-Aided Pre-operative Planning System for Skull Base Surgery

Nava Aghdasi

Chair of the Supervisory Committee:
Dr. Blake Hannaford
Electrical Engineering

Despite major technology advancements in image analysis, simulation and endoscopic procedures, surgeons do not have access to simple, yet practical and efficient planning tools for complex operations in skull base surgery. Currently, in advanced medical centers that perform these operations, all decisions about the surgical approach and treatment are made at tumor board meetings by reviewing 2D image slices in standard axial, coronal, and sagittal planes.

For experienced skull base surgeons, finding the connection and correlation of pre-operative scans to intra-operative 3D anatomy is easy due to years of practice. Others must examine each slice of the pre-operative Computed Tomography (CT) scan, to answer whether the trajectory is crossing or how close the trajectory is to the critical anatomies. This make the process time-consuming and gives results which may not be optimal. In addition, surgeons often rely on their training, background, and experiences to select their approaches. So there is no quantitative information to support the decision process.

This dissertation presents a method for assisting the surgeons in pre-operative planning by automatically providing the surgeons one or more optimal approaches by optimizing the cost function that is based on surgeon's decision-making objectives. It is anticipated that using this approach, will transform a process that is subjective to a method that is coherent and quantifiable.

TABLE OF CONTENTS

LIST OF FIGURES

GLOSSARY

ORBIT: The skeletal cavity which provides a stable and enclosed environment for orbital structures in order to protect them.

ORBITAL STRUCTURES: Each orbit contains main structures such as the eyeball, the optic nerve and the extraocular muscles. Also contains additional structures such as the lacrimal apparatus, adipose tissue, fascia, and the vessels and nerves supplying these structures.

ATLAS: refers to a specific model which consists of two parts: an intensity image (template) and its segmented image (the atlas labels). New data is mapped to the atlas via registration algorithms and therefore the atlas information cane be transformed to the new data.

SKULL BASE: refers to the bottom of the skull, or the plate of bone upon which the brain sits. The skull base is an important area since it separates the brain from the remainder of the anatomic structures in the head, including the sinuses, eyes and ears.

SURGICAL APPROACH: refers to ways/ methods of getting to the tumors in the skull base.

SURGICAL PATHWAY: refers to a 3D volume from the surface of skull to the skull base where instruments can travel through to get to the target and remove it.

SKULL BASE SURGERY: The procedure of removing the tumors or defects involving the skull base using open or endoscopic skull base surgery.

ENDOSCOPIC SKULL BASE SURGERY: refers to the type of surgery where the surgeon may make a small opening in order to remove a growth through a thin lighted tube called an endoscope.

SURGICAL NAVIGATION SYSTEM: refers to a system which the surgeon instruments can be tracked by the navigation system. The position of a tracked instrument in relation to the patient's anatomy is shown on images of the patient, as the surgeon moves the instrument.

ACKNOWLEDGMENTS

First, I would like to express my sincere gratitude to my advisor Professor Blake Hannaford. Without your encouragement and continuous support, this journey would have been impossible for me. Your dedication to research, curiosity, and ideas always inspired me to take another step forward. Thank you for listening to my ideas and challenging me to elaborate and explore more.

I wish to express my gratitude to Dr. Kris Moe and Dr. Randall Bly and acknowledge their generous and invaluable guidance and assistance. Thank you for being so patient with me and believing in me. Also, thank you for allowing me to come to the operating room, it helped to shape my thesis and more importantly to reflect and be grateful for my life.

Dr. Angelique Berens, I have learnt a lot from you and you are an example of successful woman to me. Thank you.

Dr. Yangming Li, thank you for your feedback, guidance, and discussions. Your commitment and eagerness for research motivated me everyday.

I also would like thank my Committee members: Professors Blake Hannaford, Howard Chizcek, Linda Shapiro, and Archis Ghate who offered me valuable suggestions and feedback, took the time to come to my exams, and helped me with scheduling despite their busy agenda. Thank you.

I sincerely thank all members of the BioRobotics Laboratory and especially Danying, David, Mohammad, Kevin, Andrew, and Andrew for all their friendship and support. You are all very amazing people.

Finally, I would like to thank Maman, Ammeh, and my dear sister, Neda. You taught me to be strong, patient, and always hopeful. Merci!

DEDICATION

To the memory of my father

Chapter 1

INTRODUCTION

Technological advances in optics, materials and surgical navigation permit endoscopic surgical approaches to reach more locations in the skull base, thus dramatically reducing morbidity compared to open craniotomies that requires a large skin incision and retraction of the brain. While these operations provide more benefits to patients through rapid recovery, shorter hospital stays better cosmesis and improved quality of life after surgery [2], the required skills are highly complex due to density of critical neuromuscular structures and the narrow anatomic confines in this region [3], [4] .

While endoscopic surgery is becoming a more popular surgical method to treat the tumors in skull base, major complications occur in 17% of cases [5] (complications such as blindness, Cerebral Spinal Fluid (CSF) leaks, hemorrhage, stroke and death) [6]. Considering the frequency at which these procedures are performed makes them relatively common occurrences. To prevent complications, pre-operative planning becomes an inevitable step before the performing the procedure. However, surgical planning tools for surgeons to plan their approaches in these procedures are limited or not available. The current practice of planning is similar to the method that was performed a decade ago, where the surgical approach is planned and discussed by reviewing 2D image slices in standard axial, coronal, and sagittal planes. Since patient surgical outcome is directly correlated with the quality of the pre-operative planning, the need for an effective planning system is clear.

In planning, selection of the surgical approach (pathway) is critical, for reducing morbidity related to the surgery and to gain sufficient access to a skull base legion. The pathway is the 3D shape which instruments are inserted and the operative task is performed. The pathway passes through structures that are either removed or temporarily retracted to access the target. Therefore, it is important to select the pathways that are less disruptive to structures, specially critical structures, which removal or excessive retraction would cause complications. Selecting an appropriate pathway to treat the target is not an intuitive task. Experienced skull base surgeons, through years of experience can make the connection between the 2D images, 3D pathways and anatomical structures pre- and intra-operatively. Therefore, reviewing 2D images, planning the 3D pathway while considering the relationship of the pathway with other structures has became straightforward for them to some extend. This process is challenging, time-consuming and error-prone for new surgeons. On the other hand, surgeons often select the surgical pathway based on their training background and experiences, which make the reasoning behind the selection hard to explain or justify. Further, there is no quantitative information to support the decision process.

Surgical pathway selection can be defined as a function of individual patient anatomy, tumor location, pathology, surgical instrumentation, and visualization technology, and therefore, can be systematically computed with the proper input parameters.

This dissertation focuses on methods for pre-operative surgical planning for skull base surgery. The goal is to understand the decision-making and thought process of surgeons when selecting one surgical pathway over the other. The rules and objectives can be formulated as a cost function which then can be optimized to obtain the optimal approaches. This method of surgical approach selection results in major contribution to trainee education, the development of new surgical approaches, and the ability to accurately study clinical outcomes with fewer variables.

The main contributions of this dissertation include:

- Developing a pre-operative manual skull base surgical pathway planning using mobile portals

- Identifying the surgeons decision-making objectives in pathway planning and translate the objectives into a cost function

  - Developing an semi-automatic pre-operative planning with surgeons' inputs as weights and providing the optimal approach based on surgeons preferences
  - Developing an automatic pre-operative planning method by providing surgeons a set of optimal approaches, the final pathway is selected by the surgeon among the set of optimal pathways based on their preferences

- Developing an anatomical semantic atlas with clinically significant information for every voxel within CT

The rest of this document is organized as follows. Chapter 2 proposes a novel method for segmenting orbital structures inside the skull base. Chapter 3 describes the methods of the pre-operative surgical pathway planning. These methods are verified with real patient data and the optimal pathways were compared with post-operative pathways in Chapter 4. The construction of the skull base atlas and an example of usage are described in Chapter 5. Shortcomings of the proposed methods and directions for future work are described in Chapter 6.

Chapter 2

EFFICIENT CRITICAL STRUCTURE SEGMENTATION UTILIZING ANATOMICAL KNOWLEDGE

The base of the skull contains numerous critical structures because of its location between the brain and the rest of the body. Vital blood vessels and nerves pass through the holes in the skull base, disturbing any of them can have severe consequences such as blindness, deafness, paralysis, or death [7]. The goal of minimally-invasive skull base surgeries are to maximize the efficacy while preserving neurological function to the greatest extent possible. In many skull base procedures, due to the location of the common lesions and increasing interest in endoscopic orbital and Trans-orbital approaches because of its success [8], the surgical pathway may come in close distance to the orbital structures. Therefore, structures such as the optic nerves, eye globes, and extra-ocular muscles have important role in pre-operative planning or intra-operative navigation. In many cases, damage to these structures is irreversible and can cause harm from cosmetic issues, impaired vision, or blindness. To improve the patients safety and quality of lives after the procedure, it is necessary to handle these structures with extra case in pre-operative planning and during the surgery [9].

Medical image segmentation has been studied for decades because of its importance, yet there is not a general method for segmentation. A particular method may work well only on one part of the body. Some recent commercial software allows for semi or fully automated segmentation of some structures, but their application is limited. Manual delineation using drawing tools by a trained expert is the most commonly used segmentation technique in clinics, which is time-consuming and suffers from inter and intra-rater variability [10].

We present a fully automatic method for segmenting orbital structures (globes, optic nerves and extra-ocular muscles) in CT images. The clinical requirements that motivated this work were: 1. the segmentation of the structure must be on CT images which has low contract for soft tissues; 2. the method must be accurate and efficient with minimum or no user interaction; 3. the method must not require extra computational hardware for processing; and 4. training data is limited.

In our proposed method, prior anatomical knowledge such as shape, intensity and spatial relationships of organs and landmarks were utilized to define a Volume Of Interest (VOI) which contains the desired structures. Then new VOI was used for fast localization and successful segmentation of each structure using predefined rules. Testing our method with 30 publicly available datasets, the average dice coefficient for right and left sides of [0.81, 0.79] eye globes, [0.72, 0.79] optic nerves, and [0.73, 0.76] extra ocular muscles were achieved. The proposed method is accurate, efficient, does not require training data and its intuitive pipeline allows the user to modify or extend it to other structures.

2.1 Introduction

Recent advances in medical imaging have had a positive impact in many medical areas. In skull base surgery, the role of medical imaging is unavoidable due to the numerous vital structures in this region. Critical structures such as the optic nerve, eye globe and extra-ocular muscles must be considered in the planning stage and during the surgery. Damage to these structures can cause significant patient harm from disfigurement, diplopia (or double vision) to blindness. Therefore, localization of these structures is essential pre and intra operatively. Pre-operatively it is important to incorporate this information into the surgical plan in order to minimize the disturbance to vital structures. This is critical when the surgical approach is in close proximity to these vital structures due to lesion location. Intra-operatively identification of these structures will assist the surgeon to avoid the damage from surgical instruments, especially powered instruments such as the Microdebrider. However, in current skull base surgeries, these structures are not segmented and surgeons use their anatomical knowledge and experiences to locate them on pre operative images or on the patient intra-operatively. This is because the available segmentation tools are limited and manual delineation of these small structures requires expert time. Although there has been many successful skull base surgeries without segmentation, damage to orbital structures is one of the common complications of these surgeries. Therefore, automated segmentation methods are preferable to better aid physicians and more importantly to improve the patients treatments and safety.

In skull base surgery and procedures such as orbital reconstruction, the CT images are the main image modality used (in planning stage and intra-operatively) due to the high intensity of the bone. In the navigated surgery, the bony structures can be used as landmarks to register and calibrate the accuracy of instruments tracking. Therefore, we are interested in the segmentation of the structures inside the orbital bone in CT. Fast delineation of these structures is beneficial in the planning stage to plan and examine different approaches and intra-operatively to avoid the chance of damage.

In CT, structures can be classified into two categories:

- Structures with distinct edges or region characteristics different from surrounding structures: Examples include bony structures

- Structures with no clear distinct characteristics: Examples include soft tissue structures

Segmentation of the soft tissue structures in CT is challenging, specially for structures with small sizes such as optic nerves, Fig 2.1. Therefore, incorporating prior knowledge becomes essential. On the other hand, structures with distinct characteristics are relatively easy to segment and in cases where the image contain noise or artifacts, additional shape or intensity information can be used to accomplish the segmentation task. Therefore, structures with distinct characteristics can be used as stable features and prior knowledge to segment soft tissue. For instance the spatial relationship of a desired structures (with no distinct characteristics) to bony landmarks can be used as prior knowledge in segmentation process of that structure. Predefined rules that takes into account prior information about the locations of the organs and their appearance in CT images can be used for segmentation.

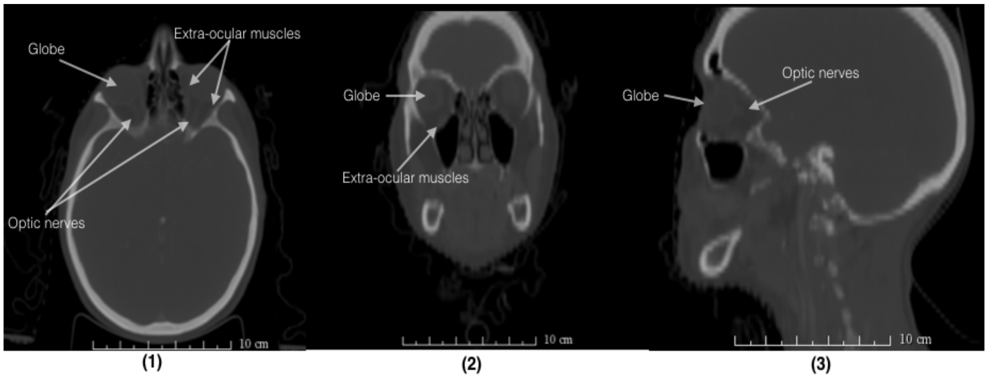

Figure 2.1: Segmentation of desired structures (optic nerve, eye globe and extra ocular muscles) is challenging due to small size and low-tissue contrast in CT images

This rule-based approach uses anatomical context and prior knowledge such as structures' location and its extension for enhancing, improving, and automating the segmentation process. Furthermore, anatomical similarity allows to exploit these rules by detecting predefined landmarks to segment the structures even where there is patient variability.

The segmentation is achieved by combining multiple anatomical knowledge (geometric shape, relationship to other structures and intensity information) with image processing techniques. The proposed method progressively locates anatomical landmarks to restrict the original volume to a smaller volume, which has a higher probability of containing the desired structure. Then segmentation is performed in the smaller volume, which makes the process more efficient and accurate. The process takes less than 5 minutes and does not require training data sets. The simple segmentation pipeline and utilizing anatomical features that are intuitive for the users (surgeons), allows them to modify and guide the result of each step in case of failure or abnormal anatomy.

2.2 Background and Literature Review

Over the years, medical image processing has contributed a lot in medical applications. For example, image segmentation, image registration and image-guided surgery. Image segmentation is an essential part of the medical image processing for extracting the region of interest (ROI) through automatic or semi-automatic processes. Several common approaches have appeared in the recent literature on medical image segmentation that can be divided into following categories: 1) Thresholding approaches; 2) Region growing approaches; 3) Classifiers; 4) Clustering approaches; 5) Markov random field models; 6) Artificial neural networks; 7) Deformable models; 8) Atlas-guided approaches; and 9) Knowledge-based approaches [11]. Each method is described briefly with their advantages and disadvantages.

Thresholding is one the simplest and fastest segmentation methods based on the assumption that images are formed from regions with different gray levels. Thresholding requires that the histogram of an image has a number of peaks, each corresponds to a region and it does not work well for an image without an obvious peaks or with broad and flat valleys. Method such as Ostu's thresholding can be used to select the global threshold value by minimizing the intra-class variance. Thresholding does not consider the spatial details and therefore the segmented region may not be continuous [12].

Region growing is an interactive segmentation method which requires some seed points to be initialized and the region will be grown based on a predefined law such as homogeneity properties of the neighboring pixels. Region growing has inherent dependence on the selection of the seed region and the result may be different based on the seed [12].

Classifier methods are pattern recognition techniques that seek to partition a feature space derived from the image by using data with known labels. A feature space is the range space of any function of the image, with the most common feature space being the image intensities themselves. Classifiers are known as supervised methods because they require training data. A number of classifier methods have been used for image processing, such as k-nearest neighbor and maximum likelihood [11].

Clustering methods essentially perform the same function as classifier methods without the use of training data (unsupervised learning). To compensate for the lack of training data, these methods iteratively alternate between segmenting the image and characterizing the properties of each class. Three popular clustering algorithms are K-means, fuzzy c-means and expectation- maximization [12].

Markov-random field are statistical model that can be used within segmentation methods which model the spatial relationship between nearby pixels. In medical imaging, they are typically used because most pixels belong to the same class as their neighboring pixels. The difficulty with these models is proper selection of the parameters controlling the strength of spatial interactions [12].

Artificial neural networks methods are parallel networks of processing elements or nodes that simulate biological learning. Learning is achieved through the adaptation of weights assigned to the connections between nodes. Neural networks in medical imaging are commonly used as a classifier, in which the weights are determined by using training data [12].

Deformable models methods are model-based techniques for delineating region boundaries by using closed parametric curves or surfaces. The model must be placed near the desired boundary and then allowed to undergo an iterative relaxation process. One of the common method used is active contour [13].

Atlas guided method is a powerful tool when a standard atlas or template is available. The atlas is used as a reference frame for segmenting new images. It finds a one-to-one transformation that maps a pre-segmented atlas image to the target image that requires segmenting. The transformation can be linear, but because of the anatomical variability, a sequential application of linear and non linear transformation is often used [12].

Knowledge-based method has long history which utilizes knowledge of anatomy to extract the organs. Knowledges such as size, locations and spatial relations of organs of the human body are important to localize and segment different structures. Usually domain knowledges are combined with knowledge of the image processing, and the effects of various image processing operators to extract the organs [14].

The image segmentation field has been studied for decades and the above approaches are not all image segmentation algorithms used. Often multiple techniques are used in conjunction. Also, there is not a general method for segmenting all organs and an algorithm may give the best result only when it is used for an organ with specific image modality.

Different methods exist for the segmentation of eye globes and optic nerves. The method of Dobler et al. [15] built a precise metric model of the eye for proton therapy, using ellipsoid and cylindrical shapes for different parts of the ocular system. The geometric model is adapted to the particular image volume using atlas-based image registration. Parameters for most objects are set via ultrasound measurements, and the rest is set to predetermined fixed values. In their model, the eye globe is an ellipsoid with variable length half axes and the optic nerves are not considered.

Bekes et al.[16] proposed a geometric model-based method for segmentation of the eye globes, lenses, optic nerves and optic chiasm in CT images. Sphere, cone and cylinder shapes were used to model the above structures respectively. To perform the segmentation, user was required to provide seeds to define the center of eye globes and nerves.

The method of D'Haese et al.[17] segments the organs of sight and some brain structures by applying predefined anatomical models that were deformed to segment the structures in target volume. The method was performed on MR images, where the contrast is better and separation of different tissue types is easier, compared to CT images.

Isambert et al.[18] used single atlas registration method on MRI to segment the brain organs (including optic nerves and globes) at risk in radiation therapy. Although, excellent agreement was achieved for larger organs, for optic nerves the Dice Similarity coefficient (DSC) of 0.4 to 0.5 was reported.

Gensheimer et al.[19] showed utilizing multi-atlases where each atlas is registered to the target image separately, improved the accuracy of the segmentation of smaller structures such as optic nerves.

Panda et al.[20] used multi-atlas registration method, the registration process had two steps: 1) bony structure affine registration and cropping the optic nerve regions in both target and atlases. 2) non-rigid registration of the cropped volumes. The DSC and Hausdorff Distance (HD) of [0.7, 3.7] (optic nerves) and [0.8, 5.2] (for both globes and muscles) were reported.

Noble et al.[21] proposed a segmentation method which combined the image registration techniques with structure's shape information. The optic nerves and chiasm were modeled as a union of two tubular structure. Statistical model and image registration were used to incorporate a priori local intensity to complete the segmentation. The mean DSC of 0.8 was achieved when compared to manual segmentations over ten test cases.

Chen et al.[22] used a multi-atlas registration method to segment the structures of head and neck. The proposed method had a global level (affine and non-rigid) registration which allowed for initial alignments of the target volume with atlases, followed by local level registration by defining a bounding box for each desired structure. For optic nerves the average (left and right) DSC and HD of [0.6, 2.8] was reported with processing time of about 90 minutes.

Albrecht et al.[23] used multi-atlas registration followed by an Active Shape Model (ASM) fitting (for small structures) to refine the segmentation for individual organs. Rigid registration was done by detecting a set of obvious landmarks and then a non-rigid (DEEDS algorithm) for computing the deformable transformation. This transformation was used for initial alignment, then the aim was to place the boundary points of the shape model at image points that have similar profiles. With this method, the average DSC and HD (left and right) of [0.6, 3.6] were reported and registration of target volume to each atlas took about 1 to 5 minutes.

With registration, model based, and neural networks approaches, labeled training data is required to create an atlas (or multiple atlases for improved results) or models, labeling the data is time consuming and demands expert time. In addition, accurate results depend on optimizing the large number of parameters which can be computationally expensive.

2.3 Efficient Orbital Structures Segmentation With Prior Anatomical Knowledge

The proposed technique is divided into two main parts: 1) given a patient data, find the smallest volume (which contains all desired structures) by detecting a set of anatomical landmarks 2) on this volume, segment different structures according to predefined rules.

Based on the anatomy, the desired structures (optic nerve, globe and extra-ocular muscles) are located and protected by the orbital bone. Therefore, the smallest volume containing these structures would be orbital volume (volume inside the eye socket). Furthermore, within this volume the structures are segmented in the following order: globes, optic nerve and extra-ocular muscles.

In next two sections, we describe the steps to accomplish each part of the segmentation pipeline, as shown in Fig 2.3.

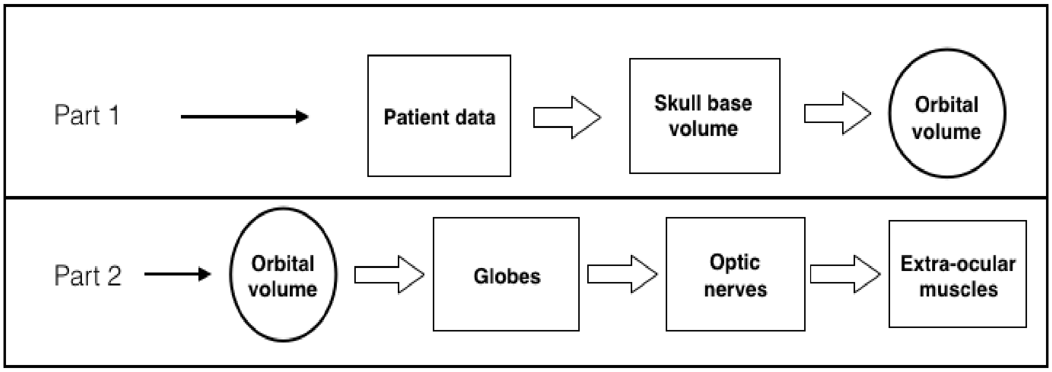

Figure 2.2: Two main parts of the segmentation method

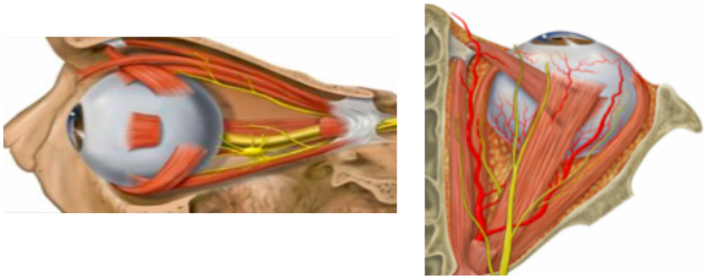

Figure 2.3: Orbital volume with target structures (Illustration by Patrick J. Lynch distributed under a CC-BY 2.5 license.)

2.3.1 Part 1: Orbital Volume Detection

The goal of this part was to get the smallest volume (orbital volume) which contained all the desired structures. To achieve this goal a set of landmarks were defined and the original data was updated to a smaller volume progressively. The following table summarize the landmarks and the resulting updated volumes.

Table 2.1: Segmentation steps for part 1

Steps	Detected landmarks	Analysis on	Input Volume	Output (updated) volume
1	Nasal tip	3D soft tissue volume	Original patient data (Fig4.1)	Skull base volume(Fig4.2)
2	Nasal tip & frontal bone	3D bone volume	Skull base volume (Fig4.2)	Sub-volume: Orbital floor to orbital roof (Fig4.3)
3	Zygoma bone	2D axial bone	Sub-volume: Orbital floor to orbital roof (Fig4.3)	Divided left and right sub-volumes (Fig5.2)
4	Orbital boundary bone	2D axial bone	Divided left and right sub-volumes (Fig5.2)	Left and right orbital volumes(Fig6.3)

Simple thresholding using Hounsfield Unit (HU) for bone and tissue produced reasonable results necessary to detect the initial landmarks. However, threshold values were verified for each data set by analyzing the intensity profile of the horizontal midline in all axial slices, Fig 2.4 (1).

Intensity profile is the set of intensity values of regularly spaced points along a line segment, Fig 2.4 (2).

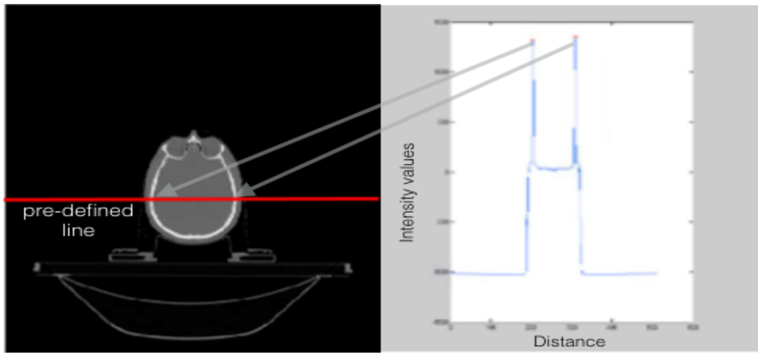

(1) (2)

Figure 2.4: Threshold values were obtained by finding the local maximum (2) in intensity curve along the predefined mid-horizontal line in all 2D axial slices (1)

The maximum value of the intensity curve for each slice represents the bone threshold value due to high density of the bone in CT images. In addition, the location of the maximum values on the intensity curve and their euclidean distance represent the width of the skull in many slices, Fig 2.4. If the calculated distance was not in the range of average skull width ($152 \sim 178$ mm), intensity value of that slice was ignored. For instance near mandible the maximum values may be higher due to dental filling, in those slices the distance check would be necessary to select the correct threshold. The accepted maximum intensity values of all slices was averaged and used as threshold. Verifying the HU number of the bone with the threshold value obtained by mid-line intensity curve would ensure that the threshold value is robust to different scanners [24]. Next, the four steps of table 1 are described in details:

- **Step 1: (Input volume: original patient data - Output volume: skull base volume)**

  The initial landmark (nasal tip) was detected by finding the intersection of a XZ sliding plane and the point cloud representation of the soft tissue thresholded volume, Fig 2.5 (1). The skull base volume was obtained by updating the original volume using this nasal tip position.

- **Step 2: (Input volume: skull base volume - Output volume: sub-volume: Orbital floor to orbital roof)**

  Similar approach as step 1 was used to detect the nasal tip and frontal bone landmarks, except that the bone thresholded volume was used Fig 2.5 (2). The volume between these two landmarks (output volume) was used for further processing, Fig 2.5 (3).

- **Step 3: (Input volume: sub-volume: orbital floor to orbital roof - output volume: divided left and right sub-volumes)**

  The goal of this step was to restrict volume 1 even more and divide it into the left and right side. The Zygoma bone was detected by using the bone thresholded volume 1 and determining the closest bone pixels to the top corners of the image on each 2D axial slice, Fig 2.6 (1). Therefore, the landmarks (Zygoma, nasal tip and the center of

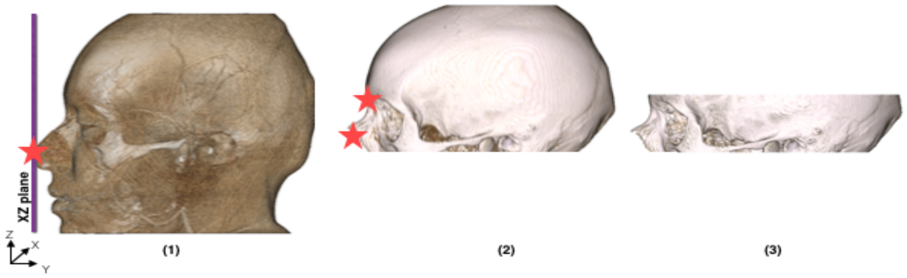

Figure 2.5: Step 1 and 2: Initial volume of interest (3) was obtained by restricting the original volume using anatomical landmarks such as nasal position and frontal bone represented by stars in tissue (1) and bone (2) thresholded volumes

mass) were used to form a pyramid volume to update the input volume and divide it into the left and right sides, Fig 2.6 (2).

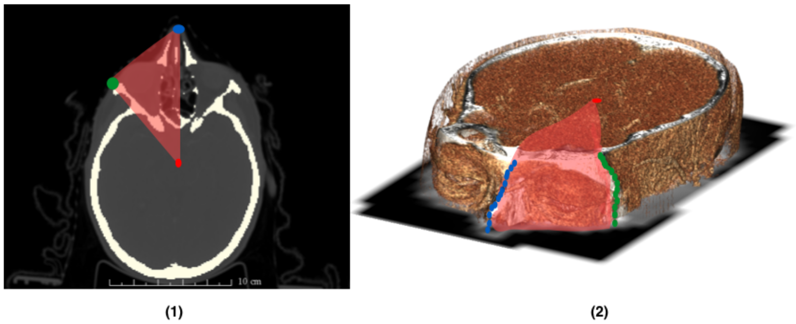

Figure 2.6: Step 3: Zygoma landmarks were detected on each 2D axial slices (1). Zygoma, nasal tip and center of mass were used to form a pyramid volume (red) and restrict the volume 1 to smaller volume (left and right) (2).

- **Step 4: (Input volume: divided left and right sub-volumes - output volume: orbital volume)**

  In order to get the orbital volume, the bone boundaries of the region inside the eye socket were detected in 2D axial slices of the volume 1 (left and right) separately. on each slice, the boundaries were obtained by finding the first intersection point of the bone mask to the vertical lines parallel to image y-axis and equal distances based on image resolution, Fig 2.7 (2). A cubic spline was fitted to the points for a smooth boundary on each 2D slices, Fig 2.7 (3). Using these points a binary mask was defined on each slice and the final orbital volume which contained all target structures (eye globe, optic nerve and extra ocular muscles) was constructed from pixels in each slice that overlapped with the binary mask.

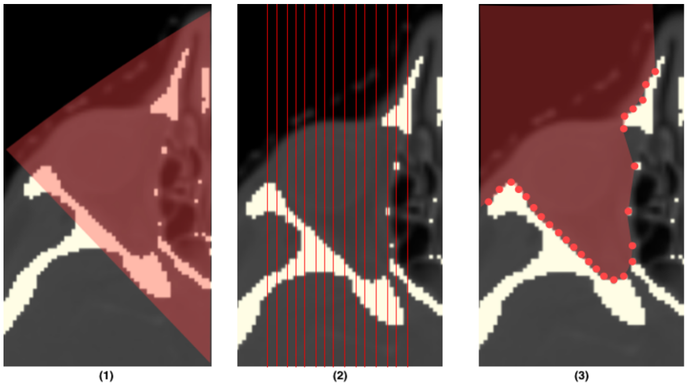

Figure 2.7: The volume (Fig. 2.6 (2)) was restricted more by finding the intersection of the first bone pixels with equally distance vertical lines (2) and fitting line to obtained points and creating a binary mask, represented by red convex plane (3). Therefore, final orbital volume was constructed from pixels in each slice overlapped with binary mask.

2.3.2 Part 2: Extraction of orbital structures

The goal of part 2 was to extract each structure by using the rules that incorporated the knowledge about intensity, neighborhood relations and geometric shapes. The structures were segmented in a following order: globes, optic nerve and extra-ocular muscles. After detecting each structure the orbital volume (obtained from part 1) was updated and was used to segment the next structure. The segmentation details of each structure are described now:

- **Eye globe segmentation:** The globe segmentation was achieved in two steps: First, finding the approximate boundaries of the globe in 2D axial slices. Second, 3D shape (sphere) fitting to the voxels (inside the approximated boundaries) for better refinement of the boundaries.

To approximate the globe boundaries: 2D axial slices of the orbital volume were processed by analyzing the intensity distribution of the pixels along the horizontal and vertical lines parallel to image axis, Fig 2.8 (1 and 2). Furthermore, the globe's appearance in CT images, having brighter boundary area than the surroundings, the derivative of each line intensity was used to find the pixel positions [x, y] of the first and second peak points. For instance, consider a horizontal intensity line the first two peak points represented the top and bottom of the globe boundary. On each slice, multiple points were obtained (2 point for each line) these points were clustered with k-means clustering (4 clusters: top, bottom, left and right sides of globe), Fig 2.8 (3). While any edge detection technique (Example: Canny edge detection) can be used to find the boundaries, additional processing was required to identify and separate the globe boundaries from other detected boundaries. Analyzing the intensity along the lines had the benefit of containing the extra position information. Finally, on each 2D axial slice, all pixels inside the detected boundaries were labeled as the approximation of the globe. *To improve the segmentation:* Additional refinement was done by 3D shape fitting. The approximated globe segmentation was converted into the point cloud representation. This step was necessary to remove regions that were not part of the globes as shown in, Fig 2.9 (3). Due to the anatomical shape of the globe, a sphere was used to improve the segmentation, Fig 2.9 (1 and 2) . The parameters of a

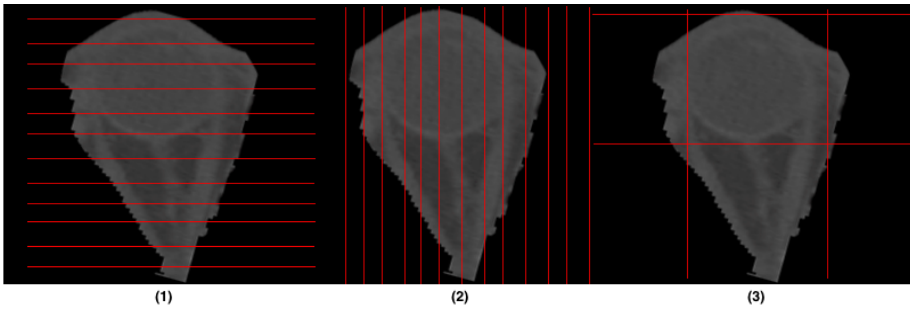

Figure 2.8: Approximation of eye globe boundaries for an axial slice

sphere were found by minimizing the least square distance between the points on the surface of the sphere and globes' voxels. Finally, the intersection of the axial plane to the sphere was labeled as final globe segmentation.

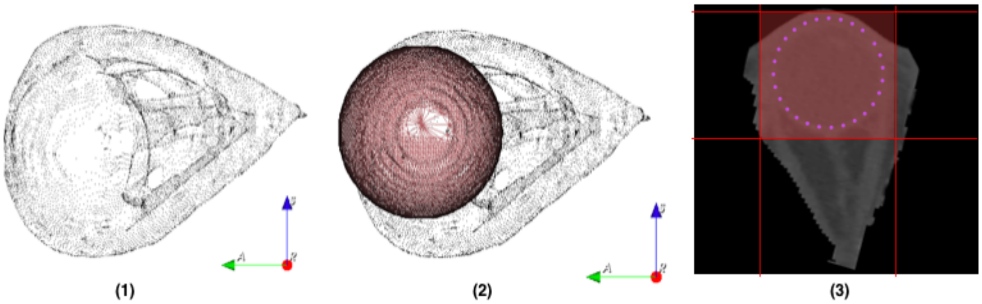
(1) (2) (3)

Figure 2.9: 3D sphere was fitted to eye globe voxels, top view (1) and 3D view (2). 2D visualization of eye globe pixels inside approximation boundary and slice of fitted sphere (3)

- **Optic nerve:** *To segment the optic nerve:*Information such as the spatial relationship to other structures, intensity and shape was exploited. In addition, the orbital volume was updated by removing the globe segmentation, the new volume contained the optic nerve and extra-ocular muscles. Hence, the goal was to detect these structure from the surrounding tissue (background) and then isolating the optic nerve from the extra-ocular muscles.

  Since optic nerve and extra-ocular muscles had similar intensity distributions in the updated orbital volume, Otsu's method was used to find the intensity threshold for separating the foreground (main structures) from the background (surrounding tissue). Foreground points (optic nerve and extra-ocular muscles) were converted to 3D point cloud for isolating the optic nerve, Fig 2.10. *To isolate the optic nerve:* The shape model and relationship with the surrounding muscles were used to define a constrained cost function.

  The geometric model was defined as series of connected cylinders with decreasing radii to emphasize the optic nerve shape, Fig 2.11. The shape was parameterized by two 3D points (front and back of optic nerve) and with fixed exponential decay function (

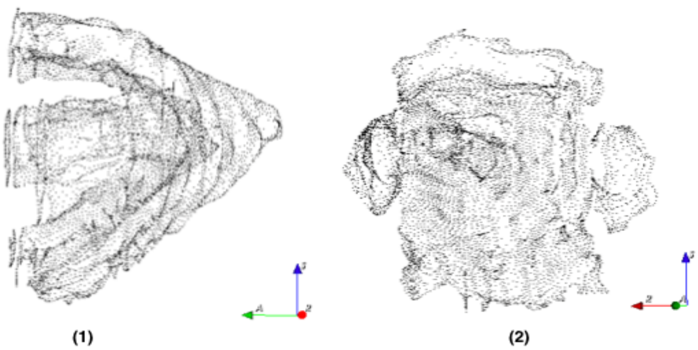
(1)
(2)

Figure 2.10: Point cloud representation of foreground structures (optic nerve and extra ocular muscles) in orbital volume - 3D view (1) and top view (2)

$2e^{-2d}$) as radius.

The cost function was defined as the number of foreground points inside the shape model. Having a fixed radius for the model and boundary constraints, the decision variables (the parameters of the model) would contain the foreground points of optic nerve by maximizing the cost function. Nelder-Mead optimizer was used which is a

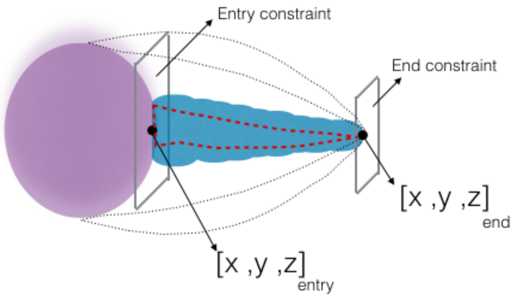

Figure 2.11: Optic nerve model, decision variables and constraint for optimization

simplex method for multidimensional optimization without derivatives. The algorithm maintains a simplex which are approximations of an optimal point. The vertices are sorted according to the cost function values. Then algorithm attempts to replace the worst vertex with a new point, which depends on the worst point and the center of the best vertices [25]. Fig 2.12 (2) shows the final cylinder which maximized the cost function and foreground points inside the cylinder which were labeled as optic nerve voxels, Fig 2.12.

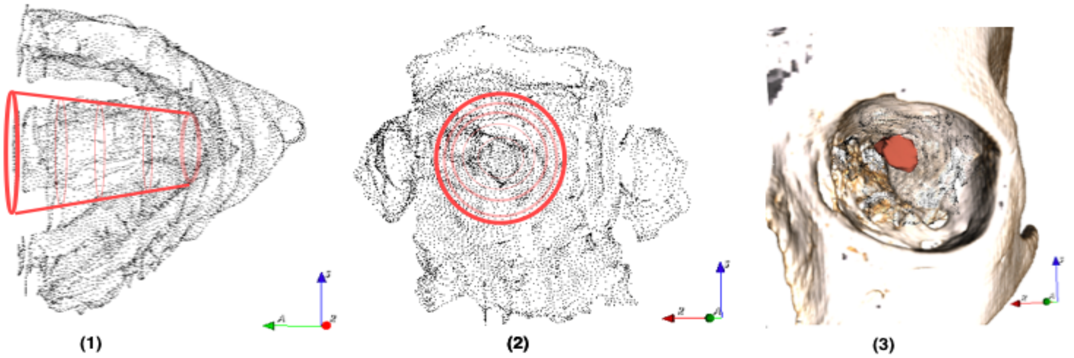

Figure 2.12: Final cylinder orientation which maximize the number of foreground voxels (1, 2) and optic nerve segmentation (3)

- **Extra-ocular muscles:** *To extract the extra-ocular muscles:* The optic nerve points obtained from the previous step was removed from the 3D point cloud foreground points, Fig 2.12. For further segmentation of the muscles into Superior, Inferior, Lateral and Medial rectus muscles, the relative location (above, bellow, right and left) of remaining voxels (3D points) relative to segmented optic nerve was considered. To improve the segmentation results, 2D masks were created by projecting the optic nerve voxels onto the axial and sagittal planes, Fig 2.13. Therefore, voxels that were above or bellow the optic nerve and their projection overlapped with the 2D axial mask were labeled as Superior and Inferior rectus muscles respectively. Similarly, voxels that were left or right of the optic nerve and their projection overlapped with the 2D saggital mask were labeled as Lateral and Medial rectus muscles, Fig 2.14.

2.4 Experimental Results

2.4.1 Imaging Data

The imaging data used to test the described method was a subset (30 datasets) of a publicly available data set via the Cancer Imaging Archive [26]. CT images and manual segmentation of structures were in compressed NRRD format. For all datasets, the reconstructed matrix

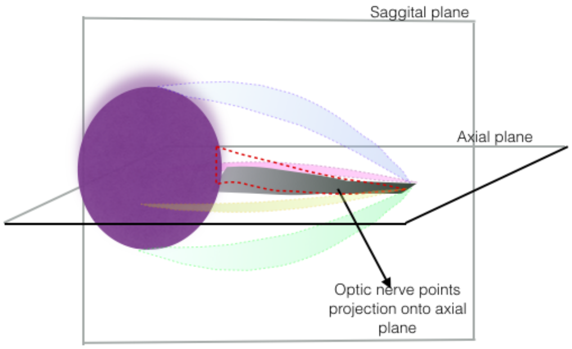

Figure 2.13: Extra-ocular muscles

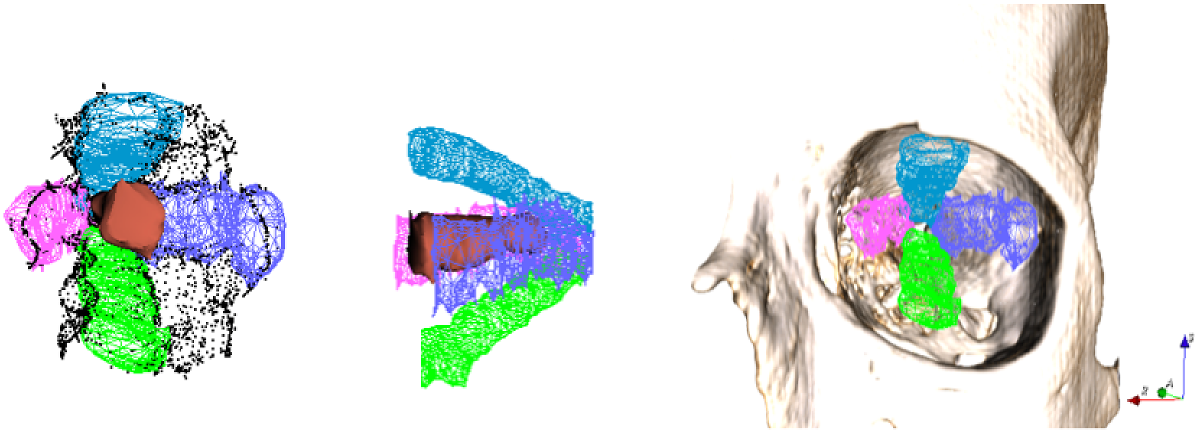

Figure 2.14: 3D point cloud representation of extra ocular muscles 3D view (1, 2) and extra ocular muscles segmentation (3)

was 512×512 pixels. In-plane pixel spacing was isotropic, and varied between 0.98×0.98 mm and 1.17×1.17 mm. The number of slices was in the range of 110 - 190 slices. The spacing in z-direction was between 2 mm and 3 mm. Manual segmentation of globes and extra-ocular muscles was done by an Otolaryngologist in our team. The segmentation of optic nerve was available with the data, however only the part of the optic nerve inside the orbital volume was considered.

2.4.2 Evaluation Metrics

Dice Similarity Coefficient (DSC)

The DSC measures the volumetric overlap between the automatic and manual segmentation[27]. It is defined as:

$$Dice = \frac{2|A \cap B|}{|A|+|B|} \tag{2.1}$$

A and B are the labeled regions that are compared. Volumes are represented by the number of voxels. The Dice coefficient can have values between 0 (no overlap) and 1 (perfect overlap).

Distance Measure

Hausdorff Distance (HD) measures the maximum distance of a point in a set A to the nearest point in a second set B. The distance measure we used was 95% HD, the calculation of the 95th percentile of the Hausdorff distances. The reason for using this metric is to measure the effect of a very small subset of inaccurate segmentation on the evaluation of the overall segmentation quality [28]. The maximum and average HD was defined as:

$$\begin{aligned} HD_1(A,B) &= max(h(A,B),h(B,A)) \\ HD_2(A,B) &= average(h(A,B),h(B,A)) \end{aligned} \tag{2.2}$$

where:

$$h(A,B) = P_{95_{a \in A}}\{min_{b \in B}||a-b||\} \tag{2.3}$$

2.4.3 Numeric Results

The metrics were computed separately for left and right sides for all segmented structures. Table 1 and 2, summarizes the basic statistics for each metric. The full result are in Appendix A.

Table 2.2: Dice coefficient statistics (right)

Statistics	Right		
	Optic nerve	Globe	Extra-ocular muscle
Average	0.72	0.81	0.75
Std	0.05	0.05	0.08
Max	0.83	0.88	0.90
Min	0.65	0.69	0.62

Table 2.3: Dice coefficient statistics (left)

Statistics	Left		
	Optic nerve	Globe	Extra-ocular muscle
Average	0.79	0.79	0.76
Std	0.06	0.06	0.06
Max	0.92	0.92	0.84
Min	0.62	0.62	0.60

Table 2.4: 95 % Hausdorff distance statistics in mm

Right						
Statistics	Optic Nerve		Globe		Extra-ocular muscles	
	HD1	HD2	HD1	HD2	HD1	HD2
Average	5.12	3.32	2.89	2.44	2.76	2.13
Std	3.00	1.55	0.73	0.48	0.97	0.47
Max	13.41	8.68	4.20	3.22	4.33	3.34
Min	2.31	1.73	0.48	1.39	0.82	1.29

Table 2.5: 95 % Hausdorff distance statistics in mm

Left						
Statistics	Optic Nerve		Globe		Extra-ocular muscles	
	HD_1	HD_2	HD_1	HD_2	HD_1	HD_2
Average	5.73	4.24	3.02	2.62	3.19	2.44
Std	3.10	1.69	1.04	0.73	0.87	0.61
Max	12.87	8.93	5.00	4.18	4.75	4.1
Min	2.59	1.73	0.88	0.98	0.71	1.74

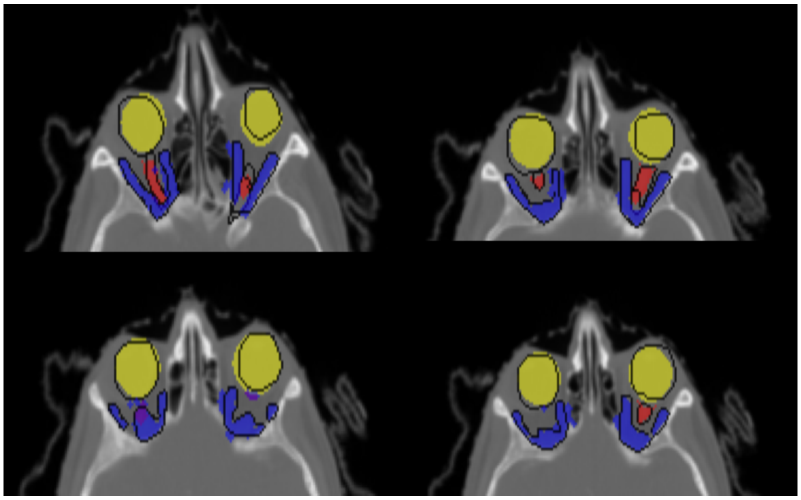

Figure 2.15: Representative slice: orbital structures segmentation with ground truth (black) boundaries

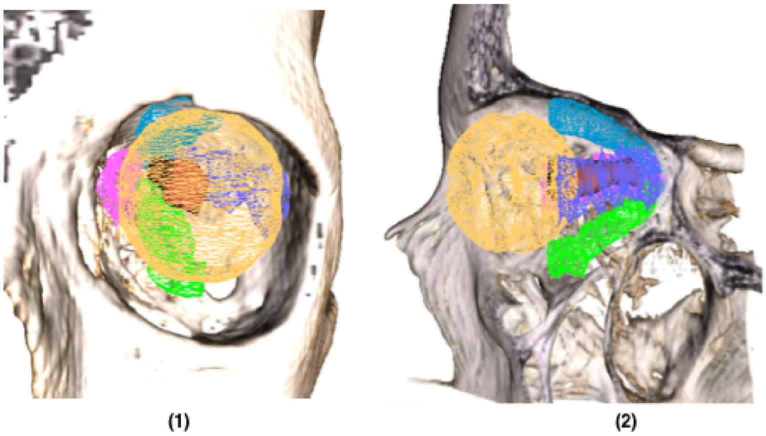

Figure 2.16: Orbital structures segmentation 3D view

2.4.4 Discussion

There is an increasing interest in safety of endoscopic orbital and Trans-orbital skull base surgery due to its less invasive approach. Navigation guidance is highly important in endoscopic surgery for pathway creation, target manipulation, and reconstruction of normal bone anatomy. A major challenge to orbital navigation is segmentation of orbital structures such as the globe, optic nerve, and extra-ocular muscles. To ensure patients' safety, localization of these critical structures would be a key step in pre operative planning and intra operative operation. Chang et al. [29] reported a case of sinus surgery in a patient with distorted anatomy during which the patient's eye was inadvertently removed by a powered surgical instrument. Therefore, the segmentation of the orbital structures and defining them as danger zone where the instruments can not penetrate in or the surgeon will be warned, would protect the patient from possible damages. These cases, motivates the need for efficient segmentation to save time, resources and to prevent complications.

Head and neck segmentation methods are often based on Statistical Models of Shape/Appearance or Atlas Based Segmentation. For both methods, large training data sets are required to create the Atlas or create the models for different structures. Creating training data is time consuming and requires multiple experts time for high quality data. In addition, some of these methods have long processing time and parameters that need to be set for acceptable results. On the other hand, for small structures such as optic nerves, results may not be accurate and therefore additional post-processing must be considered.

Our segmentation approach was to define a set of stable landmarks relevant to desired structures. These landmarks were used to restrict the original volume to the smallest possible volume which contained that structure. Basic geometric shape models were defined and used in an optimization scheme to segment the structure. This rule-based approach was accurate, did not required training data.

Two metrics were used to evaluate the segmentation results. The DSC which measures the overlap between the segmented results and ground truth segmentation and the HD measured the maximum distance of all minimum distances of the segmented voxels to the ground truth voxels. The average DSC of [0.81, 0.72 and 0.73] (right) and [0.79,0.79 and 0.76] (left) for eye globe, optic nerve and extra ocular muscles were achieved with our method. The average HD of [3.32, 2.44 and 2.13 mm] (right) and [4.24, 2.62 and 2.44 mm] (left) were obtained respectively for each structure.

It is generally accepted that DSC value > 0.7 represents excellent agreement [30]. Based on this metric, all structures had a good overlap with manual segmentation. In terms of accuracy, our approach is close to the work presented in [31], where mean DSC of 0.6 was reported with and average HD of 3.1 mm. The obtained results fulfilled the clinical requirements that originally motivated this work, in our case the key points were the quick computation with minimum computational hardware for processing and training data.

The HD measure for globe and extra-ocular muscles were less than 5 mm, however there were cases for optic nerves with large distances (HD >5 mm). The following figure illustrated the comparison of the manual and automatic segmentation for one of these cases. The segmentation results were overlapping, however due to low contrast in lower region the automatic method did not capture the superior section.

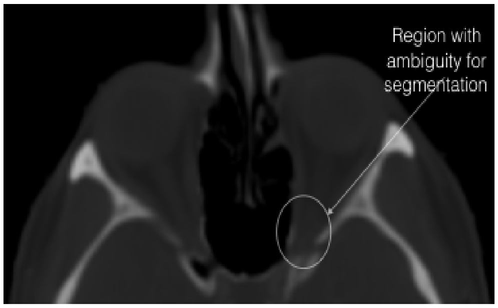

Figure 2.17: Data set 20, (Hausdorff distance > 5mm - contrast changed) in which the true length of optic nerve is not clear

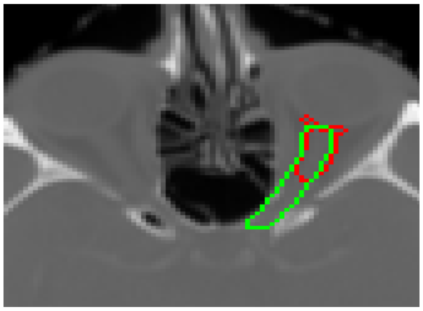

Figure 2.18: Data set 20, comparison of manual (green) and automatic (red) segmentation

The difficulties with optic nerves segmentation were their low contrast with surrounding tissues in CT and also their small size (only present in few slices). Particularly segmenting the optic nerves from extra-ocular muscles at the back of the orbit (just before orbital canal) was difficult. In this area, the optic nerves and extra-ocular muscles are merged. Although constraining the orbital shape with reducing radius improved the optic nerves separation, the same ambiguity was present for segmenting the extra-ocular muscles into different parts, Fig 2.17. Our automated segmentation process is efficient (less than 5 minutes with MATLAB which can be improved) and will save surgeons time from segmenting slice by slice to confirming or editing part of the results, for example editing the optic nerve segmentation represented in, Fig 2.18 (Data set 20 with HD >5 mm) .

One limitation of our method is that if the patient had different orientation during the imaging, severe destructed or abnormal anatomy the segmentation may not detect the landmarks successfully. In these cases the segmentation must be guided by the user such as providing the right transformation for reorienting the image, or selecting few landmarks.

However, for cases where the patient head is deviated from the mid sagittal plane the process can be automated. The angle between the mid sagittal plane and the nasal position obtained from the 3D point cloud representation of the tissue thresholded volume (in step 2 of part 1) can be used to reorient the image, Fig 2.17. Therefore the nasal position would be aligned with the mid sagittal plane. For the cases where the angle of deviation from mid sagittal plane is large, methods such as Iterative Closest Point (ICP) can be used to find the rigid transformation of the target and a reference 3D point cloud in order to reorient the target image. To get the transformation efficiently, using only one reference point cloud would be enough and in addition the bone thresholded point clouds can be used due to its less number of points.

This approach can be used for segmenting other structures, however the rules would be different for a particular structure and must be defined. The future work is to develop a software with an easy interface for surgeons to perform the segmentation by clicking through landmarks, selecting the geometric shapes and defining simple rules. The system record and learn the landmarks, shapes and rules to perform the segmentation for new data set. General

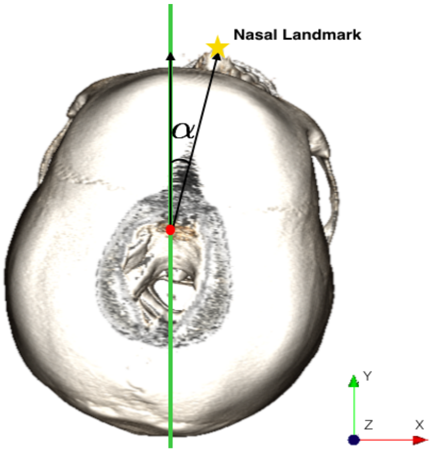

Figure 2.19: Finding the deviation angle necessary to reorienting the image

and easy work flow allows surgeons to “demonstrate” the segmentation to the system, while the system learns the process. The goal is to restrict the original volume to smaller volume by detecting the learned landmarks and performing the rules on the smallest volume.

The described method can automatically segment the orbit and orbital structures including the globe, extra-ocular muscles, and optic nerve using anatomical knowledge. The segmentation process is efficient and does not require training data. Detection of reliable anatomical landmarks to restrict the original volume to smaller volume, reduces the computational cost, sensitivity to image artifacts, and improve the precision.

Chapter 3

SURGICAL PATHWAY PLANNING

3.1 Introduction

The open surgical approach allows for adequate exposure, but subjects the patient to significant morbidity associated with a craniotomy. Craniotomies involve an incision over the scalp and temporary removal of a bone flap. The risks of a craniotomy include infection, bleeding, compression injury to the brain due to retraction, facial nerve injury, and cerebrospinal fluid leak. Minimally invasive endoscopic surgery provides an alternative to open craniotomy for treating many skull base lesions [32]. The use of minimally invasive techniques provides great benefit to the patient through shorter ICU stays, decreased post-operative pain and quicker return to baseline function [33].

Surgical approaches to the skull base have evolved significantly to minimize collateral tissue damage and improve access to complex anatomic regions. Technological advancements in optics, devices such as the ultrasonic bone aspirator, and materials such as injectable hemostatic agents have mirrored and been critical in enabling this progress. Recently, Transorbital portals that allow safe, direct pathways to skull base pathology have been described. These offer opportunities to approach regions that were previously limited in their access endoscopically. Combined with previously described portals including transnasal, trans-oral, trans-maxillary, trans-cervical, and trans-ventricular, there exists a huge number of possible endoscopic approaches [34].

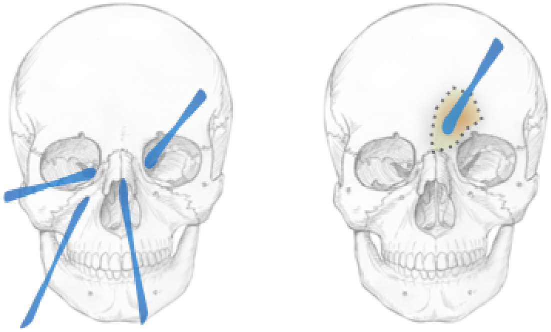

Figure 3.1: Endoscopic skull base surgery vs craniotomy

On the other hand, high density of critical neurovascular structures at the skull base and anatomical variability make the surgical planning more complex and time-consuming. Furthermore, utilizing more surgical pathways for additional instruments may improve the visualization or target removal, but it would also contribute to the complexity of pre-operative planning.

Currently, planning for surgical approaches is limited and typically involves review of patient CT or MRI images in 2D-axial, coronal, and sagittal, without 3D reconstruction. Furthermore, skull base surgeons manually change the visualization effect to better view the anatomy and examine possible approaches to the lesion.

While surgeons are visualizing the data slice by slice, they have to mentally reconstruct the pathways and keep track of all structures inside or adjacent of the pathway to ensure patient's safety. While for some tumor location the surgical approach is obvious, for other tumor locations in the skull base, the optimal choice of surgical pathway may not be intuitive.

This cumbersome process relies heavily on surgeons' experiences without any metrics to assess or compare the approaches. Therefore, in the pre-operative planning stage, often multiple surgeons collaborate to locate the boundary of the target and choose the *best* surgical approaches by considering all available data such as pre-operative medical images, patient health history and conditions.

The choice of surgical approache(s) is critical not only for optimization of visualization and target manipulation capability, but also to minimize collateral tissue damage for both pathway and target trauma. Pathway trauma refers to damage incurred by gaining surgical access to reach the target and repetitive passage of instruments, as well as tissue retraction injuries.

The clinical need that motivated this work was the difficulty of the surgical pathway planning, the amount of time and resources required and the lack of metrics to compare and assess different approaches. The goal is to aid the skull base surgeon in designing and selecting the optimal surgical approaches to target locations.

This was achieved by 3 different schemes:

- Providing the surgeons the total control while offering an efficient method of examining different approaches with better visualization.
- Providing the surgeons with an *optimal* approach based on their preferences as weights and by optimizing a scalar cost function.
- Providing the surgeons with *optimal* approaches by optimizing the multi-objective cost function and allowing the surgeons to select their preferred approach among all *optimal* approaches.

3.2 Background and Literature Review

In other areas, such as abdominal, heart, neurosurgery or invasive robotic surgery, several studies have proposed methods to better assess and reduce risk of surgery by planning trajectories [35],[36],[37] and [38]. Some of these tasks include methods for planning safe keyhole neurosurgery [39], identifying trajectories in Deep Brain Stimulation (DBS) [40], or planning of non-straight trajectories [38].

In planning for Robotic Minimally Invasive Surgery (RMIS) intervention, Adhami et al.

[41]proposed a two-step optimization strategy: the port placement of the robot (incision sites) and the pose of the robot (initial configuration of stationary joints). The first part was achieved by optimizing the cost function based on visibility and dexterity. These criteria were based on patient specific models and surgeon's knowledge. The pose planning, aims at ensuring a collision free operation of the robot throughout the intervention.

In planning trajectories in the abdomen, most methods concentrate on calculation and simulation of the ablation zone and the resulting optimal probe placement with respect to the coverage of the tumor.

Baegert et al. [42] proposed a method based on a constraint concept for automatically computing insertion trajectories. An insertion trajectory consists of the given target point and an insertion point on the skin. Hard constraints (collision free trajectories) were used to determine the insertion zones on the skin and soft constraints (distance to critical structures) were used for rating those trajectories. Several soft constraints could be combined using a weighted sum in order to obtain an overall rating of a given trajectory.

In trajectory planning for percutaneous needle insertions (interventions in the liver), Seitela et al.[43] used the concept of Pareto optimality for a weight-independent proposal of insertion trajectories. Similarly to Baegert et al. the hard constraints were defined and evaluated to eliminate the trajectories that did not satisfy a condition. In this study, the soft constraints were used to obtain the Pareto frontier set.

In brain surgery such as placing a micro-electrode to alleviate Parkinson's disease, Lee et al.[44] proposed a method to fuses patient MRI head images with a registered atlas to support the manual selection of a trajectory with a visualization of the 3D atlas structures.

In image-guided neurosurgery, Vaillant et al. [45] proposed an algorithm for determining optimal surgical paths in the brain . Each point on the outer surface of the brain were treated as an entry point. The risk of a candidate trajectory were defined as a weighted sum and based on the trajectory intersected intracranial structures and their associated importance. The cost of trajectory associated with each critical structure, and total cost were presented to surgeon to define a low cost trajectory. This method did not consider the distance from the trajectory to critical structures; thus, the damage that can be caused by surgical tool misplacement was not incorporated in the function.

In image-guided keyhole neurosurgery, Shamir et al. [40] presented a preoperative straight trajectory planning method for reducing the risk associated with insertion of straight tools. In this method, risk volumes (risk maps) were defined based on the importance (estimated consequences of the damage) of the brain tissue and distance to critical structures. Neurosurgeons were presented with interactive 3D visualization to define or edit the trajectories. The risk values were computed for input trajectories and were presented to the neurosurgeons for selecting the safest trajectory.

In planning for placing the electrode in Deep Brain Stimulation (DBS), Essert et al. [46]proposed a method for the optimal placement based on strict and soft constraints defined by neurosurgeons. The strict constrained were used to define the space of all possible solutions. The soft constraints were aggregated using surgeons defined weightings and were used to find the optimal linear trajectories. The shape of the trajectory was defined as a line which cause inaccuracy in the planning because of the brain shift.

In context of the endoscopic skull base surgery, Becker et al. [47] developed a software program for manual planning and evaluation of multiple trajectories toward a designated target within the temporal bone. The user has to defined the entry points, drill path radius and safety distance to the critical structures. The pathways which satisfies the constraints were generated and color-coded based on their distance to the critical structures. Surgeons were able to select a set of three drill canals among all generated pathways to reach to lateral part of the skull.

3.3 Manual Surgical Pathway Planning

The difficulty, required time and resources for pre-operative surgical pathway planning for skull base surgery, were unmet needs that motivated this section.

A rapid pre-operative planning system for skull base surgery is described using the following two novel concepts: *importance-based highlight* and *mobile portal.* A novel concept of mobile portals will allow surgeons to quickly review all potential pathways in a 3D model. This avoids the need for slice by slice 2D visualization of conventional computed tomography (CT) and magnetic resonance imaging (MRI) viewers. The new visualization method of CT data based on the relative importance of structures, depending on their distance to vital structures will allow surgeons to identify structures inside or close to pathway. The skull base bones are segmented into different contours with emphasis on critical structures, which include the internal carotid artery, cavernous sinus, and cranial nerves.

To achieve this, the following methods were used: 1. novel bone-only atlases were manually generated, 2. orbits and the center of the skull serve as features to quickly pre-align the patients scan with the atlas, 3. deformable registration technique was used for fine alignment, 4. surgical importance was assigned to each voxel according to a surgical dictionary, and 5. pre-defined transfer function was applied to the processed data to highlight important structures. The proposed idea was fully implemented as independent planning software and additional data are used for verification and validation.

The experimental results show: 1. the proposed method were greatly improved planning efficiency while optimal surgical plans were successfully achieved, 2. the method successfully highlighted important structures and facilitated planning, 3. the workflow required shorter processing time than classical segmentation algorithms, and 4. the method can be used to improve surgical safety for surgical robots.

3.3.1 Method

Figure 3.2, shows the workflow of the proposed system which has 3 main components. In preprocessing the features and bone structures are extracted from CT data followed by registration. In the registration, the results from previous stage are used to pre-align the data with the atlas for rapid registration and segmentation of bone structures. In volume rendering stage bone structures are visualized based on their importance level (previously assigned). In final step, surgeons can explore different possible surgical pathways by using the mobile portal feature. Being able to manipulate the portal in 3D quickly, provide the surgeon a total control to plan a patient-specific pathways.

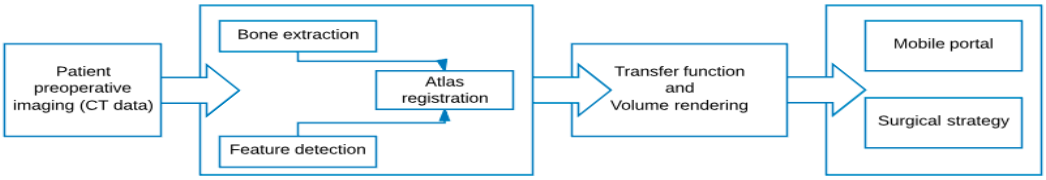

Figure 3.2: Manual surgical planning workflow

Next each component of the workflow is described in details:

- Atlas and Feature Based Rapid Registration and Segmentation:

  Image registration is a time consuming process. Registration efficiency was increased by focusing on bone windows and utilizing obvious features to pre-align to anatomical atlas.

  Bone extraction: Simple intensity global threshold was used for bone extraction, which requires manipulation of only one parameter and improves efficiency [48].

  Feature extraction: The goal of this step is to pre-align the test and atlas volumes to streamline registration process. For automatic alignment, the software finds the orientation of the patients skull and matches it with orientation of the atlas data set. The orbits and the center of skull are used for orientation. Edge Canny detection was used due its optimal performance with noise, localization, and the amount of the details that could be controlled [49]. The feature used for the identification of the orbits is the approximate circularity of the orbits and the Hough Transform (HT) was used to detect the circular objects [50]. To completely describe the orientation of the data set, the center of the image was used as the third feature. Thus, the two data sets were spatially aligned for rapid registration.

  3D Registration and segmentation: Image registration is the process of finding the optimal transformation $T : (x, y, z) \rightarrow (x, y, z)$ which maps any point in the test volume to a corresponding point in the reference volume while minimizing the cost function. We used a combined transformation T which consists of global and local transformation. This step aims to correct for global differences in position, orientation, and size between an atlas and a subject volume. We used 9 degrees of freedom as the registration model, where the free parameters include three translational, three rotational, and three scaling factors. To find the optimal transformation parameters, we minimized the mean squared pixel-wise difference between the atlas and the subject volumes using a gradient-descent optimization scheme.

An additional transformation was required to model the local deformation of the skull because the bone volumes are different in both size and shape across patients and global transformation is not sufficient to capture this variation. Therefore, we used B-splines, which are a well-known approach for non-rigid registration of 3D medical volumes [51]. In this method, a mesh of control points with uniform spacing is defined, which act as parameters of the B-splines method. The degree of this non-rigid deformation is tuned by changing the resolution of the mesh of the control points. To achieve accurate and efficient registration, we used the same cost function, minimizing mean squared pixel-wise difference, and the Limited-memory BFGS optimizer. LBFGS is an optimization algorithm in the family of Quasi- Newton methods that approximates the Broyden Flecther Goldfarb Shanno (BFGS) algorithm using a limited amount of computer memory. Limited-memory make this optimization technique suited for problems with large number of variables [52].

For assessing the algorithm, we warped the atlas volume and used it as our patient data set, where we have the ground truth to evaluate the segmentation result. To create the test volume, we used a landmark deformation method to deform the atlas. Figure 3.4 from left to right, shows the axial slice visualization of the atlas data set, the deformed visualization of the same slice, the difference between the original image and the warped image, visualization of a slice from the 3D registration result, and its difference with the original image. Finally, once the registration problem is solved, in the case of the single atlas, the easiest and fastest way to assign a label to each input

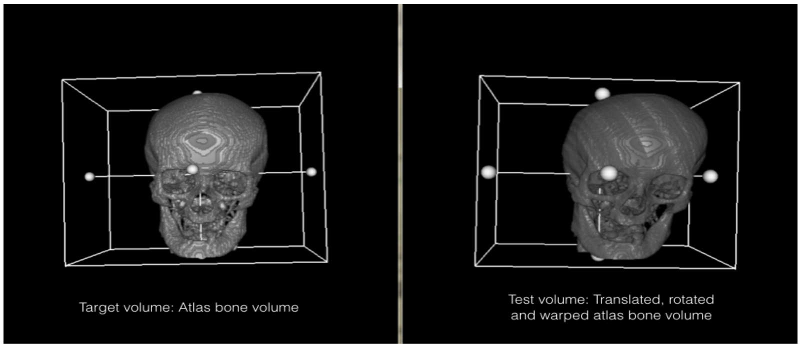

Figure 3.3: Left to right, 3D Bone visualization of atlas data and warped atlas data set as test data

Figure 3.4: Representivie slice from 3D registration, left to right: fixed Image (atlas), moving Image (warped atlas), registration result, rescaled difference of moving image and fixed image, rescaled difference of registered image and fixed image

image voxel is to propagate the atlas labels to image space [53]. With this strategy, the segmentation process relies on a registration process that aims to estimate the anatomical differences between the atlas and the input image volumes. In the case of single atlas, we assumed that the atlas is close to the subjects anatomy.

- CT Bone Atlas and Anatomy Based Importance Dictionary Definition:

  CT bone atlas: The atlas was created by manually segmenting the bone structure through collaboration with Head and Neck surgeons at the University of Washington. The atlas contains 20 different bone contours inside the skull base area the following figure shows a representative axial slice of the bone Atlas.

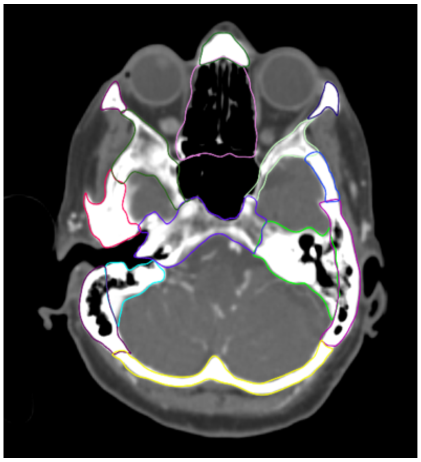

Figure 3.5: A representative slice of the bone Atlas

Importance dictionary: In medical imaging physicians often are interested in certain spatial regions where the data should be emphasized. Any prior knowledge can be used to highlight different areas in the final volume rendering.

In skull base surgeries bone anatomy is important because of its stable position. Furthermore, surgical navigation systems uses bone as landmarks for accurate tracking. Due to this characteristic of the bony structures, we utilized the bone segments and voxels by assigning then a relative value based on their proximity to critical structures (e.g. carotid artery and optic nerve) or surgeon's prior knowledge.

Visualization effect: The crucial step in volume rendering is to design the transfer function. This function determines which structures or region of the volume will be visible and how they will be rendered [54]. To better convey the information in CT volume data, we utilized the importance-based information to find the optimal window level, opacity, and color to highlight the influential structures. For example, bone structure adjacent to optic nerve would have a higher opacity and brighter color, while Ethmoid bone structures would be more transparent with regular bone color. Since this transfer function is designed based on importance of different structures and segmentation, it is generalizable to all data sets. Figure 3.6 highlights the bone structures near the optic nerve and extra-ocular muscles. Note that direct volume rendering was used to create

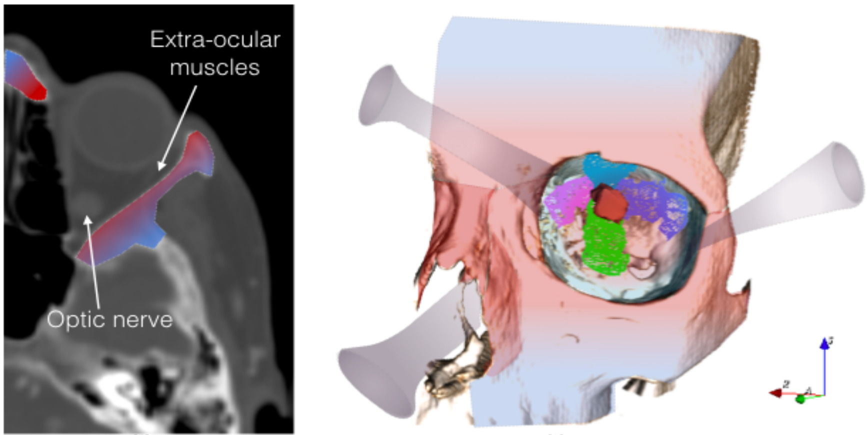

(1) (2)

Figure 3.6: Zygoma and nasal bone highlighted based on distance to critical structures (1) and 3D view of importance based visualization (2)

the 3D model. To visualize the bone segments, we used pixel wise rendering vs mesh generation of segments. This visualization technique helps surgeons to have access to the raw pixel information in the case of mis-registration. We used shades of red to color segmented bones according to their importance. Bone structures which belong to contours with high importance level were red and relatively less important structures were white, Fig 3.7.

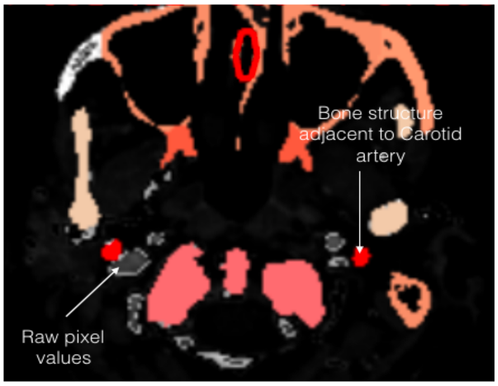

Figure 3.7: Pixel wise importance based visualization effect

- Mobile Portal for Fast Surgery Planning:

  Using the 3D model, or any 2D views, surgeons can determine the target and defined the pathway to the target, whether it is on the skull surface, Trans-nasal or Trans-orbital approaches. Next surgeons can manipulate the virtual pathway to examine various approaches to the target, the geometry, location and dimension of the pathway can be adjusted in an iterative process till it satisfies the surgeons requirements.

  Figure 3.8, shows screen shots of manipulating the surgical pathway. Surgeons can examine each pathway using 2D or endoscopic view. With emphasized critical structures they can easily find the optimal pathway. The selection of the target (yellow sphere) and two different pathways (labeled 1 and 2) to the same target are shown in the following figure. Comparing these two pathways, it is shown that pathway 1 contains less critical structures than pathway 2 and in general the amount of bone removal would be less for pathway 1. In addition, surgeons can switch to the raw CT scans visualization to examine structures inside the selected pathway.

The rapid planning, the new CT visualization and 3D pathway visualization to the target was added as features to a prototype Skull Base Pre-operative Planning software **??**. This new visualization is based on emphasizing the relative importance of skull base bone structures. In this software, after specifying the target surgeons can manipulate the by moving the portal to examine different approaches. The atlas-based registration was used to segment bones into different structures. Using the prior knowledge we assigned a relative importance level to each bone segments. To improve the visualization, different transfer functions were generated according to the importance assigned to bone segments. Therefore, surgeons can quickly see all vital structures inside the pathway. The features improved the surgical planning in the following ways: 1. the ability to rapidly explore different pathways to the pre-specified target, 2. the ability to visualize the structures inside the pathway according to their relative importance level, 3. the ability to manipulate the portals and change the geometry of each pathway with minimal interaction, and 4. the 3D visualization for efficient

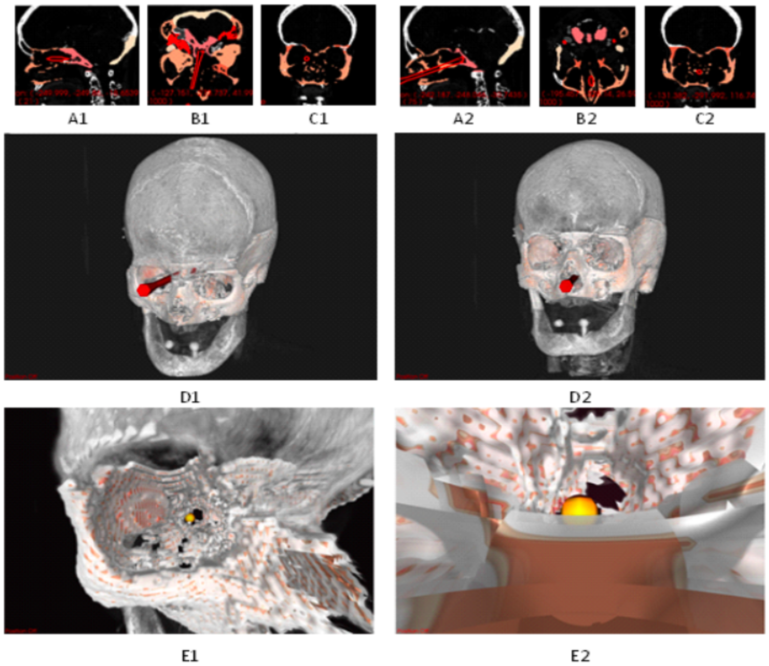

Figure 3.8: Importance based visualization for pathway review

planning.

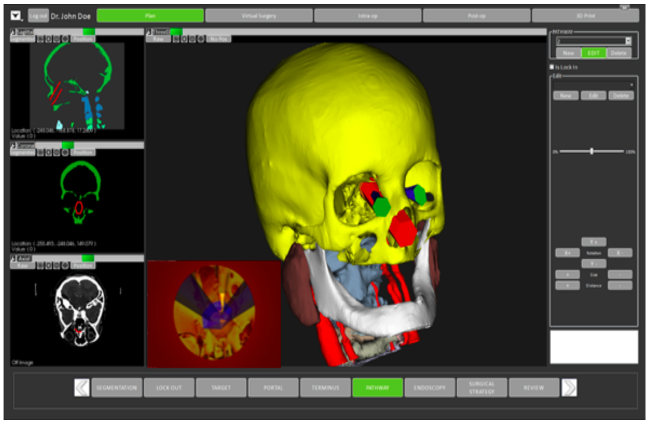

Figure 3.9: Skull Base Pre-operative Planning software with mobile portal feature

Future work such as construction of a rich collection of atlases representing different patients, or defining a more detailed dictionary by utilizing the prior knowledge can improve the pre-operative planning stage.

3.4 Semi-Automatic Surgical Pathway Planning

In previous section, a manual pre-operative planning software was introduced that allowed the surgeons to manipulate and drag the portals in 3D patient model. Surgeons could examine and visualize different approaches more efficiently. The proposed method made the planning faster and more accurate with the feature of 3D model of the pathway and the structures.

In addition to time and visualization, surgical planning does not incorporate objective metrics related to a surgical approach in terms of distance measurements, amount of tissue/bone removal, and ability to perform surgical tasks at the target site. It is challenging to demonstrate quantitatively that one approach is better than another.

Surgeons often rely on their training background and experiences in pathway selection, therefore it is difficult for trainees or patients to understand the rationale behind their choices. Further, there is no quantitative information to support the decision process [55].

The clinical need that motivated this section was to answer the question of **how to compare the surgical approaches**. In the other words, what makes one pathway acceptable by surgeon and not the other one. If the pathways can be compared, the problem of finding the *best* surgical approach can be written as an optimization problem.

The surgical decision-making can be described by factors such as individual patient anatomy, tumor location, pathology, surgical instrumentation, and visualization technology and therefore pathways can be compared by these factors too.

The two main goals of this section are: 1. To identify and translate the skull base surgeons decision-making objectives into the cost function and constraints 2. To develop an automatic preoperative planning tool to obtain patient-specific optimal surgical pathway.

3.4.1 Method

Our proposed method has the following four main parts (patient specific treatment, pathway design, cost function, and optimization) that are described in details:

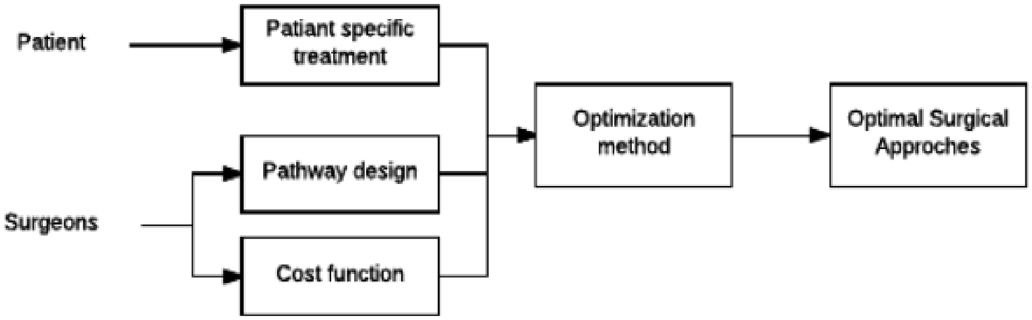

Figure 3.10: Overview of automatic surgical pathway planning

Patient Specific Treatment

- Input data

  CT images due to their high contrast bone structures are the main image modality used intra-operatively in skull base surgery. Therefore surgeons usually use this image modality for preoperative planning too. Real clinical patient data with various target locations were used to develop and test the method.

  All necessary structures were extracted from CT pre-operative images manually or semi-automatically to be used for pathplanning. The segmented structures contained: bony structures (frontal, nasal, orbital bones), soft tissue, and orbital structures (globes, optic nerves and extraocular muscles).

  For structures such as bone and soft tissue, simple thresholding using Hounsfield Unit (HU) values produced reasonable segmentation results [48]. However, the skull base surgeon in our team verified the segmentation results by visual inspection of all slices using 3D slicer software.

  The orbital structures such as globes, optic nerves and extraocular muscles were automatically extracted using the method described in previous chapter where the prior anatomical and shape knowledges were used to segment these small structures. Binary volumes obtained from the segmentation step were overlaid on the original images and were confirmed or edited by the expert surgeon for each structure. The target was segmented manually by an expert surgeon using the painting tool in 3D slicer software. All of our testing data sets were in advanced tumor stages which meant the tumor was developed outside the confines of the nose and sinuses and in some cases even eroded the bone structures [56]. While the goal of skull base surgeons is to remove all the lesions, access to some regions is more challenging. For instance when the tumor is near to critical structures or extended into non-common regions. Preoperative planning and analysis of *hard to access* regions would be more beneficial to surgeons. In our study, only *hard to access regions* of each data set were labeled as target. Therefore a case could have multiple targets, which were treated separately, Figure 3.11.

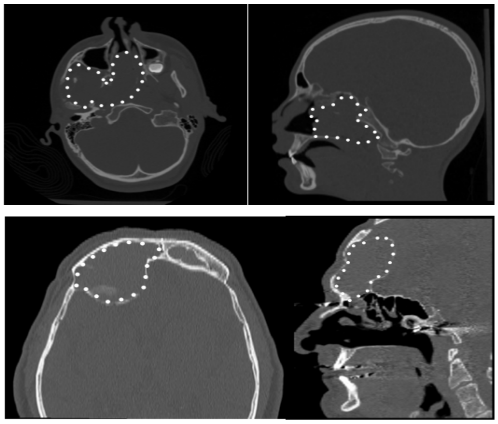

Figure 3.11: Representative slices of tumor for two patients

- Initial insertion zone and feasible region

  Insertion zone was defined as a plane parallel to the coronal plane and was specified by the surgeons. In order to consider all possible pathway candidates, the insertion planes were set in such a way that covered the whole facial region. Furthermore the feasible region was characterized as a cuboid that contained the insertion plane and a parallel plane posterior of the target. Therefore the feasible region contained the target completely and all other structures inside the cuboid.

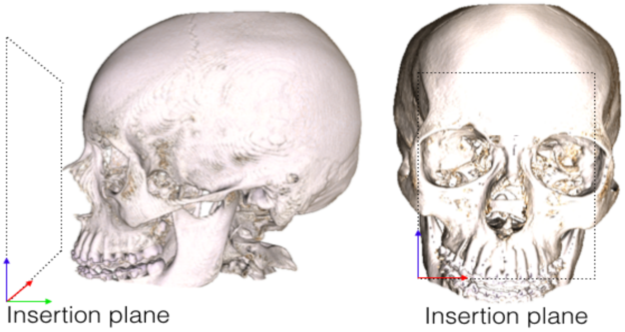

Figure 3.12: Insertion plane

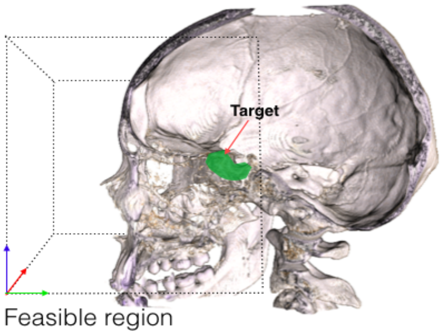

Figure 3.13: Feasible region

- Preprocessing

  Using the segmentation of anatomical structures and the target, all voxels in the feasible region were labeled as either air, general tissue, critical structure tissue or target. In addition the distance of each voxel to the critical structures such as optic nerves and extraocular muscles was pre-calculated. To reduce the computation time and rapid access of the data, the 3D position, labels and distance measurements of all the voxels in feasible region were preprocess and passed as input to the optimization algorithm.

Pathway Design

Surgical pathway (portal) is a path that a surgical instrument such as Endoscope/Microdebrider, travel through to reach to the pathology from surface of the skull. The pathway could be created using the surgical instruments or could be natural opening on the face (Trans-nasal) which provides access to the target.

The pathway must allow enough dexterity for surgeons to manipulate the target, therefore the shape of the pathway is a critical factor in the success of the surgery. The long and rigid instruments used in skull base surgery indicate a cylindrical or biconical surgical pathway. Bly et al. [1] used a polygon with six vertices at the entrance and target location as a Trans-orbital surgical pathway to the lateral cavernous sinus, Figure 3.14. In their study they showed that Trans-orbital approach can be replaced by open surgery with proper pathway since the amount of globe retraction was reduced. Compared to cylindrical shapes, the unbalanced biconical pathway, Figure 3.15 allows better maneuverability at the target with smaller volume. A free DOF for pivot point enable the algorithm to produce a variety of general pathway shapes. Furthermore, the unbalanced biconical pathway is consistent with surgeons description of the pathway which relies on bony structure as a pivot point to remove the target. A spherical volume was added to the target side (the end of the pathway) to represent space for the instruments tip and its treatment volume.

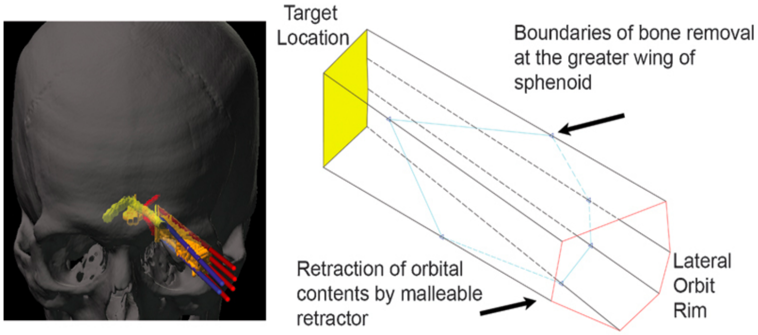

Figure 3.14: Polygon surgical pathway [1] (Trans-orbital approach)

In this study, the cylindrical biconical shape was used as a general pathway model and was parametrized by its end positions (center of the base circles), height of pivot point, and radius. The radius was set to 10 mm and 8 mm (at the pivot point) because of the instrument limitations. The other parameters were defined as decision variables of the optimization.

Therefore each surgical pathway was characterized by six parameters: Entry point was defined as a 2D position on the initial insertion plane, End (exit) point a 3D position and center of the spherical volume, and parameter d which was the distance of the entry point to the pivot point of the pathway.

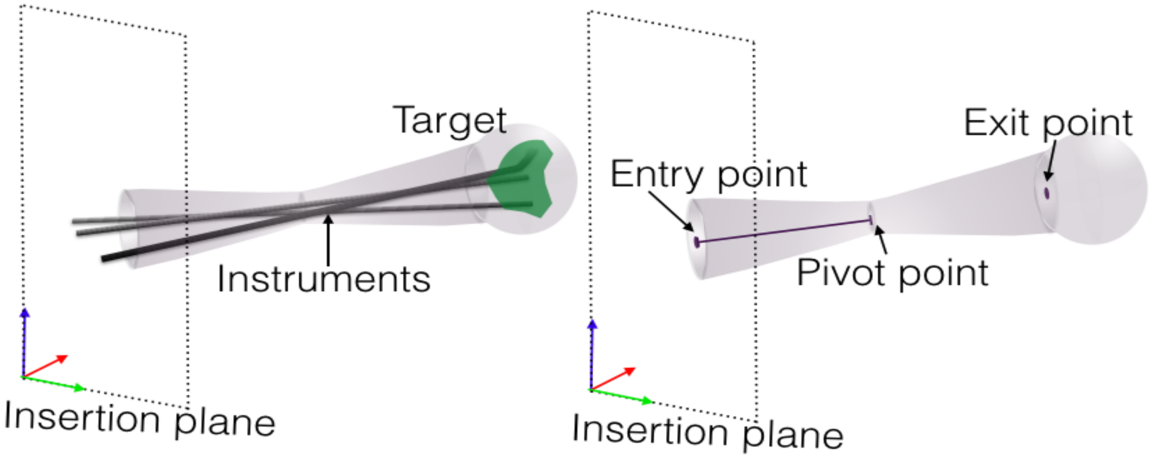

Figure 3.15: Defined surgical pathway

Cost Function

- Objectives To develop an automated computer aided surgical planning tool, its important to understand the thought process of the surgeons in preoperative planning and translate their descriptions into a mathematical structure.

  Two expert skull base surgeons at University of Washington were interviewed to gather the implicit and explicit rules used when deciding the best possible approach to the target. The surgeons were asked to plan their approaches for different cases using the Skull Base Preoperative Planning tool [57] while explaining their preference. Although the process of planning is a complex task, the following fundamental rules for pathway placement were described by both surgeons and were used to construct the final cost function:

- *Target coverage*: The optimal pathway must provide the surgeon enough access and dexterity to remove the target. The pathway exist point must be in the target region. Therefore the space of possible solutions was restricted.
- *Hard tissue or bone removal*: While surgeons attempt to avoid removing the bone tissue to minimize trauma, in some cases removing the bone is necessary due to the target location. Considering the complications or cosmetic issues after surgery, the effect of removing bony structures in different regions are not same. Since for some regions its possible to replace and secure the removed bone with plates and screws. For instance, nasal bone removal are avoided compared to orbital bone.
- *Soft tissue removal*: Soft tissue removal is another objective that surgeons consider when selecting the surgical approaches. Similar to the bony structures, the consequences of removing different tissues will not be the same. Accordingly, tissues can be divided into three general groups: 1. Tissues that cause a little or no complication for patient after removal. 2. Tissues that can be retracted. E.g. eye globes - septum 3. Tissues that are risky and must be avoided possibly by a distance. E.g optic nerves and extra-ocular muscles.
- *Distance to critical structure*: Surgeons prefer the pathways away from the critical structures such as optic nerves to prevent possible damage to these vital structure intra-operatively. Therefore, the goal is to maximize the minimum distance of the pathway to all critical structures. However, the surgical pathway may need to come close to these risky structures because of the target location. In these cases, a minimum distance margin was defined as a hard constraint to restrict a pathway from contacting the risky structure. This margin, and the flexibility of the structure itself is usually enough to treat the targets which are near critical structures safely.

In order to find the best pathway, the rules described by the surgeons must be formalized into a cost function and constraints to be optimized. The patient data (segmented

3D images) and feasible region were inputs and the parameters of the pathway were the outputs of the optimization. To formulate the cost function the patient image voxels were divided into three groups:

- *Structure 1 (S1)* - general tissues (e.g. bone, soft tissue): Removal of S1 structures may be necessary, however patients usually recover from such a removal. However, some regions such as frontal or nasal bone are assigned a higher importance value or weight.
- *Structure 2 (S2)* - risky tissues (e.g. optic nerve, extra-ocular muscles): Removal of S2 structures will cause a serious complication for the patient. The pathway should not travel through these structures and have at least 2 mm distance. To ensure that, the minimum distance to the risky tissues was defined as a hard constraint.
- *Structure 3 (S3)* - critical but deformable tissues (e.g. globes, septum): A pre-planned surgical path may intersect with $S3$ structures, since they can be retracted to allow instruments movement. To model this feature, $S3$ structures were divided into two regions based on their possible and safe displacement without injury. Therefore, $S3'$ is the region that must not be intersected by the paths to avoid injury and was defined as a hard constraint. Figure 3.16 demonstrate example of deformable tissues. In this case, pathway in Figure 3.16 only contains S3 and not $S3'$, therefore by deforming the structure during the surgery the pathway does not cause any injury. On the other hand, pathway in Figure 3.17 contains $S3'$ and even by deforming the structure the pathway will penetrate through the structure. In case of the globes $S3'$ was defined as sphere centered at the globes center with a radius (r) defined based on deformability of the globe. Having the pathway diameter of 10 mm, the average globe radius of 24 mm and 10 mm the maximum allowable retraction on the globe [58], the radius r was selected as 14 mm. The maximum deformation is a parameter that can be set by the surgeon.

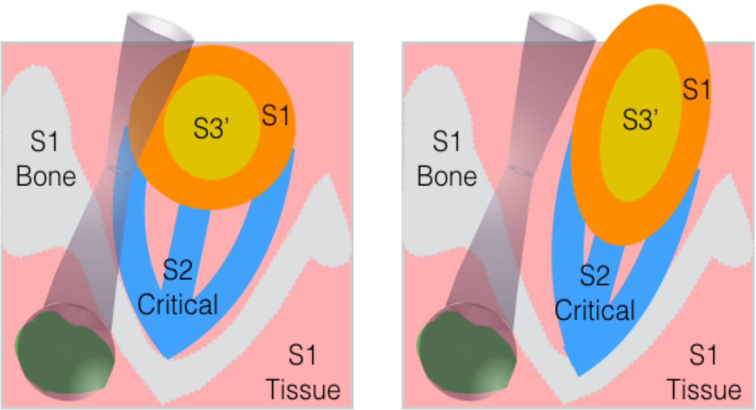

Figure 3.16: Schematic of the deformable tissue model, pathway is not penetrating through $S3'$

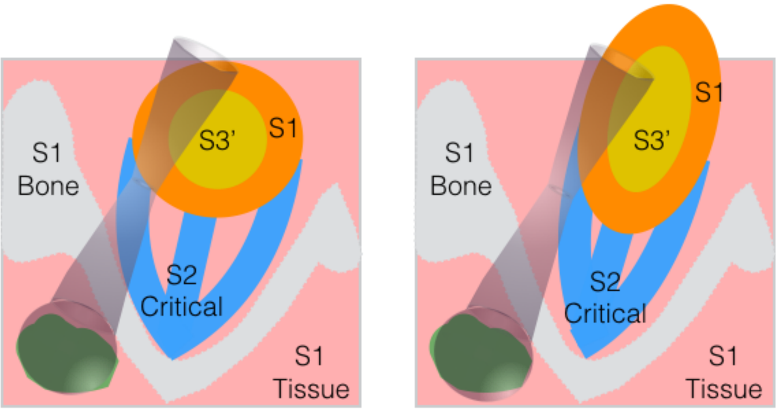

Figure 3.17: Schematic of the deformable tissue model, pathway is penetrating through $S3'$

$$S3' : (x - x_{globeCenter}) + (y - y_{globeCenter}) + (z - z_{globeCenter}) < r$$

$$\text{where } S3 \subseteq S3'$$

$$P \cap S3 \neq \emptyset \text{ and } P \cap S3' = \emptyset$$

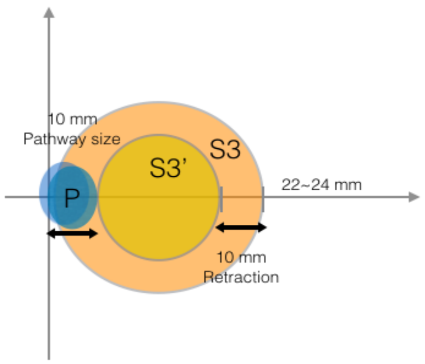

Figure 3.18: Schematic of the deformable tissue model

- Single pathway

  For planning single surgical pathways, we used the soft constraints to model the cost function which included: minimize the number of S1 voxels (bone, soft tissue, skin), minimize the number of S3 voxels, maximize the number of target voxels, and maximize the closest distance from the pathway to critical structures (optic nerves and extra-ocular muscles). We defined hard constraints of ($|d| > 2$ mm) for distance to critical structures and zero number of $S3'$ voxels inside the pathway. This cost function defined a multi-objective problem which was solved by combining its objectives into one single-objective scalar function subject to the above constraints. This approach is known as the weighted-sum method [59].

$$Minf(x) = \sum_{a=1}^{N_a} w_a(P \cap S_a) - w_b(P \cap T + O \cap T) - w_c \sum_{i=1}^{n_2} (dist_{min}(S_{2_i}, P)) \qquad (3.1)$$

s.t.

$$P \cap S3' = \emptyset$$

$$dist_{min}(P, S_{2_i}) > d_m \quad \forall j \in \{1, \ldots, n_2\}$$

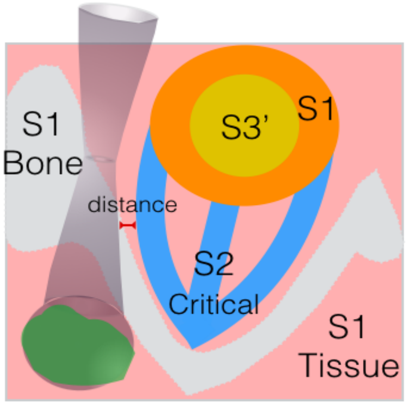

Figure 3.19: Schematic of single pathway

$$
\textit{where}\begin{cases}
P & \text{pathway}\\
w_a, w_b, w_c & \text{weight associated with the corresponding objective}\\
S_a & \text{different types of structures, } (a = 1,\ 2,\ 3)\\
S_{a_i} & \text{denotes the ith object in structure type } a\\
 & \text{e.g critical structure 2: consists of optic nerves and extra-ocular muscles}\\
T & \text{target}\\
O & \text{spherical volume of operation region}\\
S_{3'} & \text{region of deformable structure 3 that must be avoided}\\
d_m & \text{minimum distance of the closet point of the path to the structures of type 2}
\end{cases}
$$

- Multiple pathways

  Since skull base surgeons may use multiple instruments to remove the target, it was important to consider finding two surgical pathway simultaneously, Figure 3.20. With two pathways, the number of decision variables is doubled, 6 parameters for each pathway. The cost function had the same objectives as for the single pathway, however two more objectives were added. 1) to avoid collision of the surgeons hands at the entry points of the pathways, the angle between the pathways must be considered. Bly et al. [60] found that an angle of approximately 20 degrees between 2 portals is necessary to function effectively at skull base targets. 2) to ensure complete removal of lesions, each pathway should cover non-overlapping regions of the target, therefore the distance between two exit points of the pathways must be maximized while the boundary conditions are satisfied.

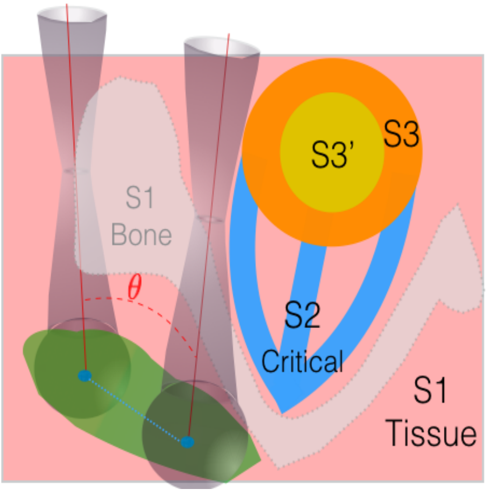

Figure 3.20: Schematic of multiple pathways

$$Minf_2(x) = \sum_{1}^{k=2} \left[\sum_{a=1}^{N_a} w_a(P_k \cap S_a) - w_b(P_k \cap T + O_k \cap T) - w_c \sum_{i=1}^{n_2} (dist_{min}(S_{2_i}, P_k)) \right] - w_d dist(P_1^{exit}, P_2^{exit}) \tag{3.2}$$

s.t.

$$P \cap S3' = \emptyset$$

$$dist_{min}(P, S_{2_i}) > d_m \;\; \forall j \in \{1, \ldots, n_2\}$$

$$\theta(P_1, P_2) > \theta_m$$

$$where \begin{cases} P_k & \text{ Kth pathway} \\ w_a, w_b, w_c, w_d & \text{weight associated with the corresponding objective} \\ S_a & \text{different types of structures, (a = 1, 2, 3)} \\ S_{a_i} & \text{denotes the ith object in structure type a} \\ & \text{e.g critical structure 2: consists of optic nerves and extra-ocular muscles} \\ T & \text{target} \\ O_k & \text{spherical volume of operation region} \\ S_{3'} & \text{region of deformable structure 3 that must be avoided} \\ d_m & \text{minimum distance of the closet point of the path to the structures of type 2} \\ \theta & \text{angle between two pathway} \\ \theta_m & \text{minimum angle between two pathways} \end{cases}$$

Optimization

Since different objective functions can have different magnitude, their sum would be meaningless and normalization is required. The normalization scheme described in [Mausser] was used. Each objective function is normalized by the differences of optimal function values in the estimated Utopia (z_i^U) and Nadir (z_i^N) points.

Utopia (z_i^U) points represent the lower bound of each objective in the entire feasible search space, and it is obtained by minimizing each function individually subject to the constraints.

Nadir (z_i^N) points which are usually difficult to compute in practice, represent the upper bound of each objective in the Pareto-optimal set [61].

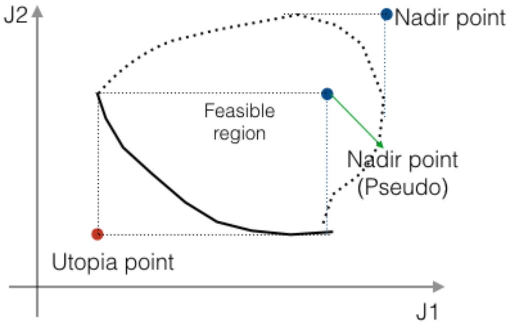

Figure 3.21: Utopia and Nadir point definition

$$f_i^{norm} = \frac{f_i - z_i^{U_{estimated}}}{z_i^{N_{estimate}} - z_i^{U_{estimate}}}$$

One method of the estimation is to sample random points of x (decision variables) subject to a subset of constraints and to calculate $z_i^{U_{estimate}}$, $z_i^{N_{estimate}}$ as the minimum and the maximum over the set of sampled points [62]. We obtained our samples of decision variables by dividing the feasible plane into small grids $N = 5$ or 10, while keeping 4 of the parameters constant (3D position of exit points and height of pivot point). Then each objective function was evaluated over the sampled points and the minimum and maximum were found. The obtained values provided useful information about range of each objective function. In addition, to ensure that the decision variables in the feasible region were normalized correctly, the obtained values ($z_i^{U_{estimate}}$, $z_i^{N_{estimate}}$) were adjusted to smaller and larger values respectively, based on anatomical prior knowledge. For instance, for the bone removal objective, $z_i^{N_{estimate}}$ was set to zero which represented a pathway with no bone removal, even though, the decision variables corresponding to such a pathway were not in the sampled points set. After normalization, the objectives were aggregated with surgeon defined weights such that $\sum_{i=1}^{i=N} w_i = 1$ and $w_i \geqslant$

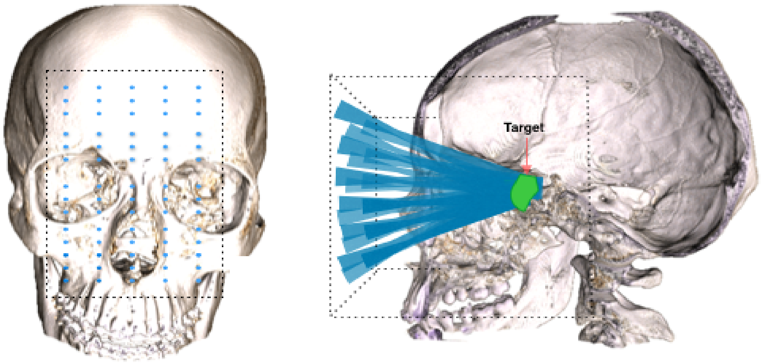

Figure 3.22: Estimating the Utopia and Nadir points

0. The obtained single objective cost function (equation 1 and 2) were optimized using Simulated Annealing method (SA) [63].

SA is general local search technique, that has been applied to optimization problems in many fields [64]. The main advantage of the algorithm is that allows for non-improving solutions in order to escape from local minima. The acceptance and rejection of the worse solution is determined by a probability function [65]. Geman et al. [66] showed that SA, if annealed sufficiently slowly, converges to the global optimum. To ensure the quality of the optimal solution, the surgeon defined four different initial values which were reasonable to treat the target. Therefore the obtained optimal pathway probably will have better cost value compared with initial starting points.

In this presented approach, still the surgeons are the key decision maker, their preferences are the weights to each objective function. In this case, the decision-making is before the search. Providing this freedom to surgeons is critical and will increase the patients safety and outcome. Consider the following scenario: the patient has a tumor in a region that can be access with craniotomy (through frontal bone) or trans-orbital. Each approach has their own risks and complications, however surgeons knowledge of the patient can be used to find the optimal surgical approach.

The described approach was designed to be extendable and can easily be adapted by changing the cost function, adding more structures, changing the pathway shapes, considering other characteristics of the tissue such as deformability or patient's pre-conditions. Future work, machine learning algorithms can be used to learn from other patient's data with similar target locations or the surgeon's previous cases. This information can be added to the optimization as prior knowledge. In addition, the surgical pathways planning can be extended into other medical institution. In other words, the training from

3.5 Automatic Surgical Pathway Planning: Pareto Optimal Set

In the previous section, the cost functions for single and multiple pathways planning were obtained by identifying surgeons decision making factors while they were planning for multiple cases using a prototype Skull Base Pre-operative Planning software **??**. The normalized result of each objective was considered in a weighted sum. The individual weighting w_i were manually selected based on surgeons preferences such that the $\sum_{i=1}^{N} = 1$. Therefore the optimal pathway was obtained according to the aggregate cost function subject to defined constraints.

In this section, we extend that work to provide an automatic way of planning a trajectory, using the *Pareto optimality* concept [67]. In this method, the cost function is defined and solved as a Multi-Objective Optimization Problem (MOOP) [68]. Therefore, surgeons are provided with a *set* of optimal solutions rather than a solution. The pathway will be obtained from the set according to the surgeon's preference and examining the set of Pareto solutions. Rather than chossing weights, surgeons will make the decision after performing the search.

A multi-objective optimization typically appears in many engineering modeling, financial, and other domains where the decision maker must choose among several competing objectives to satisfy [69].

A general multi-objective optimization is defined as:

$$min\{f_1(x), f_2(x), ..., f_k(x)\}$$

s.t.

$$g_j(X) = b_j \ \forall \{j = 1, ..., k\}$$

$$B_{min_n} < X < B_{max_n}$$

To solve the optimization problem is to minimize/maximize a set of objective functions by finding a decision variable $X = [x_1, ...x_n]$ which is generally restricted by a set of constraints or bounds.

In many real world problems, the objectives that are considered may conflict. For instance, for a given pathway, the amount of bone/tissue may be optimized, but it may be too close to a critical structure. So there is a trade off between the distance and amount of tissue removal. Due to the conflicting nature of objectives, finding a X that simultaneously satisfies all objective functions is not possible. A reasonable solution to a multi objective problem is to explore a set of solutions (notion of Pareto optimality) instead of one.

In minimization of multiple objectives, a vector $X^\star$ is in the *Pareto optimal set* if all other vectors X in the feasible space have a higher value for at least one of the objective functions f_i, or have the same value for all the objective functions. In the other words, a Pareto optimal solution cannot be improved with respect to any objective without worsening at least one other objective. For a given Pareto optimal set, the corresponding objective function values in the objective space are called the Pareto front. Then boundary points of the objective function (Pareto front) correspond to Pareto optimal set. Although the goal in multi objective optimization is to determine the Pareto optimal set, identifying the entire set is impossible in many problems due to its size [70]. Therefore, a practical approach is to find an approximation of the Pareto set (the best-known Pareto set) that represent the true Pareto optimal set as much as possible. To have a good representation of the Pareto set, the following must be considered, as describe in [71]: 1. the Pareto front approximation should be close (maybe subset) to the true one, 2. for a good representation of true Pareto front, the approximate Pareto front result should be diverse over the true Pareto front, 3. the approximation should capture the whole spectrum of the Pareto front.

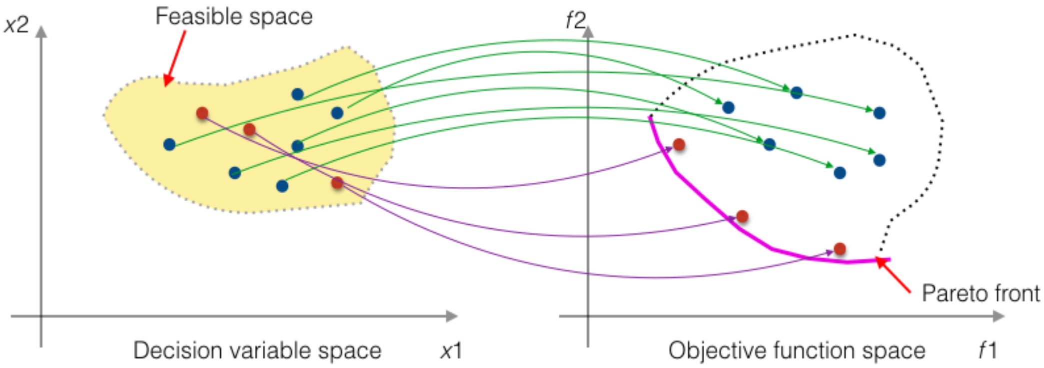

Figure 3.23: Pareto optimal and Pareto front

Algorithms such as Genetic Algorithms (GA) [72] were modified to be able handle to solving multi-objective problems by introducing the notion of non-dominance [73] . Furthermore some of the characteristics of GA (being population based and ability to produce large number of solution at each generation) are good for approximation of Pareto optimal.
The following section describes using the concept of the Pareto optimality to provide the surgeons with optimal surgical approaches.

3.5.1 Method

Similar to the previous section, Figure 3.10, the method in this section has five main parts (patient specific treatment, pathway design, cost function, optimization and Pareto optimal set representation).

Patient Specific Treatment

The input data, initial insertion zone, feasible region and preprocessing steps are similar to previous section. In summary, CT images are used for planning and structures are segmented, the insertion plane is defined by a surgeon, and 3D points inside the feasible region are preprocessed for fast access during the optimization.

Pathway Design

The shape of the pathway is similar to the previous section, an unbalanced biconical shape with same radius of 10 mm and 8 mm. However, the exit location of the pathway was fixed to the center of the target. Therefore the decision variables were the entrance of the surgical pathway and the location of the pivot point (3 DOF).

Cost Function

The ultimate goal is to find an optimal surgical pathway to access the lesion. The same objectives are used here too. Since the exit point of the portal was fixed to the center of the target, the amount of target removal was not considered in this case.

$$min\{f_n(x)\} \quad n = 1, 2, 3 \tag{3.3}$$

$$\begin{cases} f_1 = P \cap S_{bone} & \text{objective 1: amount of bone removal} \\ f_2 = P \cap S_{tissue} & \text{objective 2: amount of tissue removal} \\ f_3 = -dist_{min}(P, S_{critical}) & \text{objective 3: distance to critical structures} \end{cases}$$

s.t.

$$P \cap S3' = \emptyset$$

$$dist_{min}(P, S_{critical}) > d_m$$

$$where \begin{cases} P & \text{pathway} \\ d_m & \text{minimum distance of the closet point of the path to the structures of type 2} \\ S_{3'} & \text{region of deformable structure 3 that must be avoided} \end{cases}$$

Optimization

In order to find the Pareto optimal solution set or its approximation that satisfies the objectives, two methods (genetic algorithm and particle swarm) were studied. The main reason to choose these algorithms for study is their population based nature that allows generating several elements of the Pareto optimal set in each generation [73].

- GA for multi-objective problems The basic idea in the GA algorithm is the current population (current solution) can be used to form the next generation or new population with a goal that the new population will be better than the old one. Solutions which are selected to form new solutions "offspring" are selected according to their fitness - the more suitable they are the more chances they have to reproduce [73]. In our application, "fitness" corresponds to less bone removal, tissue removal and larger distance to the critical structures.

  A generic single-objective GA can be modified to find a set of multiple non-dominated solutions in a single run. The ability of GA to search different regions of a solution space simultaneously, makes it possible to find a diverse set of solutions. As stated before, having a diverse solution that represents the true Pareto optimal well was one the requirements/goals in multi-objective optimization. Several major multi-objective GA methods [70] are described in the literature, that are well-known and have been used in many applications. The Fast Non-dominated Sorting Genetic Algorithm (NSGA-II) was used as optimization method in the surgical planning task.

  NSGA-II [72] is a popular method that was developed for solving non-convex and non-smooth multi-objective optimization problems which has the following features: 1. a non-dominated sorting where all the individual are sorted and classified into different layers, the first layer is the Pareto front, 2. storage of non-dominated solutions (Elitism) and therefore better convergence to the true Pareto optimal set, 3. crowding distance which is ranking among the members of a classified layer, in order to guarantee diversity and spread of solutions, 4. constraints handling by defining the constrained-domination principle.

Based on our cost function (non-smooth, non-convex and constrained), the NSGA-II seems an appropriate method because of its speed, ability to solve these problems and better convergence to the true Pareto optimal. The NSGA-II developed in Matlab optimization toolbox was used for this purpose [74].

The outline of the basic GA and NSGA-II are added to Appendix B.

- Particle Swarm Optimization algorithm (PSO)

  Particle swarm optimization (PSO) is a population based stochastic optimization technique, inspired by social behavior of bird flocking. The basic idea is that local interactions can motivate the group's behavior, and each member of the group can profit from the discoveries and information of other members [75]. Therefore, using this information the population (swarms/particles) can be guided toward the promising area of the search space. Similar to GA, PSO is initialized with a group of random particles (solutions). Each particle remembers the best fitness value it has achieved thus far during the operation of the algorithm, referred to as the individual best fitness. In addition, the PSO algorithm maintains the best fitness value achieved among all particles in the swarm, called the global best fitness. In contrast to GA, when the new generation of population is created, the position of the original particles are updated at each iteration based on the obtained velocity. The velocities of particles are obtained based on their current velocity, current position, personal best and global best positions. The velocities at each iteration guide the particles to optimal solution in the search space. More details about the algorithm can be find in [76], the basic outline of this algorithm is included in appendix B.

  PSO can be extended to solve multi-objective optimization problems by incorporating the Pareto dominance concept. There have been several recent proposals to extend PSO to handle these problems [77]. The method described in [78] was used for approximating the Pareto optimal solution in the surgical pathway planning task. In this

> method, an external repository was incorporated in which the main objective was to keep a historical record of the non-dominated vectors found along the search process, this is similar to the notion of elitism in GA. In addition, the mutation operator was added to improve the explorative behavior of the swarms and ensure that the full range of every decision variable was explored to prevent converging to a false Pareto front. Finally, the constraints were handled in this method.

Since generating the Pareto optimal set can be often infeasible due to the size and complexity of the real world problems, the goal is to try to find a good approximation of the Pareto set. In other words, finding a set of solutions whose objective vectors (Pareto front) are close to the optimal objective vectors. In order to test the Pareto optimal set obtained from GA algorithm, the Pareto front obtained from this method was compared with the results of brute force search and Pareto front obtained from PSO.

The Kung's method [79] was used to find the non-dominated solutions of the exhaustive search of the feasible space (large grid sizes for each variable). Figure, 3.24 shows the Pareto front obtained from the brute force search, GA and PSO algorithms. The Pareto front surfaces obtained from both algorithms were close visually.

Figure 3.25 shows the Pareto front obtained from the GA and PSO algorithms for 3 additional patients. Solutions obtained from both methods were close, however PSO was computationally faster and found more diverse solutions. Increasing the population size and Pareto fraction parameters in the GA method would change the results closer to the solution obtained from PSO.

Pareto Optimal Set Presentation

In this method, surgeons will be presented with a set of optimal approaches that are non-dominated with respect to each other (Pareto optimal set). Therefore from one Pareto solution to another, there is always a certain amount of sacrifice in one objective to achieve a certain amount of gain in the other [70].

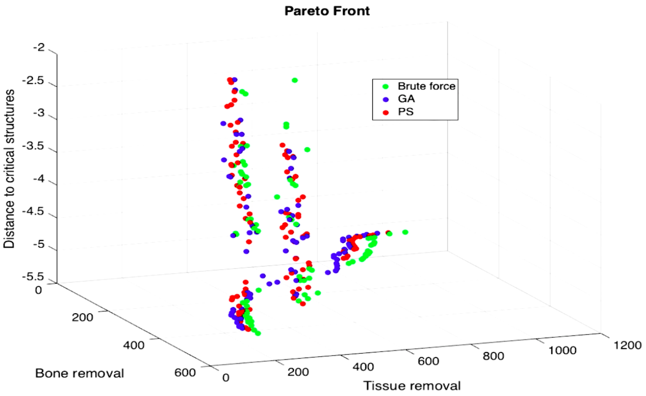

Figure 3.24: Pareto front comparison of GA, PSO and Brute force search for a random selected data set

One method of presenting the Pareto optimal set to surgeons could be sorting the pathways based on each objective (bone removal, tissue removal, and distance to critical structures) and coloring them from low cost (blue) to high cost(red) as illustrated in Figures 3.26, 3.27 and 3.28 (for a randomly selected patient). Surgeons will be selecting *the surgical approach* based on their experiences and patient's health condition.

For this specific patient, the Trans-nasal approaches have a lower cost for objectives such as bone removal and distance to critical structures (blue color) in Figures 3.26 and 3.27. However, if the surgeon is more concerned about the amount of tissue removal, the Trans-orbital approaches will be better (lower cost - blue color in Figure 3.28) compared to the Trans-nasal approaches. Therefore, the optimal approach depends on the surgeon's preferences.

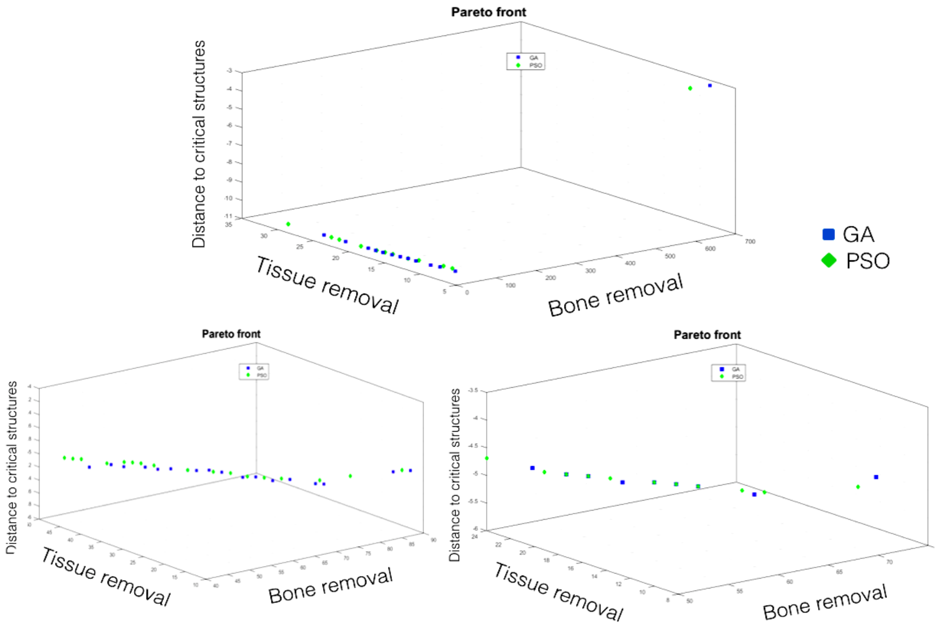

Figure 3.25: Visual Pareto front comparison for 3 different patients - GA and PSO

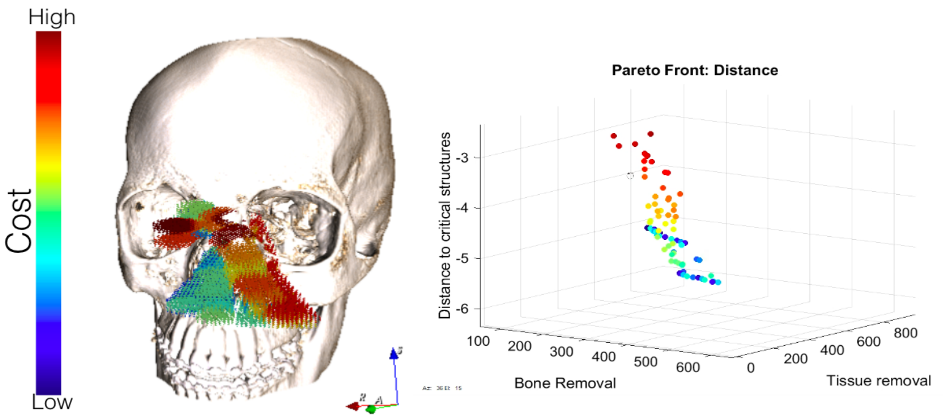

Figure 3.26: Pareto front and Pareto optimal solution - distance to critical structures

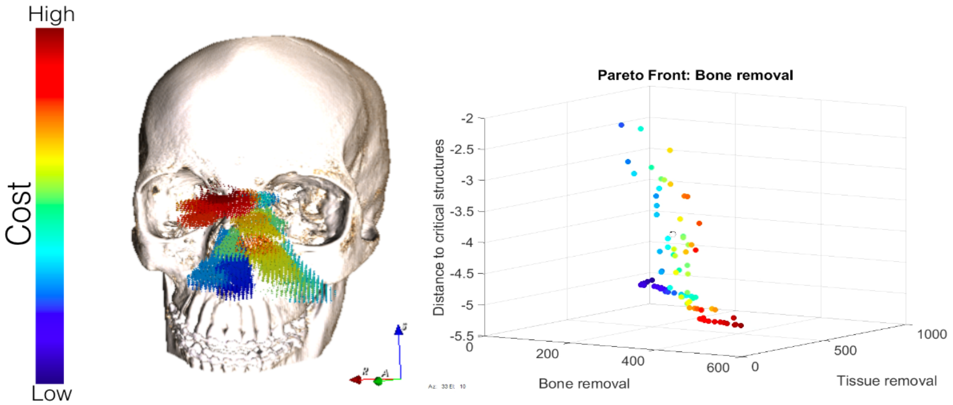

Figure 3.27: Pareto front and Pareto optimal solution - bone removal

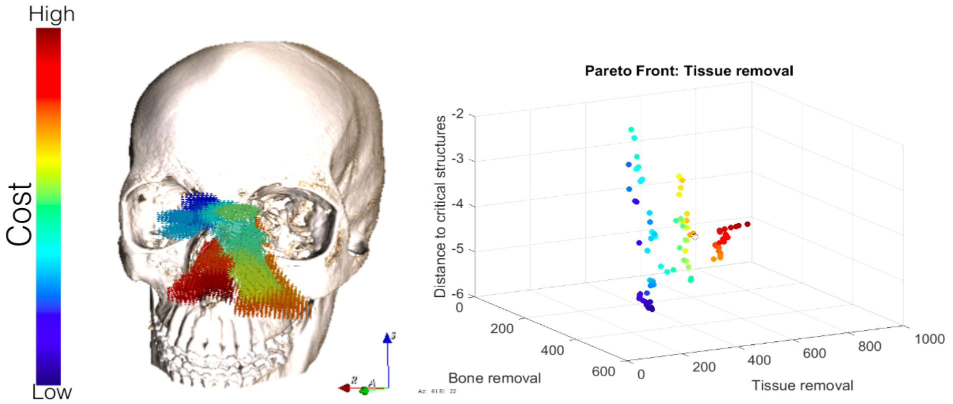

Figure 3.28: Pareto front and Pareto optimal solution - tissue removal

Chapter 4

SURGICAL PATHWAY PLANNING SYSTEM: VALIDATION

4.1 Introduction

The pre-operative planning system described in the previous section assists surgeons 3 different ways: 1. Manual planning; 2. providing an optimal approach based on surgeons' preferences entered as weights; 3. providing a set of optimal pathways from which the surgeon can select the optimal pathway or a set of pathways.

The lack of 3D visualization of patient model (different structures) and the surgical pathway, make the current planning method a time consuming and error-prone process. Surgeons and residents who used the manual planning feature in a prototype Skull Base Pre-operative Planning software [57] evaluated it positively. Surgeon feedback showed that the system improved the planning process, specifically via the ability to rapidly explore different pathways, the ability to visualize inside and outside the pathway, and the ability to manipulate the pathways and change the geometry with minimal interaction.

Different studies described in this chapter were designed to evaluate the following main goals:

- To validate the objectives of the cost function
- To compare the computed optimized pathways with the surgeons' manual pre-operative planning
- To compare the computed optimized pathways with the actual surgical pathway performed on the patient
- To test the dexterity, visibility and accessibility of the target using the optimized computed pathway via a cadaver study

To validate and test the methods in a pre-operative planning system, image data from 7 patients with different tumor locations were used. The *hard to access* regions of the lesions were identified and segmented manually by an expert Otolaryngologist. These were regions that were in proximity to vital structures such as optic or facial nerves. The different regions of the lesion were segmented and used as targets independently while the rest of the lesion were segmented as regular tissue ($S1$ structures).

4.2 Goal 1: To Validate the Objectives of the Cost Function

Five head and neck (skull base) and sinus surgeons participated in this experiment to evaluate if the factors/objectives considered in the cost function are valid in context of skull base surgical planning.The 3D model and 2D views for each pathway were presented to surgeons using 3D slicer software, Figure 4.1.

A questionnaire was designed, and surgeons were asked to assess each pathway on a 5-point Likert scale (Strongly agree to Strongly disagree), Figure 4.2. Surgeons were able to go through slices of each patient (2D and 3D view) to examine the target location and the pathway, Figure 4.1. For each presented pathway, the surgeons were asked to agree or disagree with the following statements:

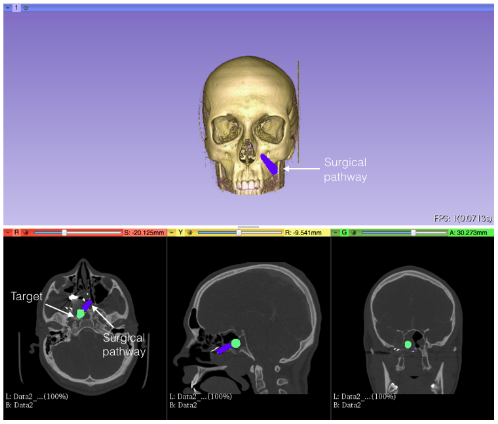

Figure 4.1: Survey 1, the presented surgical pathway to surgeons

1. The amount of bone removal in this path is clinically feasible and does not cause

significant risk.

2. The amount of soft tissue removal/retraction in this path is clinically feasible.
3. Considering the target location, the path is not too close to the critical structures - optic nerve or extraocular muscles.
4. The degree of access for target removal is reasonable with this path.

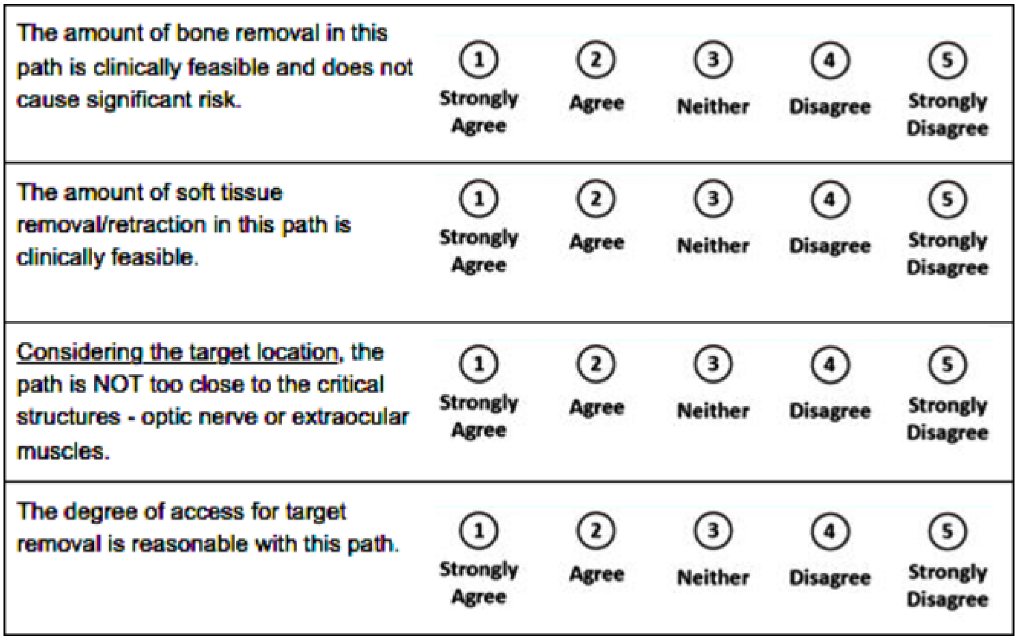

The amount of bone removal in this path is clinically feasible and does not cause significant risk.	① Strongly Agree	② Agree	③ Neither	④ Disagree	⑤ Strongly Disagree
The amount of soft tissue removal/retraction in this path is clinically feasible.	① Strongly Agree	② Agree	③ Neither	④ Disagree	⑤ Strongly Disagree
Considering the target location, the path is NOT too close to the critical structures - optic nerve or extraocular muscles.	① Strongly Agree	② Agree	③ Neither	④ Disagree	⑤ Strongly Disagree
The degree of access for target removal is reasonable with this path.	① Strongly Agree	② Agree	③ Neither	④ Disagree	⑤ Strongly Disagree

Figure 4.2: Survey 1

The presented pathways were generated from 3 patient images with different target locations, for a total of 15 simulated cases. The purpose of generating different pathways (same target location) was that the surgeons could be presented with not only good (low-cost) but bad(high-cost) surgical pathways to rate.

In order to systematically generate pathways with different cost values, the feasible plane was sampled uniformly, Figure 4.3. To make the sampling possible, 4 out of 6 pathway parameters were set to constant values resulting in a 2 dimensional search space. The pathways were ordered from low to high calculated cost, Figure 4.3. Finally, 5 random pathways were selected from the sorted cost values with equal intervals. For each presented case, the average of agreement by surgeons with each statement (1 = strongly agree - 5 = strongly disagree) was plotted against the pathways. Figures 4.4 4.5 and 4.6, blue shows strong agreement and yellow strong disagreement. The surgeons' responses showed that they generally agreed that lower cost pathways were better and more reasonable compared with higher cost pathways in all objectives (tissue removal, distance to critical structures and target removal). Specifically, for pathways 1 and 2 which had the lowest cost values, 90% - 95%, 85% - 90% and 80% - 65% (in patient 1, 2 and 3 respectively) of all the surgeons responses to statements were strongly agree or agree.

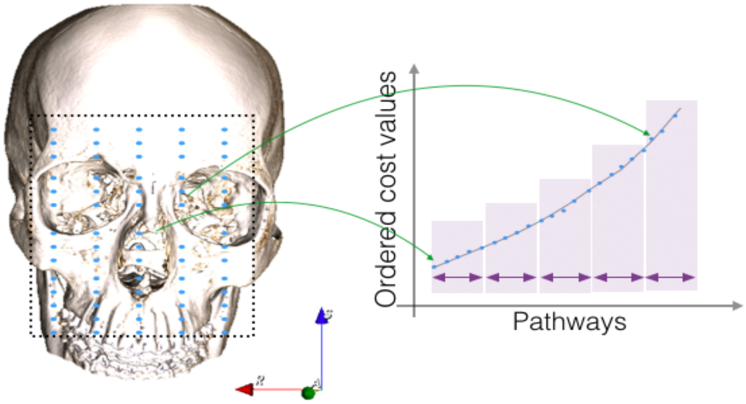

Figure 4.3: Ordered cost values and pathway selection with different cost values

Pathways 1 and 2 (in patient 1 and 2) were Trans-orbital and Trans-nasal approaches and surgeons preferred Trans-nasal pathways over Trans-orbital based on their average score. This is understandable since Trans-orbital approaches are state-of-the-art and more challenging compared with Trans-nasal and require special surgical training. Pathway 5 in patient 3 went through extra-ocular muscles and had a high cost according to the cost function, however the approach did not score low by some of the surgeons since they considered the deformability of this structure.

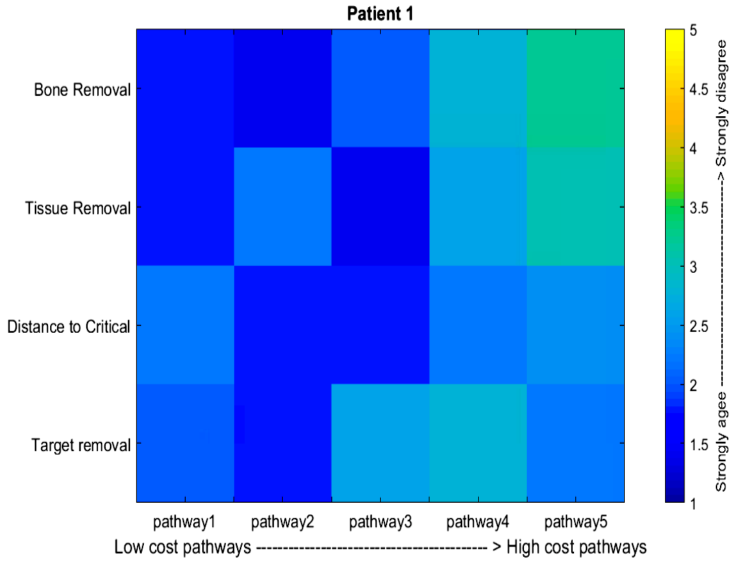

Figure 4.4: Patient 1: 5 generated pathways with different cost values

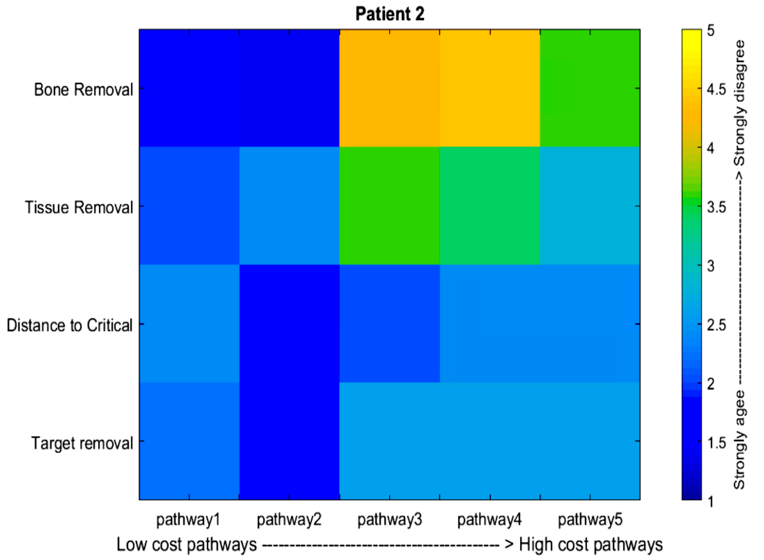

Figure 4.5: Patient 2: 5 generated pathways with different cost values

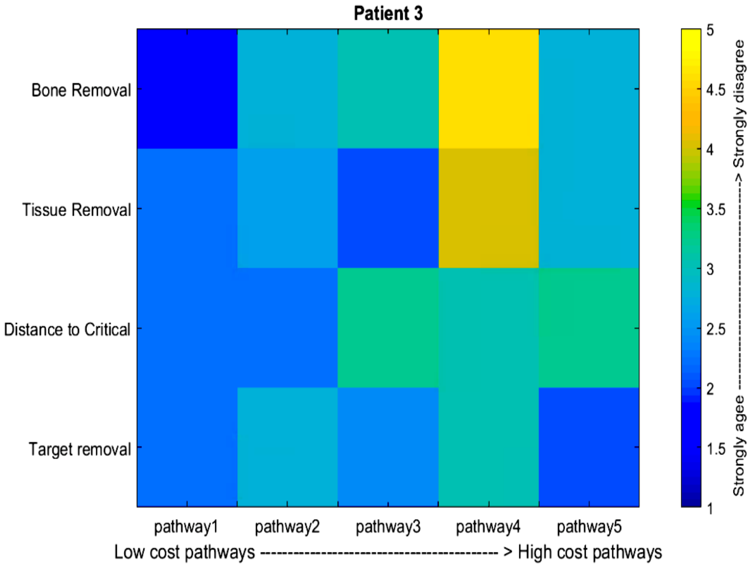

Figure 4.6: Patient 3: 5 generated pathways with different cost values

4.3 Goal 2: To Compare the Computed Optimized Pathways with the Surgeons' Manual Pre-operative Planning

Validation of the generated pathways was studied through the following aims:

- Aim 1: to compare the computed optimized approaches obtained from the weighted sum cost function with the surgeons' manual planning to treat the target

- Aim 2: to compare the computed optimized approaches obtained from the Pareto optimal set with the surgeons' manual planning to treat the target

- Aim 3: to evaluate the quality and feasibility of multiple-pathways planning

Aim 1: To compare the computed optimized approaches obtained from the weighted sum cost function with the surgeons' manual planning to treat the target

The purpose of this survey was to compare the surgeons planned approaches with results obtained from single objective optimization using weighted sum cost function. The weights were assigned based on surgeons explanation in survey 1 with weights decreasing in the following order: bone removal (nasal bone and all other bony structures 0.2), tissue removal (0.2), target removal (0.2), distance to critical structure (0.1) and globe retraction (0.1). Lower weights were assigned to distance to critical structures and globe retraction due to the hard constrains for both these objectives.

To compare the computed optimized pathways with the surgeons preferred approaches, surgeons were given the segmented target locations in de-identified patient pre-operative CT scans (10 cases) and were asked to plan the treatment by selecting their top three approaches from a set of possible pathways described in the literature, Figure 4.7. The approaches were:

- Trans-nasal
- Trans-oral
- Trans-orbital (Superior, Inferior, lateral and medial)
- Trans-maxillary (Caldwell -Luc, inferotemporal)
- Frontal craniotomy
- Preryonal craniotomy (lateral craniotomy)
- Open infratemporal fossa (Fisch type C, D)
- Lefort I
- Supraorbital mini-craniotomy (Perneczkv)

- Trans-frontal bone (Osteoplastic flap, coronal incision)

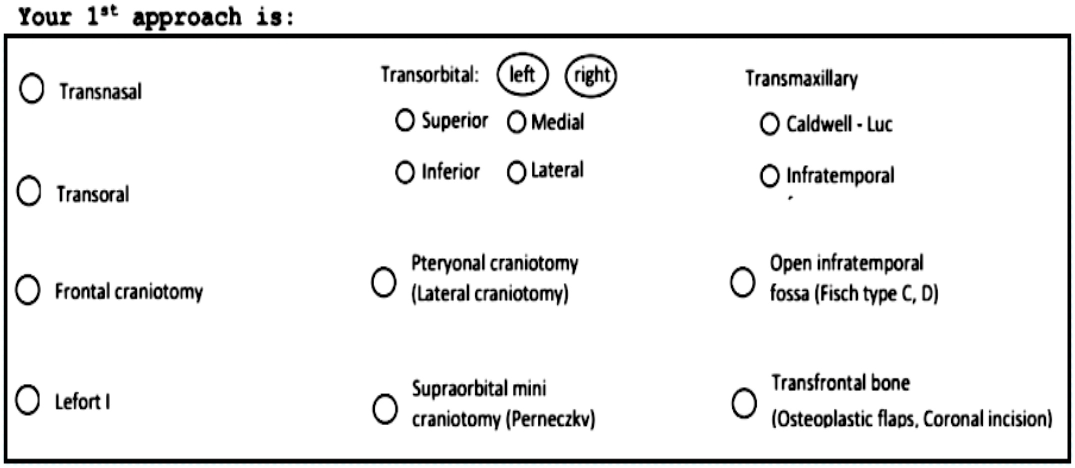

Your 1st approach is:

○ Transnasal	Transorbital: left right ○ Superior ○ Medial	Transmaxillary ○ Caldwell - Luc
○ Transoral	○ Inferior ○ Lateral	○ Infratemporal
○ Frontal craniotomy	○ Pteryonal craniotomy (Lateral craniotomy)	○ Open infratemporal fossa (Fisch type C, D)
○ Lefort I	○ Supraorbital mini craniotomy (Perneczkv)	○ Transfrontal bone (Osteoplastic flaps, Coronal incision)

Figure 4.7: Survey 2

For each of the 10 patients, 3 plans were proposed by 4 individual surgeons (120 surgical pathways). Figure, 4.8 shows the surgeons selected approaches which were similar to the computed optimized pathways for each patient (total of 40 surgical pathways).

For instance, for patient 4, the computed optimal approach was Trans-nasal. The first choice of all surgeons was matched with the optimal approach. In addition, the frequency of surgeons first, second, third and none choices can be plotted. Figure 4.8 shows that 36/40 of computed optimized surgical approaches obtained from the weighted sum cost function were among one of the three plans proposed by the surgeons. Only in *four* patients, *one* of the surgeons surgical approach did not match with the computed optimized approach. However, for these patients, the suggested surgical approach by the other three surgeons was similar to the computed optimized approaches, Figure 4.9. In patient 2, the obtained optimized approach was right, superior, Trans-orbital approach while surgeon 4's choice was right, medial, Trans-orbital but both approaches had almost the same cost values.

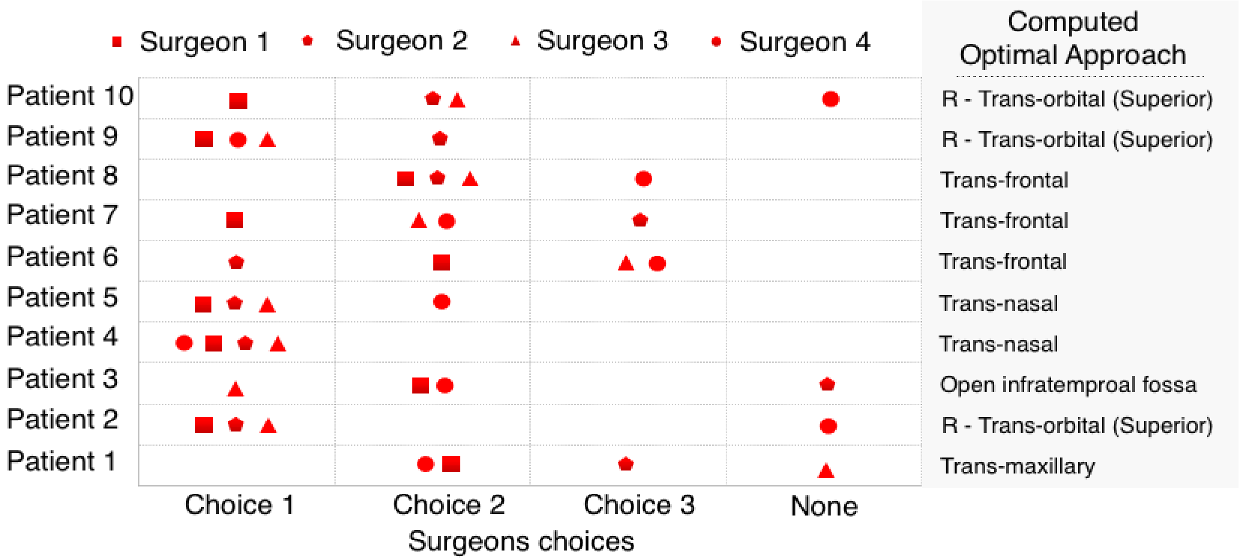

Figure 4.8: Surgeons ranking of approaches compared to the computed optimal approach. A symbol is placed where each surgeon ranked the computed optimal in their personal ranking.

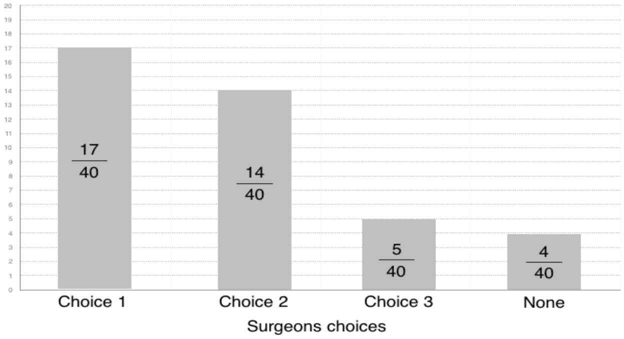

Figure 4.9: Frequency of ranking position for the computed approach. Fraction indicates the number of rankings out of total number of surgeons approaches (40 = 10 patients × 4 surgeons)

Aim 2: To compare the computed optimized approaches obtained from the Pareto optimal set with the surgeons' manual planning to treat the target

The purpose of this survey was to compare the surgeons planned approaches with pathways obtained from multi objective optimization (Pareto optimality concept). Therefore, the computed optimized pathways (Pareto optimal set) from the GA algorithm (100 pathways) were categorized based on the different approaches in survey 2, Figure 4.7. Figure 4.10 illustrates the Pareto optimal pathways and the main 4 different categories of surgical approaches (Trans-nasal, right and left Trans-orbital and Trans-maxillary) for one patient.

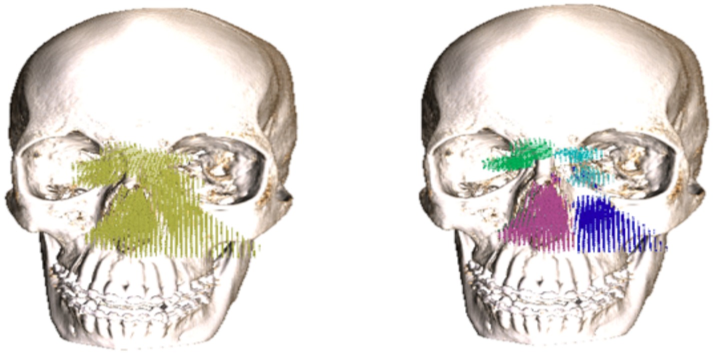

Figure 4.10: Optimal surgical pathways from the GA

For 10 patients, the obtained categories were compared with surgeons top three manual approaches planned/ranked from the survey 2. Figure 4.11 shows the Pareto optimal set compared with surgeon's first ranked plan. For instance, for patient 1, the Pareto optimal set categories were: Trans-nasal, Lefort I, Left Trans-orbital (Medial), Right Trans-orbital (Medial) and Trans-maxillary (inferotemporal). The first choice of all surgeons was Trans-nasal and therefore all the 1st approaches (choices) were on the Pareto front. Figures 4.12 and 4.13 show the Pareto optimal set compared with surgeons' second and third ranked plans. Again, for patient 1, surgeons (2 and 3) second ranked approaches and surgeons (1, 2, and 4) third choices were matched with the categories of the Pareto optimal set.

The results showed that [70%, 52%, and 45%] of surgeons' first, second and third suggested approaches were in the Pareto optimal set respectively. Future work will analyze the surgical pathways that were in the Pareto optimal set but not proposed by surgeons.

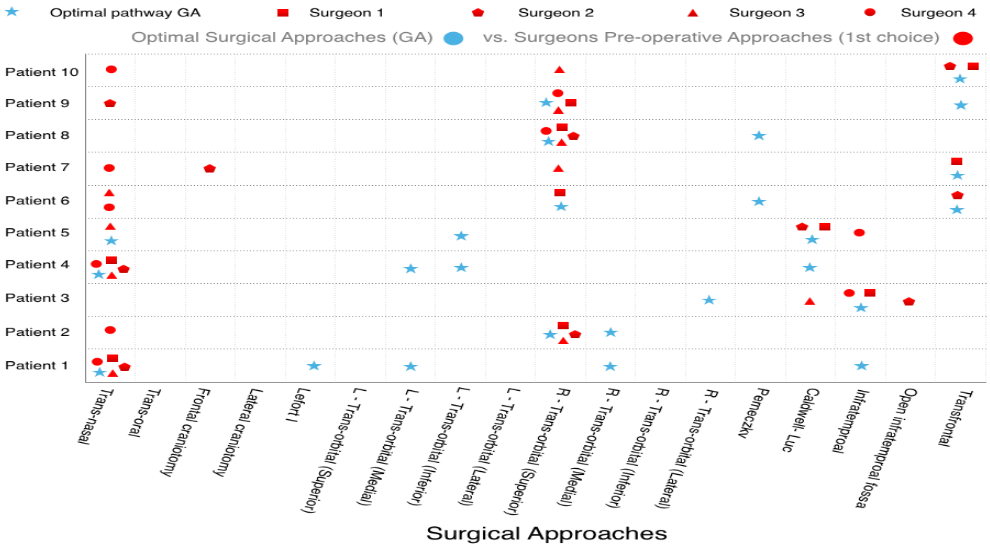

Figure 4.11: Pareto optimal surgical pathways vs. surgeons 1st plan for each patient

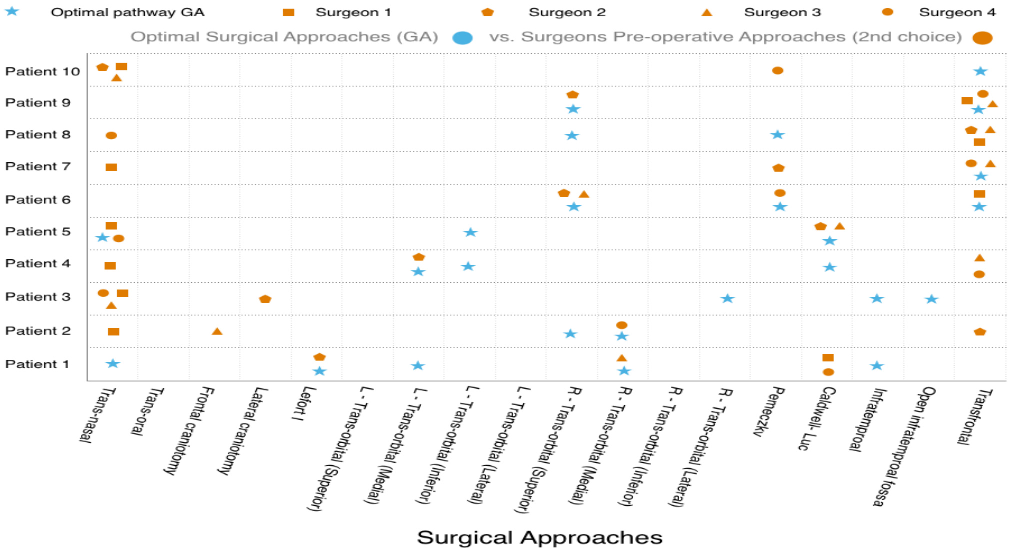

Figure 4.12: Pareto optimal surgical pathways vs. surgeons 2nd plan for each patient

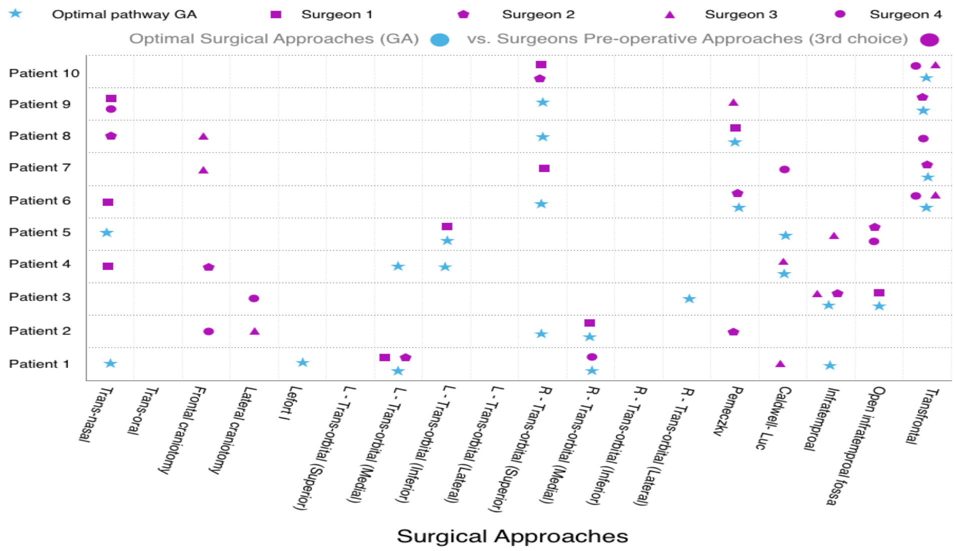

Figure 4.13: Pareto optimal surgical pathways vs. surgeons 3rd plan for each patient

Aim 3: To evaluate the quality and feasibility of multiple-pathways planning

The purpose of this study was to evaluate the quality and feasibility of multiple pathways planning using the weighted cost function, method described in section 3.3. The reason for planning two pathways simultaneously is the cases which require two surgical pathways to fully access and observe the target removal, for example, two surgical pathways for Endoscope and Microdebrider. In these cases, using the single pathway cost function to plan a pair of pathways will result in spatially similar pathways due to process of minimizing the cost function. The goal of this section was to evaluate the pathways obtained from equation 3.2 with subjective ratings of the surgeons. Three skull base surgeons were presented with target location, the optimized multiple pathways, and metrics presented in table 4.1. As described in previous chapter (Cost function definition) and Figure 3.20: 1. Target removal refers to the number of voxels inside the pathways (Maximizing); 2. Angle between the pathways refers to the angle between the center lines of two pathways (Hard constraints); 3. Bone removal refers to the number of bone voxels inside the both pathways (Minimizing); 4.

Tissue removal refers to number of tissue removal inside the both pathways (Minimizing); 5. Distance to critical structures refers to minimum Euclidean distance of the pathways to optic nerves and extra ocular muscles (Maximizing).

For 5 patient data, considering the target locations, the planned pathways were all clinically valid and feasible to access and remove the pathology.

One of the surgical pathways obtained for patients 4 and 5 were not a standard/common approaches to treat the specified target, as shown in Figures 4.14 and 4.15. For these cases, the obtained optimal approaches were compared with the surgeon's preferred surgical pathways, Figures 4.16, 4.17 and 4.18. The surgical entry was found by the Brute force search of the region suggested by the surgeon for each case. Specifically, Trans-nasal for case 4 and Trans-orbital (right) for case 5. The metrics confirmed a better fitness for the computed optimized surgical pathways against the manual ones, Table 4.2. Specifically, the number of bone and tissue voxels removals were both higher for patient 4 (computed optimized vs. surgeons preferred pathways). Similarly, for patient 5, the tissue and bone removals were higher even by relaxing the hard constraints (distance to critical structures to 1 mm).

The homogenous weight assignments to different bony structures could be one reason for this result. For instance, if the "not common" surgical pathway in case 4 was a few millimeter inferior to the optimized position, the new pathway would be more preferable by the surgeon, even though the amount of bone removal will be more. In chapter 5, the initial steps toward this goal will be described. However, additional studies must be designed to fully examine the feasibility of these *new* surgical pathways.

Table 4.1: Subjective rating of three surgeons for multiple-pathway planning

Data	Approaches	Target removal (voxels)	Angle between pathways (degrees)	Bone removal (voxels)	Tissue removal (voxels)	Distance to optic nerves (mm)	Distance to extraocular muscles (mm)	Surgeons rating
Case 1	Trans-nasal Trans-nasal	945	89.2	0	208	21.4	15.2	Clinically valid
Case 2	Trans-nasal Trans-nasal	1138	42.2	1	300	16.9	12.6	Clinically valid
Case 3	Trans-orbital Trans-orbital	1042	61.75	0	133	8.3	3.0	Clinically valid
Case 4	Trans-orbital Trans-maxillary	1753	25.27	207	681	11.70	3	Clinically valid
Case 5	Trans-orbital Trans-nasal	1672	36.04	91	619	5	4.5	Clinically valid

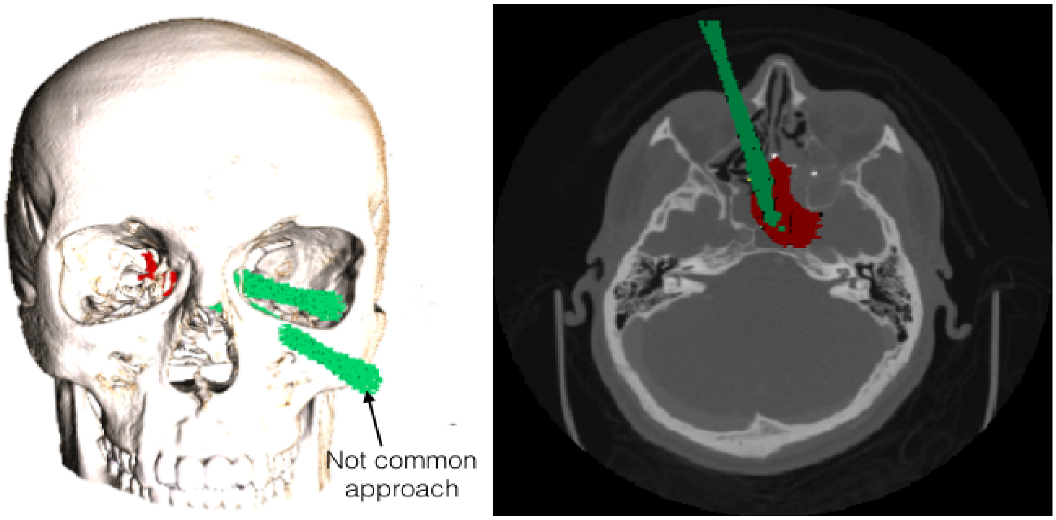

Figure 4.14: Multiple-surgical pathways (Case 4) with a representative axial slice and target location

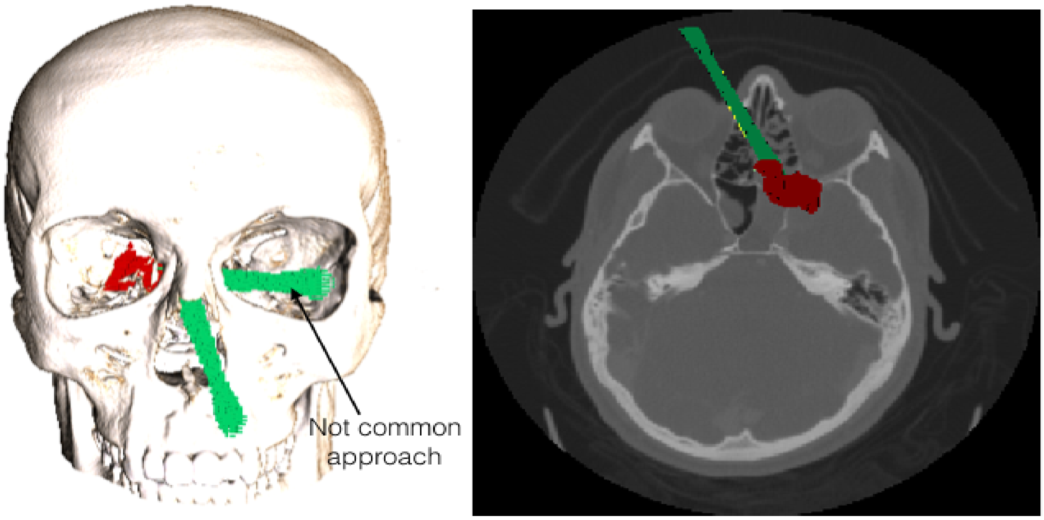

Figure 4.15: Multiple-surgical pathways (Case 5) with a representative axial slice and target location

Table 4.2: Case 4 and 5 comparison with manual planning

Data	Approaches	Target removal (voxels)	Angle between pathways (degrees)	Bone removal (voxels)	Tissue removal (voxels)	Distance to optic nerves (mm)	Distance to extraocular muscles (mm)
Case 4	Trans-orbital Trans-maxillary	1753	25.27	207	681	11.70	3
Case 4 (Manual)	Trans-orbital Trans-nasal	1811	20.53	436	736	12.24	3
Case 5	Trans-orbital (left) Trans-nasal	1672	36.04	91	619	5	4.5
Case 5 (Manual)	Trans-orbital (right) Trans-nasal	1338	49.04	182	648	11.18	2.23
Case 5 (Manual 2)	Trans-orbital (right) Trans-nasal	1379	42.34	110	386	11.22	1

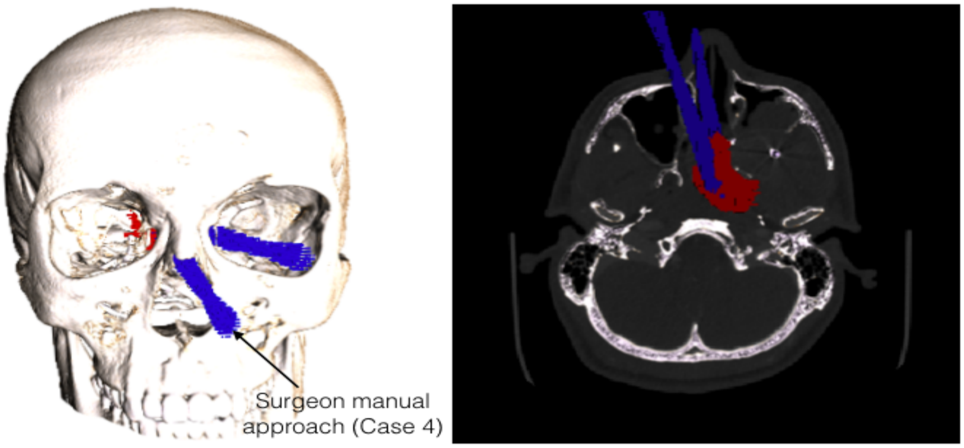

Figure 4.16: Multiple-surgical pathways (Case 4) manual planning

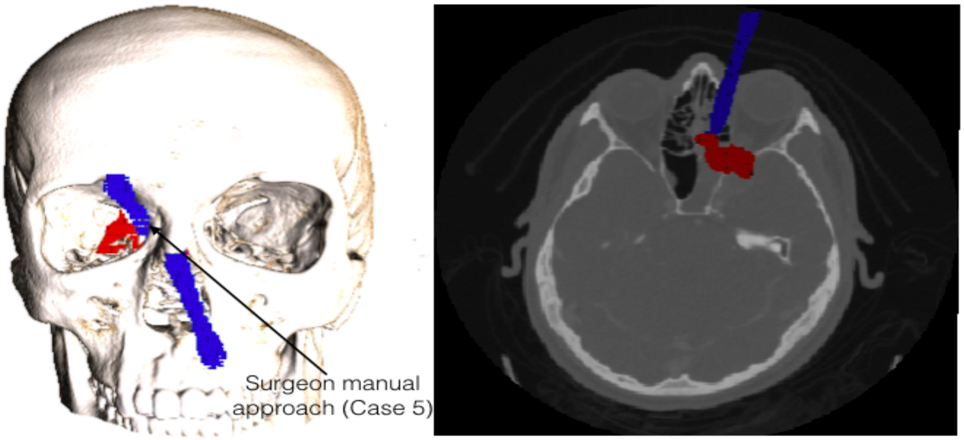

Figure 4.17: Multiple-surgical pathways (Case 5) manual planning 1

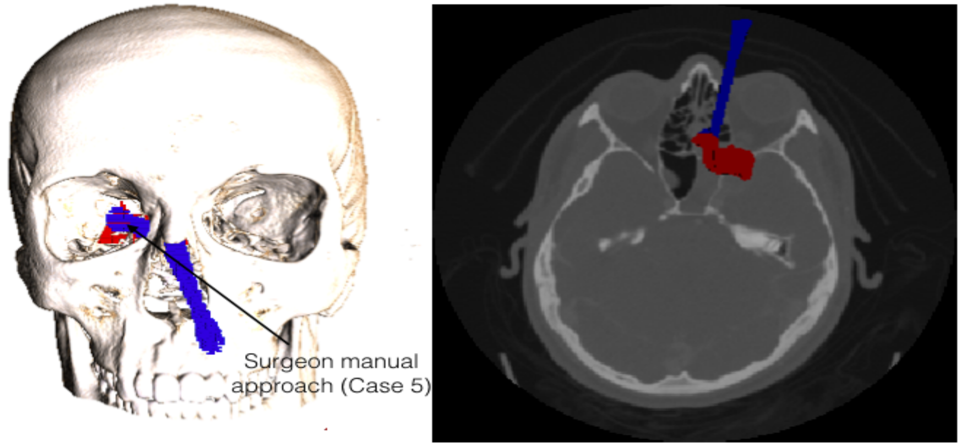

Figure 4.18: Multiple-surgical pathways (Case 5) manual planning 2

4.4 Goal 3: To Compare the Computed Optimized Pathways with the Actual Surgical Pathway Performed on the Patient

In this study, the computed optimized pathways were compared with the actual surgical pathways performed on the patient in the Operating Room (OR) using the patients' post-operative image and information. The 7 patient cases analyzed in this work were classified as challenging cases which preferably should be treated in advanced centers.

As described in the previous chapter, in this study the patient data had tumors in late stages, which must be removed. For planning, the target was segmented based on *hard to access* regions and the rest of the lesion was treated as normal tissue. The reason for considering only a part of target for planning was because surgeons plan their approaches based on the regions that are hard to access. The easy to access region requires little or no incision. Therefore, If a patient had two hard to access regions, at least one of the computed optimized pathways must be similar to the actual performed approaches.The actual approaches and the post-operative complications were obtained from the surgeons who performed the surgery by either using the post-operative image or from the patient file.

Table 4.19 summarizes the post-operative approaches and the pre-operative planning obtained from the weighted-sum optimization method and categorizes of the Pareto optimal set (obtained from aim 2 of goal 2). Except for case 6, all of the actual surgical approaches were similar to optimized approaches. For patient 6, the computed optimized approaches were Trans-frontal (in weighted-sum and Pareto optimal set methods) and (Pareto optimal set method). In addition changing the weights did not change the optimized approach in the weighted-sum method. However, the surgeon's first approach was Trans-nasal and due to the post-operative complication (CSF leak), in the second operation the Trans-orbital approach was used to repair. The surgical pathway obtained for patient 6 (Trans-frontal) is reasonable because the large amount of frontal bone erosion (due to tumor) and the tumor location itself (far from the critical structures), figure 4.19. Therefore, the cost consisted of removing small amount of tissue (skin) removal and frontal bone removal (eroded) and larger amount of target removal and distance to critical structures.

Table 4.3: Optimal surgical approach vs. post-operative approach

	Weighted sum optimal pathway	Pareto optimal pathways (categories)	Actual surgical pathway	Complications
Patient 1	Trans-nasal (hard 2) Trans-orbital (hard 1)	Trans-orbital	Trans-nasal Trans-orbital Trans-maxillary	No complication Complete removal of tumor
Patient 2	Trans-orbital (hard 1) Trans-maxillary (hard 2)	Trans-nasal Trans-orbital Trans-maxillary	Trans-nasal Trans-maxillary	No complication Complete removal of tumor
Patient 3	Trans-orbital (hard 1)	Trans-orbital	Trans-orbital	No complication Complete tumor removal
Patient 4	Trans-maxillary (hard 1)	Trans-orbital Trans-frontal Trans-maxillary	Trans-nasal Trans-maxillary	No complication Complete tumor removal
Patient 5	Trans-nasal (hard 1, 2)	Trans-nasal Trans-orbital Trans-maxillary	Trans-nasal Trans-maxillary	No complication Complete tumor removal
Patient 6	Trans-frontal (hard 1, 2, 3)	Trans-orbital Trans-frontal	Trans-nasal Trans-orbital	CSF leak Repaird with subsequent Trans-orbital approach
Patient 7	Trans-orbital (hard 1) Trans-frontal (hard 2, 3)	Trans-orbital Trans-frontal	Trans-nasal Trans-orbital	No complication Complete tumor removal

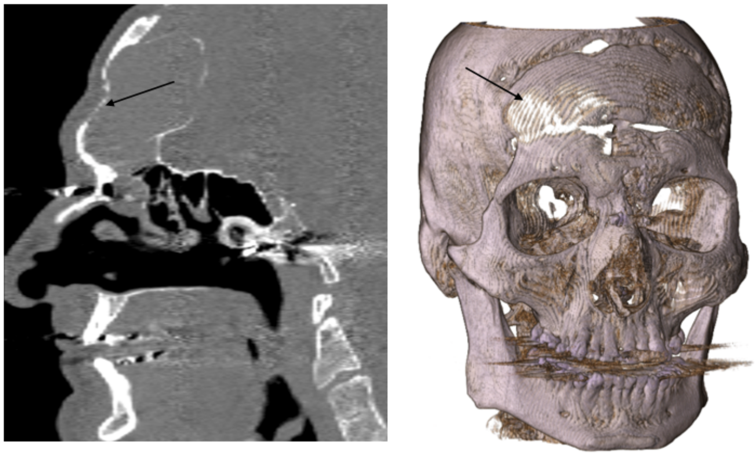

Figure 4.19: Frontal bone erosion in patient 6: Sagittal view of representative slice and 3D bone window of pre-operative CT

4.5 Goal 4: To Test the Dexterity, Visibility and Accessibility of the Target Using the Optimized Computed Pathway Via a Cadaver Study

The pupose of this experiment was to confirm the surgical feasibility of the pathway found by single weighted sum cost function by testing the ability to accurately carry out the plan and to compare its shape to what was actually performed.

A cadaver head CT scanned at Harbor View Medical Center was used for the planning. Two different locations in the skull base were labeled as targets by an expert skull base surgeon. Both target locations were considered as medium to challenging tumor locations for skull base surgery cases. The planning method with one surgeon's preferences (weights: Bone removal (nasal bone and all other bony structures 0.2), Tissue removal (0.2), Target removal (0.2), Distance to critical structure (0.1) and Globe retraction (0.1)) was used to find the optimal approach for each target location. The operation to access to those locations was performed on the cadaver head by a different surgeon using the proposed pathways outputted from the optimization.

We modified the CT so that the optimal pathway could be visualized during the procedure. The navigation system (Stryker iNtellect Cranial Navigation) was used to track the instrument tip's 3D position and the points obtained from the tracking system were compared with the computer-generated optimal pathways. The 3D surgical pathway and the motion data for both target location are shown in Figures 4.21 and 4.22. For each target location about 64% and 67% of the 3D points (instruments tip position) were inside the optimal pathway, Figures 4.24 and 4.23. For the first target location (the Trans-nasal approach), instruments tip position outside of the surgical pathways were intersecting with bone, tissue or air (11%,9% and 16%) respectively. For the second approach instruments tip position outside of the surgical pathways were intersecting with bone, tissue or air (11%,15% and 7%) respectively. The main reason for the points (instrument's tip position) outside of the pathways was the visual presentation of the pathways on the Navigation screen. Since the surgeons mainly use the endoscopic screen/window to perform the surgery and use the nav-

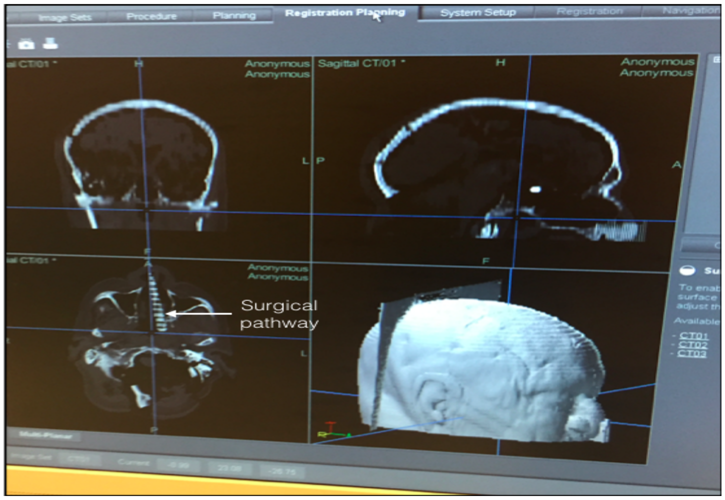

Figure 4.20: Cadaver CT with surgical pathway loaded on Stryker iNtellect Cranial Navigation

igation to only confirm their position (if needed). The points outside the pathways were not disturbing any critical structures, nerves.

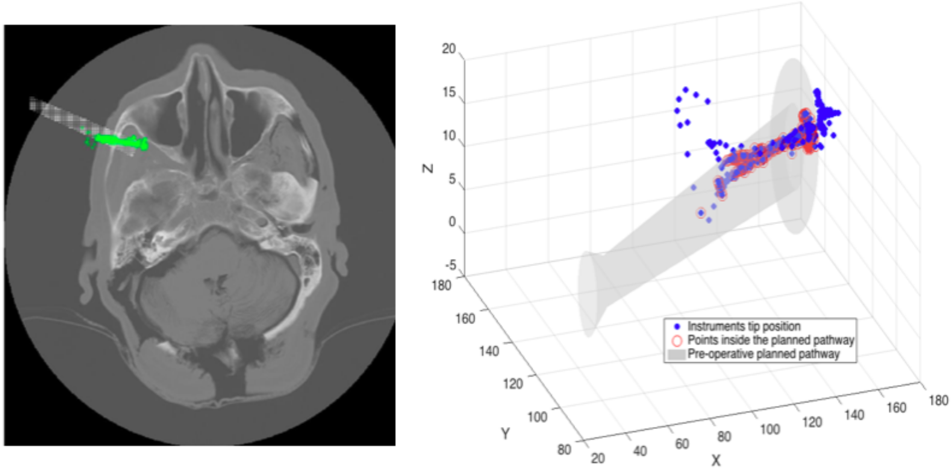

Figure 4.21: Projection of all motion data on a representative CT slice and 3D surgical pathway with motion data for target 1

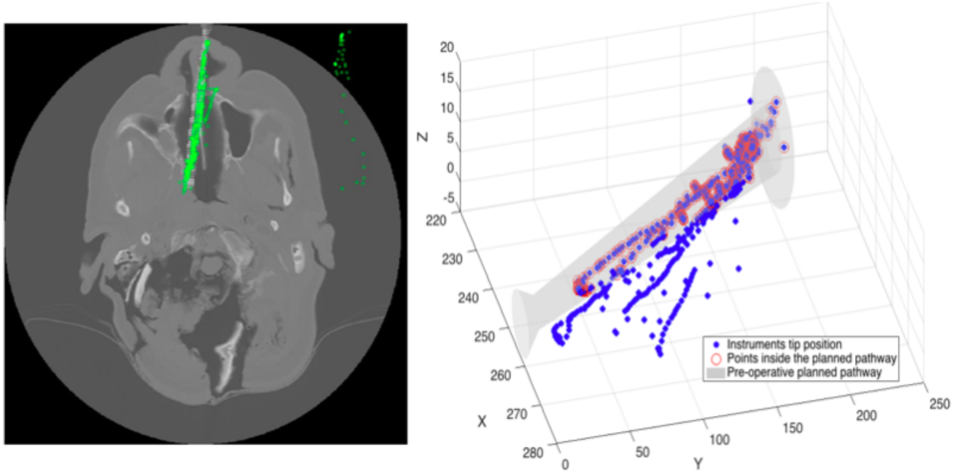

Figure 4.22: Projection of all motion data on a representative CT slice and 3D surgical pathway with motion data for target 2

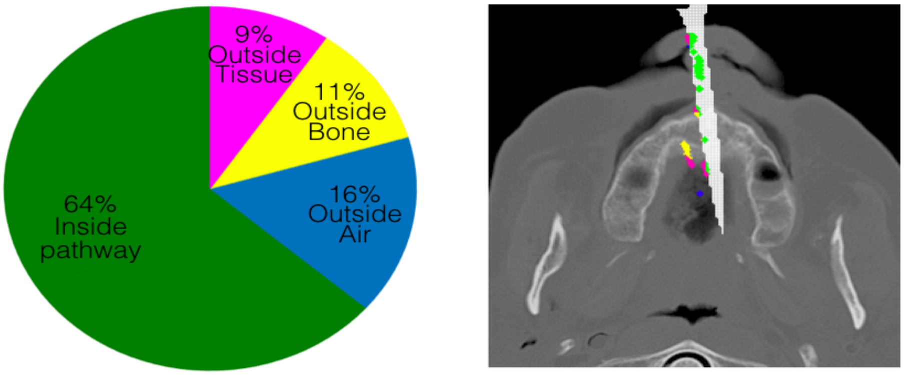

Figure 4.23: Motion data inside and outside the optimized surgical pathway for target 1

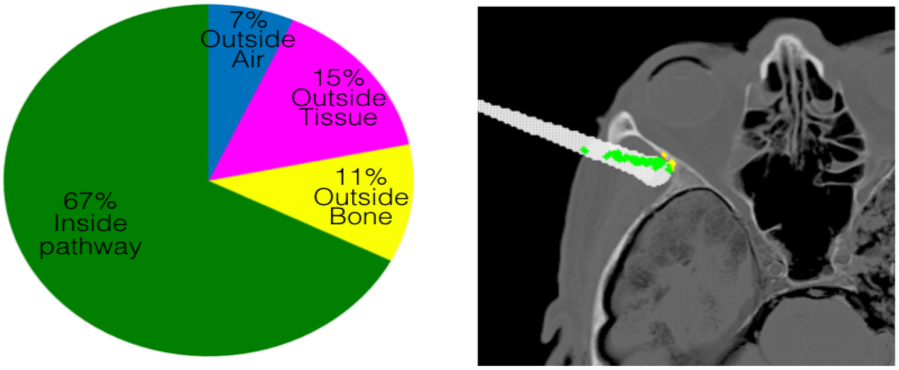

Figure 4.24: Motion data inside and outside the optimized surgical pathway for target 2

The result from this section showed that the optimal pathway was feasible to access and treat the target. It also showed that in addition to visual presentation of the pathway, other warning methods were required to make sure that the instruments were inside the pathway. Therefore to be able to use the surgical pathway without distracting the surgeons, other methods such as haptic feedback or audible alarms are required to ensure that the instruments are moving inside the pathway. Future work will study and compare different methods to use the surgical pathways during the operation without distracting the surgeons.

Chapter 5

ATLAS-BASED SURGICAL PATHWAY PLANNING

5.1 Introduction

In the context of image-processing and analysis, an atlas consists of two parts: an intensity image (template) and its segmented image (the atlas labels). After registering the atlas template and a target image, the atlas labels are propagated to the target image. This process is known as *atlas-based segmentation* and unlike manual segmentation methods, which require a trained technician to manually label regions of interest in target images, these methods require a small or no human assistance [80].

Atlas-based segmentation of medical images has become a standard method for exploiting prior anatomical knowledge in image segmentation [81]. Accordingly, prior anatomical knowledge can be added to an atlas for use in surgical pathway planning. For pathway planning, in addition to structure labels, other anatomical information such as density or elasticity about each structure can be propagated to the target image and be used in planning.

The Visible Human Project [82] or Voxel-Man [83] are two examples of major efforts to create an anatomic atlases. While these projects provided a powerful reference tool for different users in medical disciplines, the dataset do not contain the intensity image (template) and therefore can not be used in methods such as registration. Furthermore, each voxel contains only data about the anatomy and tissue type.

The hypothesis that motivated this study was that an anatomical semantic atlas that contains clinically significant information for every voxel within the CT can be adapted to individual patient images so that the embedded prior knowledge can be used during the planning and optimization. The obtained pathways will be effective and/or safer because they will be computed by exploiting more information.

Atlas-based registration is applied *before* the optimization process (described in previous chapters), in order to transfer information to patient data that can be used in planning. With new information provieded by the atlas, the cost function must be modified. In this section, the atlas construction and registration to patient data method is described and tested. However, utilizing the information in pre-operative planning is the subject of future work.

5.2 Method

The first question in atlas-base segmentation is how to create an atlas. Various techniques for atlas construction have been developed for different human organs, such as brain, heart or head and neck [84],[85],[86].

The proposed skull base atlas was developed from a publicly available CT scan known as the Manix data set [87]. The head and neck segmented labels of the Manix data set is available on the Internet. In this data set, the entire skull and skull base was labeled as one segment as shown in Figure 5.1.

In this work, the skull base region of the Manix data set was manually segmented into 23 bony structures. The orbital structures (optic nerves, extra-ocular muscles and globes) were segmented using the method of chapter 2. Other critical structures and soft tissues were segmented manually or semi-manually.

Each voxel was assigned a value for the following data fields:

1. Anatomical location; 2. Tissue type; 3. Distance of tolerable displacement; 4. Voxel morbidity cost; 5. Tissue material property estimations relevant to surgery.

5.2.1 Description of each field

- Anatomical location: Information about the position of each structure for example different location of sinuses.

- Tissue type: General information about the tissue (hard or soft tissue) and details such as epithelial, connective, muscle, and nervous tissue.

- Distance of tolerable displacement: Maximum amount of displacement without causing any damage to the structure, for example maximum of 10 mm displacement for globes.

- Voxel Morbidity Cost (VMC): Each voxel in the atlas will be assigned with a cost: the morbidity cost is proportional to estimated consequences and severity of the damage to the corresponding tissue.

- Tissue material property:
    - Density: The average density value for different structures is assigned to each voxels.
    - Bulk modulus: The ratio of pressure to volumetric compression.
    - Elasticity: Ability of a body to resist a distorting influence or stress and to return to its original size and shape when the stress is removed.

The segmented structures and the number of data fields is not limited and can be extended with new structures or information such as the relative value score as a function of clinical application. For example, in orbital surgery where it is expected to retract the extraocular muscles, the relative value of extraocular muscles will be weighted much differently than for sinus surgery.

In the future, the atlas will become available for other institution / research groups to use or modify the fields.

5.3 Experimental results

The atlas-based segmentation process is normally composed of three steps: a registration step where the target image is aligned to the single atlas or multiple atlases, a label propagation or fusion step where the labels are transferred from the atlases to the target, and a final

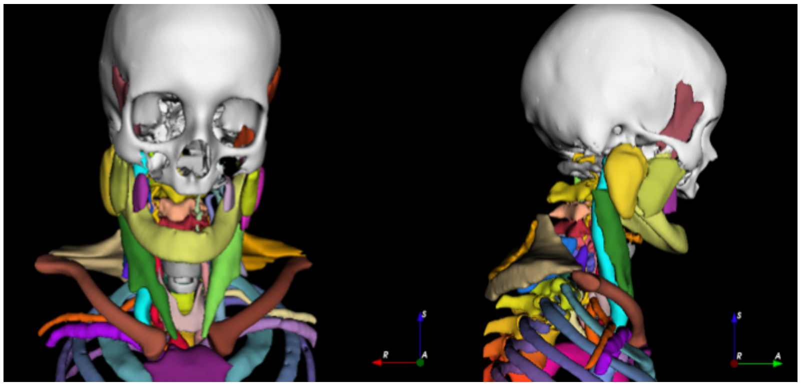

Figure 5.1: Manix data set, head and neck atlas

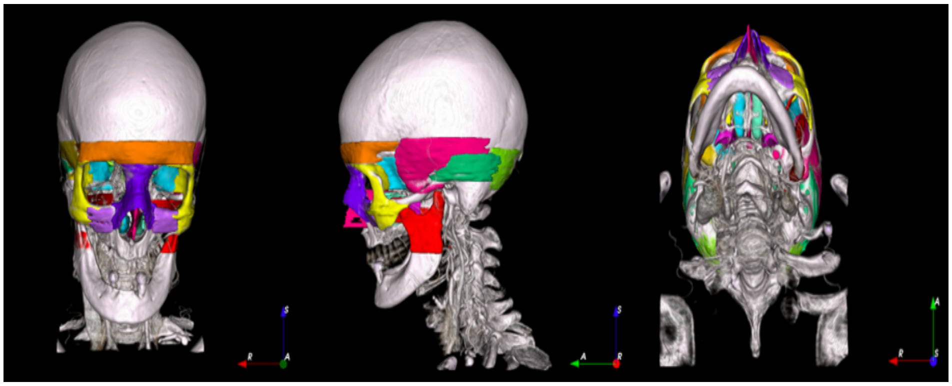

Figure 5.2: Manix data set, skull base atlas

segmentation step in which transferred labels are used to segment the target image. In order to use the atlas in surgical planning, the atlas-based scheme was used to accurately transfer the labeled voxels onto individual patient scans.

The registration process is usually carried out in two separate steps: a global registration (affine or rigid transformation) performed to obtain an initial alignment, followed by a local non-rigid registration to take into account target specific deformations.

Plastimatch software [88] was used to perform a multi-resolution global and deformable registration. Figure 5.3 shows the 3D visualization of the Manix data compared with one patient data. First the affine transformation (12 parameters or DOF) was used to align two

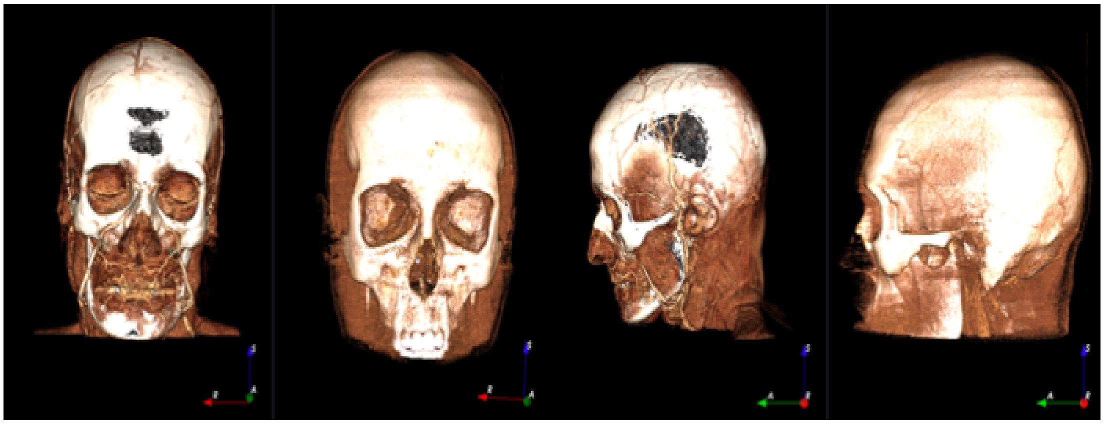

Figure 5.3: 3D visualization to Manix data set and patient data set

volumes. A 3D affine transformation $T : R^3 \to R^3$ is given by $T(x) = Hx + t$ where H is a 3×3 matrix representing the rotation, scaling and shearing, and t is a 3×1 vector representing the translation or shift.

Two kinds of curved deformations have been used in medical image registration: free-form transformations and guided deformations [89]. In many free-form deformation models such as popular method of B-splines, a grid of control points is defined in order to determine the deformation involved. The points of grid are free to move in each direction to optimize the cost function (similarity measure). Since the images are in same modality, the sum of squared difference (SSD) of intensities can be used as similarity measure for both global and local registration.

The Figure 5.4 show a representative slice of the atlas and the patient data before and after affine transformation and deformable registration. After registration, the labels and data fields were transformed and were propagated onto patient data. Since the ground truth segmentation of the patient data was not available, the common metrics such as Dice Similarity Coefficients was not performed for verifying the results. The accuracy of the registration was confirmed by an expert surgeon with slice by slice visualization of the data and the fact that the similarity measure (SSD) was decreased after the registration compared to before. The work proposed in this chapter is an initial step toward using prior anatomical

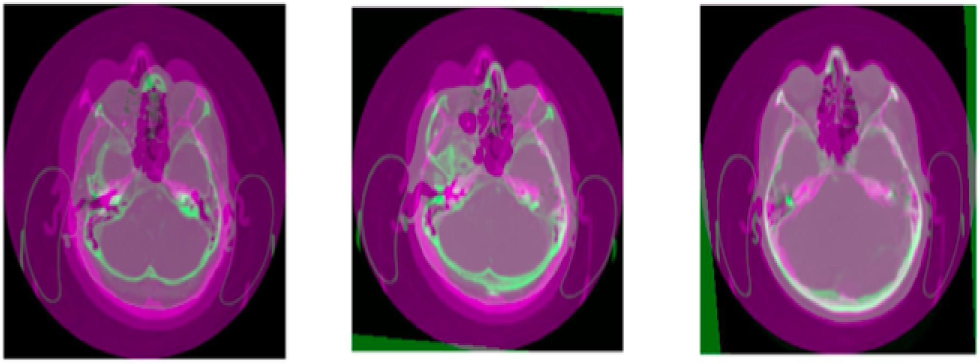

Initial overlaid

Affine

Deformable

Figure 5.4: A representative slice of atlas and patient data overlaid, after affine registration and deformable registration

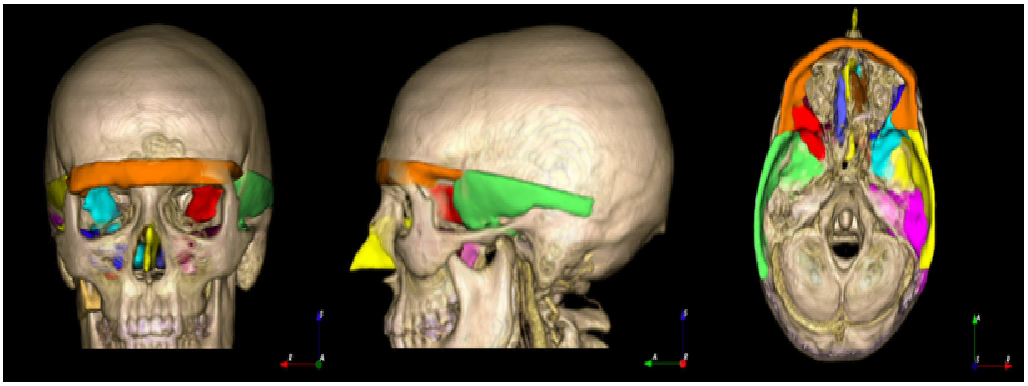

Figure 5.5: 3D model of the patient data with propagated labels

knowledge in the surgical pathway planning. To better capture the variability of target images, multi atlas based segmentation have been proposed which has been shown to be more robust and accurate. Future work consists of constructing multiple atlases, testing the registration accuracy systematically and using the atlas in the pre-operative planning method.

Chapter 6

DISCUSSION AND OPEN QUESTIONS

The previous chapters demonstrated a method of for segmentation of critical orbital structures in the skull base, a method for pre-operative pathway planning for skull base surgery, and construction of an atlas with clinical information that can be used in the surgical pathway planning. This chapter presents ideas on improving the performance of the proposed methods as well as future work.

6.1 Segmentation Based on Anatomical Landmarks

The proposed segmentation method used anatomical knowledge (such as spatial relation to landmarks or to other structures) and predefined rules to locate and restrict the original volume to a smaller volume that contains the desired structure. The rules and landmarks for segmenting orbital structures were described.

The reason for developing this method was the small size (compared to an image voxel), low intensity contrast, and the need for efficient segmentation of these structures in CT images. Although the method is extendable to other structures, the rules and landmarks would be different for other structures and must be redefined. One way of defining the rules could be *learning from demonstration* where the segmentation is performed by an expert(s) via interactive software. Similar to the method described in chapter 2, the new software can have two parts: 1. using the landmarks to restrict the original volume to a smaller one. 2. using the shape and intensity information to segment the desired structures. Information about each part such as features, the order of finding these landmarks, shapes, and rules can be stored from segmentation of multiple data. The landmarks and shapes can be used to define rules and develop an automatic segmentation pipeline for segmenting new target data.

Another benefit of this method is that can be an initial step toward labeling and segmenting enough medical volumes for complex algorithms such as convolutional neural network and deep learning that requires many training data.

6.2 Surgical Pathway Planning

The method of assisted pre-operative surgical pathway planning was proposed. The surgical decision-making for selecting the optimal pathway was translated into the cost function.

A weight vector was developed by our surgical colleague at the University of Washington for defining a single cost function in multi-objective optimization. One question that worth exploring is that if the weights and objectives are same at different institutions. The effect of different institution was shown in the field of robotic surgery and surgeon skill assessment [90].

In the proposed cost function the cosmetic factor was not included. The cosmetic results after the operation are important for both surgeons and patients in skull base surgery. The optimized pathways obtained by considering this factor in the cost function may be different compared to cost function without the cosmetic factor for the same target location. Studying and defining the cosmetics in this context and incorporating that in the cost function would produce pathways that improve the surgical results and must be explored.

Another question is if the surgeons' previous experiences or patients' data and outcomes, can be used in planning new cases. Therefore, the problem would be structured as learning and optimization. Although machine learning algorithms require labeled training data which is time consuming to label or collect, advances in computing, big data and major efforts from different companies to collect health information of individuals, may soon make the collecting and mining surgical data achievable.

Another question is how to utilize and visualize the optimized pathway in the operation room effectively and without distracting the surgeon. Surgeons often use the endoscopic view intra-operatively and only check the navigation screen to verify their position if needed.

Therefore, overlaying the optimized pathway on the navigation screen would distract the surgeon from the endoscopic view and won't be effective. One approach could be overlaying the pathway on the endoscopic screen which requires additional software development and instrument tracking. Furthermore, technologies such as augmented reality, virtual fixtures, head mounted display or other warning systems can be explored and tested to propose the most practical method.

Finally, the shape of the pathway used here was unbalanced biconical which was based on long and rigid instruments used in the current skull base surgeries. With technical advances in robotics, instruments size, and flexible robotics arms different shapes will be considered. The future work will study and characterize the pathways for robotic arms/ instruments with more degree of freedom.

6.3 Atlas-Based Surgical Pathway Planning

The purpose of this study was the idea that an anatomical atlas with detailed clinical information can be used in surgical pathway planning by transferring the data fields to new patient data. The hypothesis is that the obtained pathways could be more accurate using more clinical information. The work presented in Chapter 4 is an initial step for constructing and utilizing an atlas. The data fields of the atlas are extendable and more information about different structures or surgeries can be added.

The future work will study useful information to be considered in the atlas and how the cost function described in Chapter 3 would change with new information.

6.4 Summary of Future Work

This section provides a summary of possible future work relevant to the methods described in this thesis:

- Segmentation based on anatomical landmarks

  - Development of interactive software for learning the landmarks, shapes and rules for segmenting new structures

- Surgical pathway planning
  - Exploring the cosmetic factor in the optimization
  - Studying the effect of different institutions on weights and the surgical pathways selection from the Pareto optimal set
  - Pre-operative planning utilizing surgeons previous surgeries/experiances
  - Identifying the effect methods to utilize the optimal pathways in operation room without distracting the surgeons, virtual fixture
  - Characterizing the surgical pathway for flexible instruments/robotic arms

- Atlas-based surgical pathway planning
  - Identifying useful information for each voxel
  - Studying/defining the cost function based on new available information

BIBLIOGRAPHY

[1] Randall A Bly, Rohan Ramakrishna, Manuel Ferreira, and Kris S Moe. Lateral transorbital neuroendoscopic approach to the lateral cavernous sinus. *Journal of Neurological Surgery Part B: Skull Base*, 75(01):011–017, 2014.

[2] Avraham Abergel, Oren Cavel, Nevo Margalit, Dan M Fliss, and Ziv Gil. Comparison of quality of life after transnasal endoscopic vs open skull base tumor resection. *Archives of Otolaryngology–Head & Neck Surgery*, 138(2):142–147, 2012.

[3] W Hosemann and C Draf. Danger points, complications and medico-legal aspects in endoscopic sinus surgery. *GMS current topics in otorhinolaryngology, head and neck surgery*, 12, 2013.

[4] Neil Bhattacharyya. Ambulatory sinus and nasal surgery in the united states: demographics and perioperative outcomes. *The Laryngoscope*, 120(3):635–638, 2010.

[5] Anouk Borg, Matthew A Kirkman, and David Choi. Endoscopic endonasal anterior skull base surgery: A systematic review of complications during the past 65 years. *World neurosurgery*, 95:383–391, 2016.

[6] JA Martin, Glenn Regehr, Richard Reznick, Helen Macrae, John Murnaghan, Carol Hutchison, and M Brown. Objective structured assessment of technical skill (osats) for surgical residents. *British journal of surgery*, 84(2):273–278, 1997.

[7] Alastair G Lynn-Macrae, Rebecca A Lynn-Macrae, Janaki Emani, Robert C Kern, and David B Conley. Medicolegal analysis of injury during endoscopic sinus surgery. *The Laryngoscope*, 114(8):1492–1495, 2004.

[8] Kris S Moe, Chris M Bergeron, and Richard G Ellenbogen. Transorbital neuroendoscopic surgery. *Neurosurgery*, 67(3):ons16–ons28, 2010.

[9] Mark May, Howard L Levine, Sara J Mester, and Barry Schaitkin. Complications of endoscopic sinus surgery: analysis of 2108 patientsincidence and prevention. *The Laryngoscope*, 104(9):1080–1083, 1994.

[10] Dzung L Pham, Chenyang Xu, and Jerry L Prince. Current methods in medical image segmentation 1. *Annual review of biomedical engineering*, 2(1):315–337, 2000.

[11] Sujata Saini and Komal Arora. A study analysis on the different image segmentation techniques. *International Journal of Information & Computation Technology*, 4(14):1445–1452, 2014.

[12] Alireza Norouzi, Mohd Shafry Mohd Rahim, Ayman Altameem, Tanzila Saba, Abdolvahab Ehsani Rad, Amjad Rehman, and Mueen Uddin. Medical image segmentation methods, algorithms, and applications. *IETE Technical Review*, 31(3):199–213, 2014.

[13] Dzung L Pham, Chenyang Xu, and Jerry L Prince. Current methods in medical image segmentation 1. *Annual review of biomedical engineering*, 2(1):315–337, 2000.

[14] Masaharu Kobashi and Linda G Shapiro. Knowledge-based organ identification from ct images. *Pattern Recognition*, 28(4):475–491, 1995.

[15] Barbara Dobler and Rolf Bendl. Precise modelling of the eye for proton therapy of intra-ocular tumors. *Physics in medicine and biology*, 47(4):593, 2002.

[16] György Bekes, Eörs Máté, László G Nyúl, Attila Kuba, and Márta Fidrich. Geometrical model-based segmentation of the organs of sight on ct images. *Medical physics*, 35(2):735–743, 2008.

[17] Pierre-Francois D D'Haese, Valerie Duay, Rui Li, Aloys du Bois d'Aische, Thomas E Merchant, Anthony J Cmelak, Edwin F Donnelly, Kenneth J Niermann, Benoit MM Macq, and Benoit M Dawant. Automatic segmentation of brain structures for radiation therapy planning. In *Medical Imaging 2003*, pages 517–526. International Society for Optics and Photonics, 2003.

[18] Aurélie Isambert, Frédéric Dhermain, François Bidault, Olivier Commowick, Pierre-Yves Bondiau, Grégoire Malandain, and Dimitri Lefkopoulos. Evaluation of an atlas-based automatic segmentation software for the delineation of brain organs at risk in a radiation therapy clinical context. *Radiotherapy and oncology*, 87(1):93–99, 2008.

[19] Michael Gensheimer, Anthony Cmelak, Kenneth Niermann, and Benoit M Dawant. Automatic delineation of the optic nerves and chiasm on ct images. In *Medical Imaging*, pages 651216–651216. International Society for Optics and Photonics, 2007.

[20] Swetasudha Panda, Andrew J Asman, Michael P DeLisi, Louise A Mawn, Robert L Galloway, and Bennett A Landman. Robust optic nerve segmentation on clinically acquired ct. In *SPIE Medical Imaging*, pages 90341G–90341G. International Society for Optics and Photonics, 2014.

[21] Jack H. Noble and Benoit M. Dawant. Automatic segmentation of the optic nerves and chiasm in ct and mr using the atlas-navigated optimal medial axis and deformable-model algorithm. In *SPIE Medical Imaging*, page 7259, 2009.

[22] A. Chen and B. Dawant. A multi-atlas approach for the automatic segmentation of multiple structures in head and neck ct images. 02 2016.

[23] T. Albrecht, T. Gass, C. Langguth, and M. Lthi. Multi atlas segmentation with active shape model refinement for multi-organ segmentation in head and neck cancer radiotherapy planning. 12 2015.

[24] R. Lamba, J. McGahan, M. Corwin, T Tien C. Li, A. Seibert, and J. Boone. Ct hounsfield numbers of soft tissues on unenhanced abdominal ct scans: Variability between two different manufacturers mdct scanners. *IEEE transactions on medical imaging*, 203(5):1013–1020, 2014.

[25] John A Nelder and Roger Mead. A simplex method for function minimization. *The computer journal*, 7(4):308–313, 1965.

[26] Cancer Imaging Archive. Cancer treatment and diagnosis. *National Cancer Institute*.

[27] P. Aljabar, R.A. Heckemann, A. Hammers, J.V. Hajnal, and D. Rueckert. Multi-atlas based segmentation of brain images: Atlas selection and its effect on accuracy. *NeuroImage*, 46(3):726 – 738, 2009.

[28] Daniel P. Huttenlocher, Gregory A. Klanderman, and William J Rucklidge. Comparing images using the hausdorff distance. *IEEE Transactions on pattern analysis and machine intelligence*, 15(9):850–863, 1993.

[29] Jessica R Chang, Michael P Grant, and Shannath L Merbs. Enucleation as endoscopic sinus surgery complication. *JAMA ophthalmology*, 133(7):850–852, 2015.

[30] Alex P Zijdenbos, Benoit M Dawant, Richard A Margolin, and Andrew C Palmer. Morphometric analysis of white matter lesions in mr images: method and validation. *American Journal of Roentgenology*, 13(4):716–724, 1994.

[31] Raudaschl PF, Zaffino P, Sharp GC, Spadea MF, Chen A, Dawant BM , Albrecht T, Gass T , Langguth C, Lthi M, Jung F, Knapp O, Wesarg S, Mannion-Haworth R , Bowes M, Ashman A , Guillard G, Brett A, Vincent G , Orbes-Arteaga M , Crdenas-Pea D , Castellanos-Dominguez G , Aghdasi N , Li Y , Berens A , Moe K , Hannaford B , Schubert R , and Fritscher KD. . Evaluation of segmentation methods on head and neck ct: Auto-segmentation challenge 2015. *Medical Physics,*, (10.1002/mp.12197), 2017.

[32] Randall A Bly, David Su, Thomas S Lendvay, Diana Friedman, Blake Hannaford, Manuel Ferreira, and Kris S Moe. Multiportal robotic access to the anterior cranial fossa: a surgical and engineering feasibility study. *Computer Assisted Radiology and Surgery*, pages S85–S86, 2009.

[33] Isam Atroshi, Gert-Uno Larsson, Ewald Ornstein, Manfred Hofer, Ragnar Johnsson, and Jonas Ranstam. Outcomes of endoscopic surgery compared with open surgery for carpal tunnel syndrome among employed patients: randomised controlled trial. *bmj*, 332(7556):1473, 2006.

[34] Randall A Bly, Shu-Hong Chang, Maria Cudejkova, Jack J Liu, and Kris S Moe. Computer-guided orbital reconstruction to improve outcomes. *JAMA facial plastic surgery*, 15(2):113–120, 2013.

[35] Tirelli P., E de Momi, Borghese N.A., and G Ferrigno. An intelligent atlas-based planning system for keyhole neurosurgery. *Otolaryngology–Head and Neck Surgery*, 149(6):940–946, 2013.

[36] M Hayashibe, N Suzuki, M Hashizume, Y Kakeji, K Konishi, S Suzuki, and A Hattori. Preoperative planning system for surgical robotics setup with kinematics and haptics. *The International Journal of Medical Robotics and Computer Assisted Surgery*, 1(2):76–85, 2005.

[37] Kerem Pekkan, Brian Whited, Kirk Kanter, Shiva Sharma, Diane de Zelicourt, Kartik Sundareswaran, David Frakes, Jarek Rossignac, and Ajit P. Yoganathan. Patient-specific surgical planning and hemodynamic computational fluid dynamics optimization through free-form haptic anatomy editing tool (surgem). *Medical & Biological Engineering & Computing*, 46(11):1139–1152, 2008.

[38] A Popovic and K Trovato. Path planning for reducing tissue damage in minimally invasive brain access in: Computer assisted radiology and surgery (cars 2009) supplemental pp. *S132-S133*, 2009.

[39] Reuben Shamir, Idit Tamir, Elad Dabool, Leo Joskowicz, and Yigal Shoshan. A method for planning safe trajectories in image-guided keyhole neurosurgery. *Medical Image Computing and Computer-Assisted Intervention–MICCAI 2010*, pages 457–464, 2010.

[40] Ting Guo, Andrew Parrent, and Terry Peters. Automatic target and trajectory identification for deep brain stimulation (dbs) procedures. *Medical Image Computing and Computer-Assisted Intervention–MICCAI 2007*, pages 483–490, 2007.

[41] Louaï Adhami and Ève Coste-Manière. Optimal planning for minimally invasive surgical robots. *IEEE Transactions on Robotics and Automation*, 19(5):854–863, 2003.

[42] Claire Baegert, Caroline Villard, Pascal Schreck, Luc Soler, and Afshin Gangi. Trajectory optimization for the planning of percutaneous radiofrequency ablation of hepatic tumors. *Computer Aided Surgery*, 12(2):82–90, 2007.

[43] Alexander Seitel, Markus Engel, Christof M Sommer, Boris A Radeleff, Caroline Essert-Villard, Claire Baegert, Markus Fangerau, Klaus H Fritzsche, Kwong Yung, Hans-Peter Meinzer, et al. Computer-assisted trajectory planning for percutaneous needle insertions. *Medical physics*, 38(6):3246–3259, 2011.

[44] Jiann-Der Lee, Chung-Hsien Huang, and Shih-Tseng Lee. Improving stereotactic surgery using 3-d reconstruction. *IEEE engineering in medicine and biology magazine*, 21(6):109–116, 2002.

[45] Marc Vaillant, Christos Davatzikos, Russell Taylor, and R Bryan. A path-planning algorithm for image-guided neurosurgery. In *CVRMed-MRCAS'97*, pages 467–476. Springer, 1997.

[46] Caroline Essert, Maud Marchal, Sara Fernandez-Vidal, Tiziano DAlbis, Eric Bardinet, Claire Haegelen, Marie-Laure Welter, Jérôme Yelnik, and Pierre Jannin. Automatic parameters optimization for deep brain stimulation trajectory planning. In *Proceedings of MICCAI workshop DBSMC*, volume 12, pages 20–29, 2012.

[47] Igor Stenin, Stefan Hansen, Meike Becker, Georgios Sakas, Dieter Fellner, Thomas Klenzner, and Jörg Schipper. Minimally invasive multiport surgery of the lateral skull base. *BioMed research international*, 2014, 2014.

[48] Weiguang Yao, Purang Abolmaesumi, M Greenspan, and Randy E Ellis. An estimation/correction algorithm for detecting bone edges in ct images. *IEEE transactions on medical imaging*, 24(8):997–1010, 2005.

[49] John Canny. A computational approach to edge detection. *IEEE Transactions on pattern analysis and machine intelligence*, (6):679–698, 1986.

[50] Kostis Kaggelides, Peter J Elliott, and Robert B Fisher. Automatic location of the eyes in ct images of the head. In *Computer Assisted Radiology/Computergestützte Radiologie*, pages 683–688. Springer, 1993.

[51] Daniel Rueckert, Luke I Sonoda, Carmel Hayes, Derek LG Hill, Martin O Leach, and David J Hawkes. Nonrigid registration using free-form deformations: application to breast mr images. *IEEE transactions on medical imaging*, 18(8):712–721, 1999.

[52] Barkuru Sri harsha, PN Pournami, and V K Govindan. B-spline non rigid image registration using l˙bfgs optimizer. *International Journal of Computer Science and Information Technologies*, 5(3):3813–3816, 2014.

[53] Hrvoje Kalinić. Atlas-based image segmentation: A survey. 2009.

[54] Marc Ruiz, Anton Bardera, Imma Boada, Ivan Viola, Miquel Feixas, and Mateu Sbert. Automatic transfer functions based on informational divergence. *IEEE Transactions on Visualization and Computer Graphics*, 17(12):1932–1941, 2011.

[55] Marcin Czerwinski, Richard A Hopper, Joseph Gruss, and Jeffrey A Fearon. Major morbidity and mortality rates in craniofacial surgery: an analysis of 8101 major procedures. *Plastic and reconstructive surgery*, 126(1):181–186, 2010.

[56] Shafik N Wassef, Pete S Batra, and Samuel Barnett. Skull base inverted papilloma: a comprehensive review. *ISRN surgery*, 2012, 2012.

[57] Nava Aghdasi, Yangming Li, Angelique Berens, Kris S Moe, Randall A Bly, and Blake Hannaford. Atlas and feature based 3d pathway visualization enhancement for skull base pre-operative fast planning from head ct. In *SPIE Medical Imaging*, pages 941519–941519. International Society for Optics and Photonics, 2015.

[58] Karthik Balakrishnan and Kris S Moe. Applications and outcomes of orbital and transorbital endoscopic surgery. *Otolaryngology–Head and Neck Surgery*, 144(5):815–820, 2011.

[59] Kalyanmoy Deb, Karthik Sindhya, and Jussi Hakanen. Multi-objective optimization. In *Decision Sciences: Theory and Practice*, pages 145–184. CRC Press, 2016.

[60] Randall A Bly, David Su, Thomas S Lendvay, Diana Friedman, Blake Hannaford, Manuel Ferreira, and Kris S Moe. Multiportal robotic access to the anterior cranial fossa: a surgical and engineering feasibility study. *Otolaryngology–Head and Neck Surgery*, 149(6):940–946, 2013.

[61] Eckart Zitzler and Lothar Thiele. Multiobjective optimization using evolutionary algorithmsa comparative case study. In *International Conference on Parallel Problem Solving from Nature*, pages 292–301. Springer, 1998.

[62] Oleg Grodzevich and Oleksandr Romanko. Normalization and other topics in multi-objective optimization. 2006.

[63] Scott Kirkpatrick, C Daniel Gelatt, Mario P Vecchi, et al. Optimization by simulated annealing. *science*, 220(4598):671–680, 1983.

[64] Balram Suman and Prabhat Kumar. A survey of simulated annealing as a tool for single and multiobjective optimization. *Journal of the operational research society*, 57(10):1143–1160, 2006.

[65] Dimitris Bertsimas, John Tsitsiklis, et al. Simulated annealing. *Statistical science*, 8(1):10–15, 1993.

[66] Stuart Geman and Donald Geman. Stochastic relaxation, gibbs distributions, and the bayesian restoration of images. *IEEE Transactions on pattern analysis and machine intelligence*, (6):721–741, 1984.

[67] Elisha A Pazner and David Schmeidler. A difficulty in the concept of fairness. *The Review of Economic Studies*, 41(3):441–443, 1974.

[68] R Timothy Marler and Jasbir S Arora. Survey of multi-objective optimization methods for engineering. *Structural and multidisciplinary optimization*, 26(6):369–395, 2004.

[69] Carlos A Coello Coello and Gary B Lamont. *Applications of multi-objective evolutionary algorithms*, volume 1. World Scientific, 2004.

[70] Abdullah Konak, David W Coit, and Alice E Smith. Multi-objective optimization using genetic algorithms: A tutorial. *Reliability Engineering & System Safety*, 91(9):992–1007, 2006.

[71] Carlos A Coello Coello, Gary B Lamont, David A Van Veldhuizen, et al. *Evolutionary algorithms for solving multi-objective problems*, volume 5. Springer, 2007.

[72] Kalyanmoy Deb, Amrit Pratap, Sameer Agarwal, and TAMT Meyarivan. A fast and elitist multiobjective genetic algorithm: Nsga-ii. *IEEE transactions on evolutionary computation*, 6(2):182–197, 2002.

[73] Eckart Zitzler, Marco Laumanns, and Stefan Bleuler. A tutorial on evolutionary multiobjective optimization. *Metaheuristics for multiobjective optimisation*, pages 3–37, 2004.

[74] MATLAB Optimization Toolbox. *R2017a*. The MathWorks Inc., Natick, Massachusetts, 2010.

[75] M Janga Reddy and D Nagesh Kumar. Multi-objective particle swarm optimization for generating optimal trade-offs in reservoir operation. *Hydrological processes*, 21(21):2897–2909, 2007.

[76] Yuhui Shi. Particle swarm optimization. *IEEE Connections*, 2(1):8–13, 2004.

[77] Margarita Reyes-Sierra and CA Coello Coello. Multi-objective particle swarm optimizers: A survey of the state-of-the-art. *International journal of computational intelligence research*, 2(3):287–308, 2006.

[78] Carlos A Coello Coello, Gregorio Toscano Pulido, and M Salazar Lechuga. Handling multiple objectives with particle swarm optimization. *IEEE Transactions on evolutionary computation*, 8(3):256–279, 2004.

[79] Clark D Thompson and Hsiang Tsung Kung. Sorting on a mesh-connected parallel computer. *Communications of the ACM*, 20(4):263–271, 1977.

[80] Hrvoje Kalinić. Atlas-based image segmentation: A survey. 2009.

[81] Valérie Duay, Nawal Houhou, and J-P Thiran. Atlas-based segmentation of medical images locally constrained by level sets. In *Image Processing, 2005. ICIP 2005. IEEE International Conference on*, volume 2, pages II–1286. IEEE, 2005.

[82] XG Xu, TC Chao, and A Bozkurt. Vip-man: an image-based whole-body adult male model constructed from color photographs of the visible human project for multi-particle monte carlo calculations. *Health Physics*, 78(5):476–486, 2000.

[83] Thomas Schiemann, Jan Freudenberg, Bernhard Pflesser, Andreas Pommert, Kay Priesmeyer, Martin Riemer, Rainer Schubert, Ulf Tiede, and Karl Heinz Höhne. Exploring the visible human using the voxel-man framework. *Computerized Medical Imaging and Graphics*, 24(3):127–132, 2000.

[84] Alejandro F Frangi, Daniel Rueckert, Julia A Schnabel, and Wiro J Niessen. Automatic construction of multiple-object three-dimensional statistical shape models: Application to cardiac modeling. *IEEE transactions on medical imaging*, 21(9):1151–1166, 2002.

[85] Sarang Joshi, Brad Davis, Matthieu Jomier, and Guido Gerig. Unbiased diffeomorphic atlas construction for computational anatomy. *NeuroImage*, 23:S151–S160, 2004.

[86] Torsten Rohlfing, Robert Brandt, Randolf Menzel, and Calvin R Maurer. Evaluation of atlas selection strategies for atlas-based image segmentation with application to confocal microscopy images of bee brains. *NeuroImage*, 21(4):1428–1442, 2004.

[87] Marianna Jakab and Ron Kikinis. Head and neck atlas. 09 2015.

[88] Paolo Zaffino, Patrik Raudaschl, Karl Fritscher, Gregory C Sharp, and Maria Francesca Spadea. Technical note: plastimatch mabs, an open source tool for automatic image segmentation. *Medical Physics*, 43(9):5155–5160, 2016.

[89] Francisco PM Oliveira and Joao Manuel RS Tavares. Medical image registration: a review. *Computer methods in biomechanics and biomedical engineering*, 17(2):73–93, 2014.

[90] Timothy M Kowalewski. *Real-Time Quantitative Assessment of Surgical Skill.* PhD thesis, 2012.

Appendix A

Table A.1: Dice coefficient details

	Right			Left		
Subjects	Nerve	Globe	EO muscle	Nerve	Globe	EO muscle
S1	0.83	0.81	0.62	0.67	0.65	0.77
S2	0.81	0.79	0.63	0.85	0.85	0.83
S3	0.81	0.84	0.85	0.72	0.84	0.60
S4	0.8	0.81	0.71	0.69	0.78	0.80
S5	0.78	0.84	0.80	0.66	0.76	0.70
S6	0.78	0.73	0.65	0.68	0.77	0.76
S7	0.78	0.82	0.85	0.65	0.80	0.80
S8	0.77	0.83	0.70	0.66	0.81	0.79
S9	0.77	0.77	0.73	0.79	0.92	0.80
S10	0.74	0.82	0.65	0.77	0.81	0.81
S11	0.74	0.79	0.66	0.74	0.80	0.75
S12	0.72	0.83	0.72	0.65	0.70	0.80
S13	0.72	0.77	0.63	0.74	0.81	0.76
S14	0.72	0.87	0.70	0.67	0.82	0.70
S15	0.70	0.77	0.66	0.67	0.81	0.76
S16	0.70	0.80	0.90	0.72	0.83	0.84
S17	0.70	0.81	0.80	0.75	0.77	0.67
S18	0.70	0.69	0.80	0.64	0.85	0.71
S19	0.69	0.78	0.70	0.76	0.86	0.65
S20	0.69	0.84	0.79	0.65	0.82	0.81
S21	0.69	0.83	0.78	0.72	0.78	0.72
S22	0.74	0.79	0.71	0.65	0.80	0.81
S23	0.68	0.85	0.75	0.67	0.78	0.66
S24	0.68	0.86	0.85	0.66	0.78	0.80
S25	0.67	0.87	0.78	0.70	0.77	0.81
S26	0.67	0.85	0.78	0.68	0.80	0.81
S27	0.66	0.82	0.82	0.61	0.77	0.79
S28	0.68	0.88	0.80	0.72	0.85	0.71
S29	0.66	0.71	0.78	0.67	0.62	0.72
S30	0.65	0.73	0.79	0.66	0.76	0.80

Table A.2: 95 % Hausdorff distance details in mm

	Right (DH_1)			Left(DH_1)		
Subjects	Nerve	Globe	Muscles	Nerve	Globe	Muscles
S1	3.00	2.94	2.35	9.04	4.85	4.75
S2	3.00	2.90	1.39	3.73	2.50	2.50
S3	3.72	3.00	2.59	3.73	2.00	4.10
S4	4.16	3.00	2.50	6.10	3.24	3.00
S5	2.84	2.50	1.42	5.00	3.36	3.00
S6	2.54	3.39	3.00	6.31	3.39	4.44
S7	3.86	4.20	2.24	7.36	5.00	3.00
S8	4.90	2.69	2.19	6.95	2.94	2.69
S9	3.53	3.53	3.98	3.35	0.98	2.50
S10	4.05	2.69	2.50	5.60	2.91	2.69
S11	4.82	3.00	4.33	5.54	3.00	3.43
S12	2.31	2.32	3.48	3.40	3.00	3.00
S13	3.54	3.54	1.77	3.54	2.80	4.22
S14	2.34	3.00	3.22	3.35	3.51	3.10
S15	6.45	3.22	2.28	3.16	3.00	3.51
S16	6.11	3.00	1.39	8.32	3.00	2.79
S17	3.28	3.28	2.50	10.89	3.00	3.97
S18	6.76	4.00	3.08	4.65	3.00	3.92
S19	4.18	3.42	3.19	2.85	3.00	4.30
S20	13.41	3.00	3.00	12.87	3.00	3.00
S21	7.89	3.22	3.00	4.95	3.40	3.87
S22	2.59	3.22	3.48	8.52	3.00	3.24
S23	5.18	2.73	3.86	5.72	3.70	4.36
S24	3.95	2.50	1.32	7.89	2.94	2.69
S25	7.33	2.50	3.55	3.75	3.56	2.87
S26	2.50	2.50	2.79	3.50	2.79	2.22
S27	8.20	3.00	3.00	9.08	3.21	3.01
S28	3.53	1.86	1.27	2.82	1.86	2.18
S29	4.21	3.22	3.00	3.62	4.89	3.21
S30	4.18	2.94	2.69	7.46	5.00	3.94

Appendix B

Outline of the basic GA algorithm:

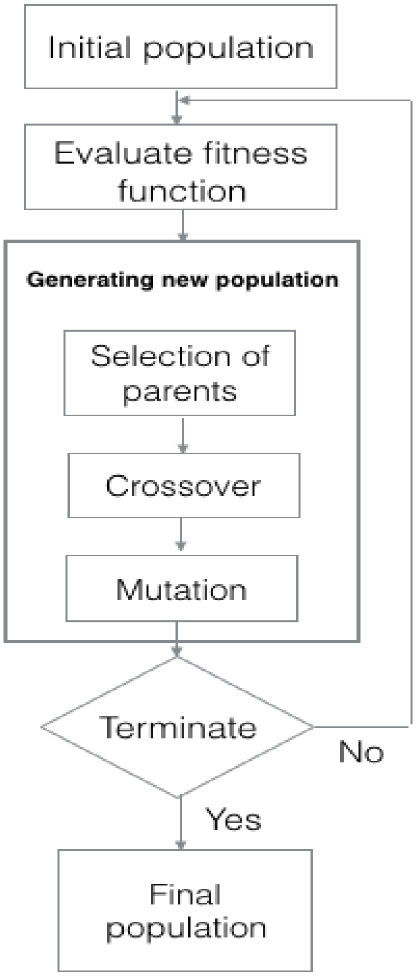

Figure B.1: Outline of basic GA algorithm

Outline of the basic NSGA-II algorithm:

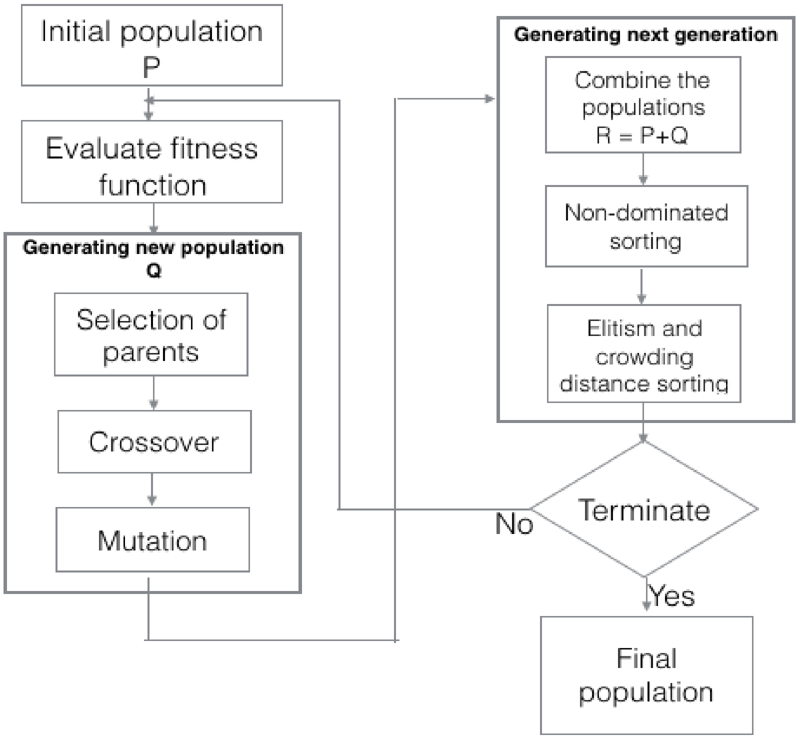

Figure B.2: Outline of basic NSGA-II algorithm

Outline of the basic PSO algorithm:

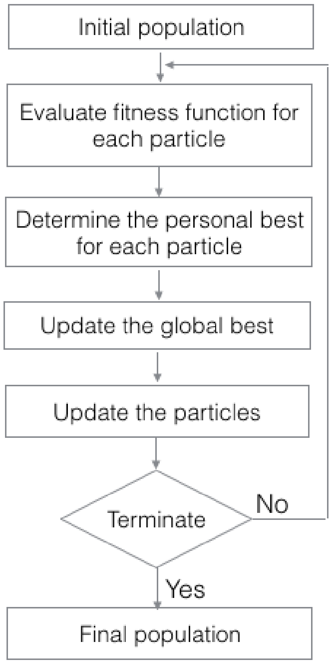

Figure B.3: Outline of basic PSO algorithm

Outline of the basic MOPSO algorithm:

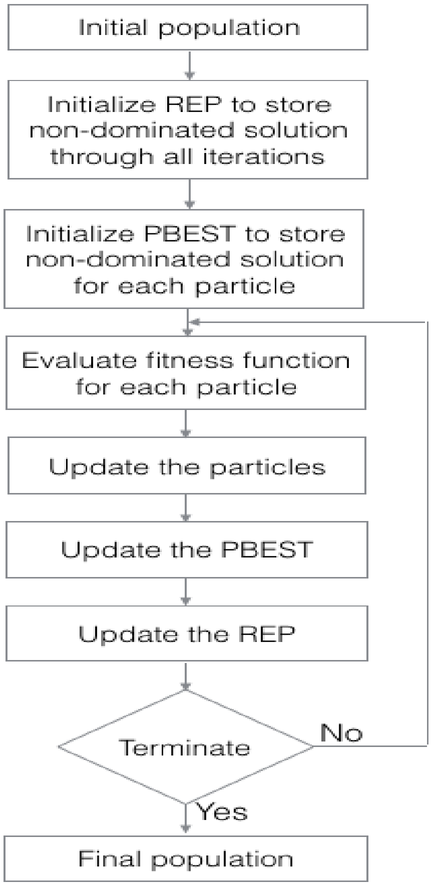

Figure B.4: Outline of basic MOPSO algorithm

VITA

Nava Aghdasi was born in 1987 and raised in Iran. She completed her Bachelor of Science in Electrical Engineering at the University of Washington, Seattle in 2012. As an undergraduate, she joined a project in the BioRobotics Laboratory to develop a smart low-cost medical simulator for Cricothyrotomy procedure. Her experiences in that project and her interest in teaching inspired her to pursue graduate school. Nava joined the BioRobotics Laboratory in 2012, as a graduate student, where she was advised by Professor Blake Hannaford and worked on characteristic and optimization of the surgical pathways in skull base surgery. In 2017 she earned a Doctor of Philosophy degree in Electrical Engineering from the University of Washington.